Advances in Optics and Photonics

Nonlinear photonics with high-*Q* whispering-gallery-mode resonators

Guoping Lin,[1] Aurélien Coillet,[2] and Yanne K. Chembo[3,4,*]

[1]*MOE Key Laboratory of Fundamental Quantities Measurement, School of Physics, Huazhong University of Science and Technology, Wuhan 430074, China*
[2]*Laboratoire Interdisciplinaire Carnot Bourgogne [CNRS UMR6303], Univ. Bourgogne-Franche-Comté, 9 Avenue A. Savary, 21078 Dijon, France*
[3]*GeorgiaTech-CNRS Joint International Laboratory [UMI 2958], Atlanta Mirror Site, School of Electrical and Computer Engineering, 777 Atlantic Dr NW, Atlanta, Georgia 30332, USA*
[4]*FEMTO-ST Institute, Univ. Bourgogne Franche-Comté, CNRS, Optics Department, 15B Avenue des Montboucons, 25030 Besançon cedex, France*
**Corresponding author: yanne.chembo@femto-st.fr*

Received May 1, 2017; revised September 1, 2017; accepted September 6, 2017; published November 15, 2017 (Doc. ID 295080)

High- and ultrahigh-*Q* whispering-gallery mode resonators have the capability to trap photons by total internal reflection for a duration ranging from nanoseconds to milliseconds. These exceptionally long photon lifetimes enhance the light–matter interactions at all scales, namely at the electronic, molecular, and lattice levels. As a consequence, nonlinear photon scattering can be triggered with very low threshold powers, down to a few microwatts. The possibility to efficiently harness photon–photon interactions with a system optimizing size, weight, power, and cost constraints has created a new, quickly thriving research area in photonics science and technology. This topic is inherently cross-disciplinary, as it stands at the intersection of nonlinear and quantum optics, crystallography, optoelectronics, and microwave photonics. From a fundamental perspective, high-*Q* whispering-gallery mode resonators have emerged as an ideal platform to investigate light–matter interactions in nonlinear bulk materials. From an applied viewpoint, technological applications include time-metrology, aerospace engineering, coherent optical fiber communications, or nonclassical light generation, among others. The aim of this paper is to provide an overview of the most recent advances in this area, which is increasingly gaining importance in contemporary photonics.

OCIS codes: (140.4780) Optical resonators; (160.2100) Electro-optical materials; (190.3270) Kerr effect; (190.4380) Nonlinear optics, four-wave mixing; (290.5900) Scattering, stimulated Brillouin; (290.5910) Scattering, stimulated Raman
https://doi.org/10.1364/AOP.9.000828

Nonlinear photonics with high-*Q* whispering-gallery-mode resonators

Guoping Lin, Aurélien Coillet, and Yanne K. Chembo

1. INTRODUCTION

Photonics research has witnessed an ever increased amount of interest for monolithic optical resonators in recent years. Originally, bulk optical cavities were predominantly considered as host material to harness specific effects, such as lasing after extrinsic doping, for example. In this context, intra-cavity photon lifetimes of the order of a few picoseconds were most of the time sufficient for the targeted applications, such as, for instance, in semiconductor lasers. However, it rapidly became evident that provided that the photon lifetimes were increased significantly, bulk resonators had more to offer owing to intrinsic nonlinear properties such as Pockels, Kerr, Raman, or Brillouin. Effectively in the case of long photon lifetimes, the probability of mutual interactions between the photons via the nonlinear bulk cavity was increased accordingly, and permitted direct optical frequency conversion with high efficiency. The nonlinearities of the bulk materials allow for multi-scale photon interactions via the electronic cloud oscillations, molecular vibrations, or lattice deformations. Therefore, reducing the intra-cavity losses and increasing the photon lifetimes from the picosecond to the microsecond range opened new perspectives from both the fundamental and applied viewpoints. In fact, it can be argued that this process literally created a new field in photonic science and technology.

One of the most widespread types of bulk optical cavities is the whispering-gallery-mode resonator (WGMR). The concept of whispering gallery arose in the late 19th century, in the context of the propagation of sound waves confined in galleries. This quite unconventional nomenclature stems from the fact that these specific acoustic waves are known to propagate along the inner periphery of certain galleries, with the most famous example being the dome of St. Paul's cathedral in London. It was a known fact that if someone whispered close to one point at the circular dome, someone else placed at the diametrically opposed position ($\simeq$30 m) could hear him distinctively. The first physical explanation for this phenomenon was proposed by Lord Rayleigh, and it relied on an acoustic ray interpretation involving multiple internal reflections along the inner periphery of the gallery [1]. Later on, in 1910, he improved his theory and proposed a more accurate formalism based on acoustic waves [2,3]. A decade later, Raman and Sutherland experimentally demonstrated the modal nature of the whispering-gallery wave in St. Paul's cathedral [4], by evidencing both circumferential and radial variations of intensity (resonance nodes).

The same phenomenology can be translated to the optical domain, where dielectric WGMRs can trap photons by total internal reflection. The first in-depth theoretical analysis of optical WGMRs based on Maxwell equations was proposed by Mie [5] and Debye [6] at the turn of 1910, in the context of the diffusion of light waves by spherical objects. Since then, remarkable contributions have been provided and contributed to achieve a quasi-complete understanding of these resonators, at least in the linear approximation (see [7,8] and references therein).

Nowadays, the size of WGMRs typically ranges from a few micrometers to a few millimeters, and they can have a very wide variety of geometrical shapes, including

spheres, disks, toroids, and even bubbles. The optical storage capacity of a resonator can be measured by its photon lifetime τ_{ph} for photons of angular frequency ω_0, or equivalently, by its quality (or Q) factor defined as $Q = \omega_0 \tau_{ph}$. The Q-factor is also generally defined as $Q = \omega_0/\Delta\omega$, where $\Delta\omega$ is the linewidth of the optical resonance around ω_0. To any given WGM resonator corresponds a unique eigenspectrum distribution, that is, a grid of narrow resonances distributed in a complex fashion in the spectral domain. A resonator with infinite Q would therefore feature zero loss, zero linewidth, and infinite photon lifetime in each of these resonances. By convention, resonators with $Q > 10^3$ are labeled as *high-Q*, while *ultrahigh-Q* resonators correspond to a quality factor better than 10^8.

The systematic investigation of the nonlinear properties of high-Q optical WGMRs started about 30 years ago, essentially with microsphere cavities [9]. Combined with very long photon lifetimes, the small mode volume inherent to these resonators led to a significant enhancement of the effective nonlinearities. Therefore, photon frequency conversion became possible by pumping these resonators with low-power continuous-wave (CW) lasers (in the microwatt to milliwatt range), yielding optical frequency combs overlapping the eigenspectrum distribution. Several bulk media of interest coincidentally share common structural features with the fused silica of optical fibers, and as a consequence, their transparency window overlaps the standard telecom wavelength of 1550 nm, which corresponds to a mature technological segment. This is why research on this topic directly benefited from the large inventory of off-the-shelf components already available in optical communication engineering for the generation, control, and monitoring of both light wave and microwave signals. Therefore, WGMRs fabricated with these materials have the potential to play the role of all-optical components via nonlinearity in telecommunication systems, thereby circumventing the bandwidth limitations of optoelectronic components. Beyond optical communications, optical WGMRs proved to provide novel solutions for leapfrog improvements in time-frequency metrology, sensing, and aerospace engineering, among other areas. Comprehensive reviews on these applications are plentiful, and include, for example, [10–16].

The purpose of the present paper is to provide insights into the contemporary research led in the field of high-Q optical whispering-gallery mode resonators. We also aim to highlight some of the most important results achieved in recent years, and to discuss some of the main challenges that will have to be met in the years to come.

The plan of the review is the following. In Section 2, we briefly present the linear theory of optical WGMRs, with an emphasis on the most common types of resonators used in nonlinear photonics. Section 3 will focus on second-order effects, such as second-harmonic generation (SHG), optical parametric oscillators, and sum-frequency generation (SFG). Section 4 will then review Kerr effects, such as third-harmonic generation (THG) and Kerr optical frequency comb generation. An overview of stimulated Raman scattering in WGMRs will be provided in Section 5, while Section 6 will be devoted to stimulated Brillouin scattering. The paper will end with a general conclusion.

2. HIGH- AND ULTRAHIGH-Q WHISPERING-GALLERY-MODE RESONATORS

The understanding of the nonlinear properties of high- and ultrahigh-Q WGMRs requires prior knowledge of their linear properties. We discuss them hereafter, and present as well the most widespread types of WGMRs for photonics applications.

2.1. Linear Properties of WGMRs

From a linear perspective, WGMRs are fully characterized by three main physical elements: the eigenmodes, the eigenspectrum, and the losses [7,8,13].

2.1a. Eigenmodes and Spatial Field Distribution

The eigenmodes are solutions of the Maxwell equations with boundary conditions corresponding to the interface between the bulk axi-symmetric resonator of main radius a and group velocity index n_g, and its surrounding medium which is often (but not always) air. The spatial distribution of the eigenmodes is mathematically defined by a complex-valued and vectorial function $\boldsymbol{\Upsilon}_\mu(\mathbf{r})$, where μ is a label that unambiguously defines each eigenmode, while $\mathbf{r} = (r, \theta, \phi)$ stands for the usual spherical coordinates. The eigenmodes always have a torus-like geometrical form, and satisfy the Helmholtz equation $[\Delta + (\omega_\mu/c)^2 \varepsilon(\mathbf{r})]\boldsymbol{\Upsilon}_\mu(\mathbf{r}) = \mathbf{0}$, where ω_μ is the eigenfrequency corresponding to the eigenmode $\boldsymbol{\Upsilon}_\mu(\mathbf{r})$, and $\varepsilon(\mathbf{r})$ is the spatially dependent permittivity.

The Helmholtz problem can be solved exactly for some simple geometries, such as the sphere. From a general point of view, the solutions with other axi-symmetric geometries can be obtained with a numerical solver, and it is generally found that the solutions are topologically quite similar to what is obtained with a sphere. Indeed, the resolution of the Helmholtz equation demonstrates that the label μ is in fact a quadruplet $\{\ell, m, n, p\}$. The parameter ℓ is the azimuthal eigennumber. It is associated with resonance condition $2\pi a n_g = \ell \lambda_\mu$, which imposes that the optical path in a round trip inside the cavity should be an integer multiple of the wavelength. The polar eigennumber m is such that $|m| \leq \ell$, and it rules the number of lobes ($\equiv \ell - |m| + 1$) in the perpendicular direction relatively to the equatorial plane of the torus. The radial eigennumber n corresponds to the number of lobes along the radial direction. Finally, the eigenparameter p stands for the polarization, which can be either TE or TM. It should be noted that by convention, a *family* of modes is defined by a fixed n, m and p, but freely varying ℓ values. In general, most of the optical field is confined within the close vicinity of the resonator's inner periphery, while the outer periphery principally hosts an evanescent field, which typically vanishes within a few wavelengths from the resonator boundary. Figure 1(a) illustrates the electric field distribution of a fundamental optical WGM for $\ell = 30$. The transverse field distributions in the cross section of the resonator for different radial and polar eigennumbers m and n are shown in Fig. 1(b), from which the fundamental and high-order WGMs can be clearly distinguished.

Assuming that the eigenmode solutions are normalized as $\int_\infty \|\boldsymbol{\Upsilon}_\mu(\mathbf{r})\|^2 \mathrm{d}V = 1$, the effective volume of each eigenmode can be calculated as $V_{\mathrm{eff},\mu} = [\int_V \|\boldsymbol{\Upsilon}_\mu(\mathbf{r})\|^4 \mathrm{d}V]^{-1}$, where V is the volume of the bulk resonator. It is important to note that this effective volume plays a key role for the nonlinear processes occurring in WGMRs. The spatial distribution of the modes is also particularly relevant when nonlinear phenomena involve a coupling between different families of modes $\{m, n, p\}$ and $\{m', n', p'\}$, as the coupling strength is generally proportional to the overlap integral $\int_V \boldsymbol{\Upsilon}^*_\mu(\mathbf{r}) \boldsymbol{\Upsilon}_{\mu'}(\mathbf{r}) \mathrm{d}V$.

2.1b. Eigenspectrum and Dispersion Profile

The resolution of the Helmholtz equation permits to determine as well the eigenspectrum of the resonator, that is, the set of frequencies ω_μ associated with each eigenmode $\boldsymbol{\Upsilon}_\mu(\mathbf{r})$. Even though approximate solutions exist for the spherical resonator, they are generally not available for axi-symmetric resonators of arbitrary shape. However, some general and useful properties can be outlined with regard to the physical influence of the parameters ℓ, m, n, and p.

The eigennumber ℓ is arguably the most important one because it is the leading parameter associated with the eigenfrequency ω_μ. The eigenfrequency can in first approximation be expressed as $\omega_\mu \simeq \ell\Omega_{\mathrm{FSR}}$, where $\Omega_{\mathrm{FSR}} = c/n_g a$ is the free spectral range (FSR) of the resonator. Hence, the order of magnitude of ℓ depends on the size of the resonator and the spectral range of interest. For example, around 1550 nm, a silica resonator would be such that $\ell \sim 10000$ (resp. $\ell \sim 100$) for a radius of 5 mm (resp. 50 μm). It is important to emphasize here on the physical interpretation of ℓ. From a classical point of view (geometrical optics approximation), this eigennumber corresponds to the integer number of internal reflections that a photon undergoes to perform a round trip inside the cavity. From a quantum optics standpoint, this eigennumber stands for the quantized angular momentum of the photons ($\simeq \hbar\ell/a$).

The families of polar eigenmodes defined by m are in practice always quasi-degenerate in frequency, and perfect degeneracy is achieved in the case of the sphere. Polarization families of modes are also quasi-degenerate in frequency, particularly for very high ℓ values [since $\Delta\omega_\mu/\omega_\mu \sim \mathcal{O}(\ell^{-1})$]; indeed, perfect degeneracy is never obtained, even for spherical resonators. The radial families of modes are always measurably nondegenerate in frequency as n is increased [with $\Delta\omega_\mu/\omega_\mu \sim \mathcal{O}(\ell^{-2/3})$]. The consequence of the nondegeneracy induced by m, n, and p is the presence of a very large number of distinctive eigenmodes in the Fourier spectrum, particularly when the resonator is in the millimeter range. In general, the unambiguous identification of the modes under these conditions is experimentally very difficult, if not impossible. This wide diversity of energy (frequency) and momentum possibilities for the intra-cavity photons can be beneficial or detrimental depending on the targeted application, and accordingly, a recurrent challenge while using WGMRs is to frustrate or emulate the coupling between these nondegenerated families of modes.

Within a given family of modes (m, n, and p are fixed), the eigenspectrum features a quasi-equidistant grid of modes spaced by the free spectral range Ω_{FSR}. The residual nonequidistance is referred to as *dispersion*, and it has two main contributions, namely chromatic and geometric. Chromatic dispersion is a material property of the bulk

Figure 1

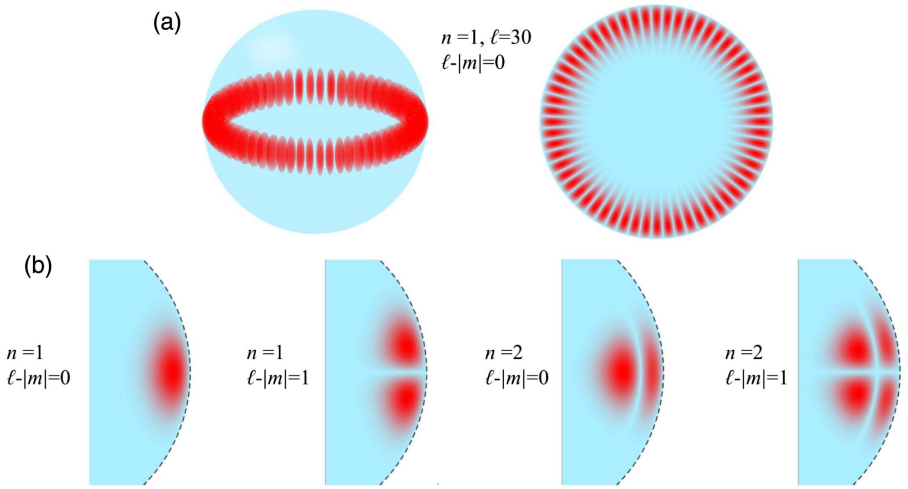

Illustration of the electric field amplitude distribution of optical WGMs in a spherical dielectric resonator. (a) Left: a 3D representation for the mode with $n = 1$, $\ell = 30$, and $\ell - |m| = 0$; Right: the corresponding 2D top view. (b) Examples of 2D transverse field distributions for different radial and polar eigennumbers n and m. Note that the evanescent field is not illustrated here.

resonator, and can be empirically calculated using the Sellmeier expansion. On the other hand, geometrical dispersion is exclusively defined by the shape of the resonator. This latter contribution can be used to engineer the overall dispersion profile of the resonator, since the bulk material dispersion cannot be directly tuned. Dispersion is frequency dependent, and therefore should be defined with respect to a given frequency $\omega_{\mu_0} \equiv \omega_{\ell_0}$. From a mathematical perspective, the eigenfrequencies ω_ℓ around ω_{ℓ_0} can be defined using the following Taylor expansion: $\omega_\ell = \omega_{\ell_0} + \sum_{k=1}^{+\infty} (\zeta_k/k!)(\ell - \ell_0)^k$, where $\zeta_1 \equiv \Omega_{\mathrm{FSR}}$ while ζ_k stands for the k^{th}-order dispersion for $k \geq 2$. The perfectly equidistant grid in the dispersionless limit is therefore recovered by setting $\zeta_k \equiv 0$ for $k \geq 2$. Hence, the dominant dispersion term is ζ_2, and is sometimes referred to as *group-velocity dispersion* (GVD). By convention, GVD is considered *normal* when $\zeta_2 < 0$, and *anomalous* when $\zeta_2 > 0$. The nature and magnitude of overall dispersion plays an important role for coherent interactions where phase matching (PM) conditions have to be respected.

2.1c. Q-Factor: Intrinsic and Coupling Losses

As indicated in the general introduction, the characterization of losses in WGMRs is generally performed in terms of quality factor, or "Q-factor."

The intra-cavity losses are characterized by the intrinsic quality factor $Q_{\mathrm{in}} = \omega_0 \tau_{\mathrm{ph,in}} = \omega_0/\Delta\omega_{\mathrm{in}}$. The intrinsic Q-factor can be further decomposed as $Q_{\mathrm{in}}^{-1} = Q_{\mathrm{vol}}^{-1} + Q_{\mathrm{surf}}^{-1} + Q_{\mathrm{rad}}^{-1}$, in order to account for the volumic, surface scattering, and radiation losses, respectively. It is important to note that the radiative Q-factor increases exponentially with ℓ [13]: it is therefore quasi-infinite for $\ell \gg 1$, which corresponds to resonators much larger than the wavelength ($a \gg \lambda$). Therefore, in practice, the intrinsic Q-factor is limited by the surface roughness (Q_{surf}), and sometimes by intra-cavity volumic losses (Q_{vol}). In general, the intrinsic Q-factor can vary widely depending on the type of resonators. On the one hand, the typical Q-factor for crystalline WGMRs is of the order of 10^9, which typically corresponds to an intrinsic photon lifetime of ~1 μs for a resonance at ~1550 nm. On the other hand, integrated WGM and ring resonators typically feature a quality factor of the order of 10^6 at 1550 nm ($\tau_{\mathrm{ph,in}} \sim 1$ ns). It is also noteworthy that crystalline WGMRs generally have a millimeter size yielding a FSR in the range of a few gigahertz, while integrated resonators typically have a sub-millimeter size and a FSR in the terahertz range.

Beyond the intrinsic quality factor Q_{in} of the resonators, it is important to account as well for the coupling (or external) quality factor Q_{ext}. The external Q-factor can itself have several contributions depending on the actual configuration of the coupling, which can involve one or two coupling ports. The coupling is generally performed using a tapered fiber (or waveguide), an angle-polished fiber tip, or a prism.

The overall Q-factor is explicitly defined as $Q_{\mathrm{tot}}^{-1} = Q_{\mathrm{in}}^{-1} + Q_{\mathrm{ext}}^{-1}$, corresponding to an overall photon lifetime and resonance linewidth $Q_{\mathrm{tot}} = \omega_0 \tau_{\mathrm{ph}} = \omega_0/\Delta\omega_{\mathrm{tot}}$. The three main regimes of coupling are under-coupling ($Q_{\mathrm{in}} < Q_{\mathrm{ext}}$), over-coupling ($Q_{\mathrm{in}} > Q_{\mathrm{ext}}$), and critical coupling ($Q_{\mathrm{in}} = Q_{\mathrm{ext}}$). All these contributions to the quality factor can generally be determined using the cavity-ring down or other ringing techniques [17], particularly when they are above a billion. The main motivation for achieving ultrahigh Q-factors is that it allows to benefit from a very narrow filtering in the optical domain, since the linewidth scales as Q^{-1} and can reach values well below 1 MHz for modes around 1550 nm (~200 THz). Such Q-factors also permit to trigger nonlinear effects with smaller pump powers, because the threshold powers generally scale as Q^{-n} with $n \geq 1$.

2.2. Various Types of WGMRs

WGMRs used in nonlinear and quantum optics can generally be classified into several categories, and the main ones are briefly outlined hereafter.

2.2a. Microsphere and Microbubble Resonators

Microspheres have an historically important place in WGM research because they correspond to the very first configurations that were investigated theoretically. When the ratio a/λ is low ($\sim$1), the radiative quality factor Q_{rad} is low as well and light can be radiatively coupled inside the resonator (the resonators are said to be radiatively *open*). This situation, frequently encountered when light is scattered by liquid droplets and aerosols, is typically investigated within the theoretical framework of Mie scattering [18,19] and morphology-dependent resonances [20]. However, solid-state resonators in that size range are scarce. On the other hand, microspheres with a higher ratio a/λ ($\sim$10–100) can be obtained by melting amorphous media and letting the surface tension create quasi-spherical droplets, which become solid-state microresonators after cooling [21,22]. Such microspheres are already radiatively closed ($Q_{\mathrm{rad}} \sim +\infty$ for all practical purposes), and cannot be coupled directly with incoming free-propagating radiations. Instead, waveguide or prism coupling has to be implemented, as explained in Subsection 2.1c. The bulk material is generally fused silica, and the intrinsic Q-factor for these microspheres can be very high, of the order of a billion at 1550 nm. For being amorphous, microspheres can be doped and driven in a regime of quasi-transparency, where the effective quality factor reaches record high values ($Q = 3 \times 10^{12}$ and $\tau_{\mathrm{ph}} = 2.5$ ms at 1530 nm; see [23]).

Another important family of microresonators are the so-called microbubbles [24–27]. They are generally fabricated using amorphous media like fused silica, and are characterized by a hollow core. They can therefore only sustain lower radial order modes. Microbubbles typically have a size of $\sim$100 μm and offer numerous advantages for sensing and microfluidic applications. In particular, they feature absolute tunability (that is, beyond a FSR), as the main radius of the resonator can be controllably varied via piezo-electric or gas pression stress [28,29,30]. A heating wire can also be inserted for broad range electrical thermo-optic tuning, which was demonstrated in a microtube resonator [31]. WGMs in the terahertz domain are also explored with bubble-like resonators [32].

2.2b. Mushroom Resonators

The so-called "mushroom" WGMRs are chip-scale resonators that are suspended on a pedestal. This appellation is an obvious reference to their peculiar geometrical form. They generally have either a toroidal, a disk, or a wedge shape.

Toroidal mushroom resonators have been introduced for the first time in [33]. They are manufactured using a combination of lithography, dry etching, and selective reflow process. They feature an intrinsic quality factor higher than 10^8 at 1550 nm, thereby providing a significant improvement ($>$1000) with regard to existing technologies. The small size of the resonator, combined with the very strong confinement provided by the toroidal shape (see Fig. 2), yields a very small effective volume, and thereby enhances the nonlinear interaction. This is one of the reasons why it has been the first integrated platform where various kinds of nonlinear interactions have been observed [34–36]. It should also be noted that beyond the enhancement of fundamental nonlinear interaction in the bulk material, toroidal resonators are also ideal for optomechanics research. This is due to the fact that the resonator can mechanically oscillate on its pedestal with very low mechanical losses, thereby yielding mechanical modes with high Q-factors, as reviewed in [37]. Wedge-resonators feature an inclined rim [38–40], as displayed in Fig. 3. They have been shown to feature some of the highest

intrinsic Q-factors for integrated resonators, of the order of a billion at telecom wavelength [39].

2.2c. Ring Resonators

Strictly speaking, ring (or racetrack) resonators as shown in Fig. 4 are not WGMRs, but this subtle distinction is more semantic than anything else in practice. The first advantage of ring resonators is that the closed path of the ring does not need to be circular with perimeter $L = 2\pi a$, with a being the eventual radius of the circle: instead, these resonators can feature the same perimeter L on a surface that is smaller than πa^2. This allows to pack a much larger number of resonators into the same surface on a chip and avoid stitching errors during the etching process [41]. A second advantage of the ring resonators is that they permit very precise adjustment of the geometrical shape of the resonator, thereby permitting a full control of its modal structure. It allows engineering of the overall dispersion profile with great flexibility and precision. This is how some resonators can be tuned to feature anomalous overall dispersion, while their constituting bulk material has normal dispersion. A third advantage of racetrack resonators is that the coupling bus waveguide is integrated as well, allowing for quasi-perfect mechanical stability of the coupling and very accurate design for the coupling strength. And most importantly, chip-scale integration offered by ring resonators virtually opens the way to scalability, mass production, cost-effectiveness, and ultimately, ubiquitousness for mass-market applications requiring all-optical frequency conversion. These advantages are significant enough to justify the strong interest and research activity devoted to the development of ring resonators in recent years.

One of the most important benchmarks for integrated ring resonators is silicon nitride (Si_3N_4). Common methods to fabricate integrated devices using silicon nitride involve low-pressure chemical vapor deposition, reactive ion etching, and thermal annealing. These processes are generally difficult to implement efficiently because of the mechanical stress that induces cracks in the bulk material during the growth process, thereby increasing the intra-cavity losses. However, several research groups have overcome this technical difficulty and achieved a Q-factor which is typically of the order of 10^6 for sub-millimeter resonators [41–45]. It is noteworthy that silicon nitride has a much stronger nonlinear coefficient n_2 compared to silica, typically 10 times higher. This property, along with low two-photon absorption and low linear

Figure 2

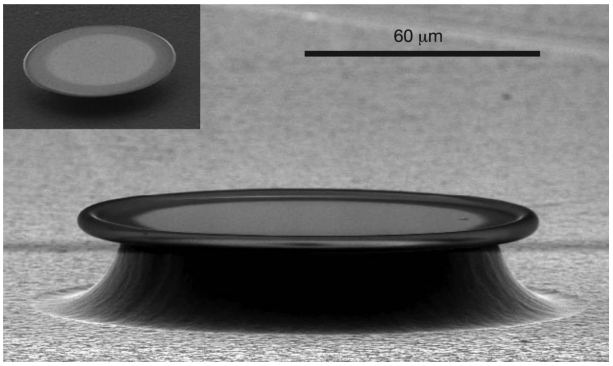

Figure of a toroidal mushroom WGM resonator, made with silica. The WGM is confined within the toroidal protuberance at the peripheral edge of the resonator. The quality factor is in excess of 10^8 at 1550 nm. Reprinted by permission from Macmillan Publishers Ltd.: Armani *et al.*, Nature, **421**, 925–928 (2003) [33]. Copyright 2003.

losses at 1550 nm, justifies the popularity of this material for integrated nonlinear platforms, as threshold power to trigger the nonlinear interactions is inversely proportional to n_2.

2.2d. Millimeter-Size Disk Resonators

Millimeter-size WGM disk resonators are optical cavities that are generally fabricated individually using a grinding and polishing technique [46]. An example of a millimeter-size WGMR coupled with a fiber taper is displayed in Fig. 5. It has been shown that such resonators can be fabricated at a large scale using laser machining techniques [47].

Millimeter-size WGMRs typically feature a nanometer surface roughness and very low intra-cavity losses, which allow them to reach exceptionally high quality factors, with the record value being set at 3×10^{11} at 1550 nm [48]. The most widespread bulk materials for such resonators are fluoride crystals, such as calcium fluoride [49,50], magnesium fluoride [51], barium fluoride [52,53], lithium fluoride [53,54], and strontium fluoride [55]. Lithium niobate resonators are also frequently manufactured under this geometrical shape [56,57]. It is important to note that these resonators can be amorphous as well, as they can be manufactured with fused silica [58], or fused quartz [59], for example. Millimeter-size resonators can also be integrated in ultracompact devices [60], a feature of particular relevance for technological applications.

3. SECOND-ORDER NONLINEAR EFFECTS

The second-order optical nonlinearity results from the quadratic nonlinear polarization response of material, in which the electron cloud distribution is distorted by external electric fields at the optical frequency. It occurs in crystal materials with noncentrosymmetric structures. The polarization response is expressed as $P^{(2)}(t) = \varepsilon_0 \chi^{(2)} E^2(t)$, where ε_0 and $\chi^{(2)}$ are the permittivity and the second-order nonlinear susceptibilities of the medium, while $E(t)$ is the external electric field strength. Light interaction with second-order nonlinear materials can enable the energy and momentum transfer between light waves at different frequencies. Such parametric processes are popular ways for generating laser radiations at new frequencies. WGMRs featuring optical

Figure 3

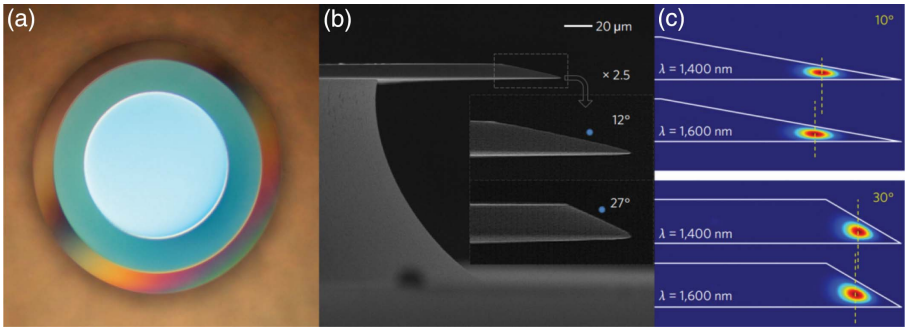

Ultrahigh-Q wedge resonators on a silicon chip. The resonator has a quality factor of the order of 10^9 at 1550 nm, a record value for an on-chip resonator. (a) Top view of the 1-mm diameter wedge resonator. (b) Scanning electron micrograph showing the side view of a resonator (insets are slightly magnified micrographs, and blue circles indicate the approximate locations of the taper during measurements). (c) Calculated fundamental-mode intensity profiles in resonators for various wedge angles and pump wavelengths. Reprinted by permission from Macmillan Publishers Ltd.: Lee, *et al.*, Nat. Photonics, **6**, 369–373 (2012) [39]. Copyright 2012.

modes with small mode volumes and very high Q-factors can therefore be explored for resonance-enhanced second-order nonlinear processes. These nonlinear effects include second-harmonic generation, optical parametric oscillation, and sum-frequency generation [61–63]. They have been used to generate various light sources including nonclassical ones [15]. A recent report also shows that strong coupling between optical modes of different colors can be realized in an on-chip nonlinear cavity [64].

3.1. Second-Harmonic Generation in WGMRs

Second-harmonic generation can be seen as a degenerate case of sum-frequency generation where two photons at pump frequency are converted into one photon at doubled frequency. For efficient SHG with WGMRs, the three key factors to consider are the material, phase matching, and mode overlap conditions.

First, as it is well known that $\chi^{(2)}$ becomes null in materials with inversion symmetry, the material investigation of WGMRs for SHG mainly focuses on noncentrosymmetric crystalline materials. It should be also mentioned that several works have been carried out on SHG with centrosymmetric materials. For instance, the $\chi^{(2)}$ response can be induced by breaking the bulk symmetry of a centrosymmetric material. SHG in a microring resonator made of silicon nitride was demonstrated [65]. In addition, one can also deposit a small number of molecules on the surface of a microsphere resonator for SHG investigation [66,61]. In this review, we will focus on the SHG with noncentrosymmetric crystalline WGMRs.

The second key condition for efficient SHG in WGMRs is the fulfillment of PM, which is required by the law of momentum conservation [61,62,67]. To clearly visualize the origin of different phase matching techniques, we can first consider the case of SHG in one-dimensional material under undepleted pump and slowly varying envelope approximation. The growth of the harmonic field in this case can be expressed by [68]

Figure 4

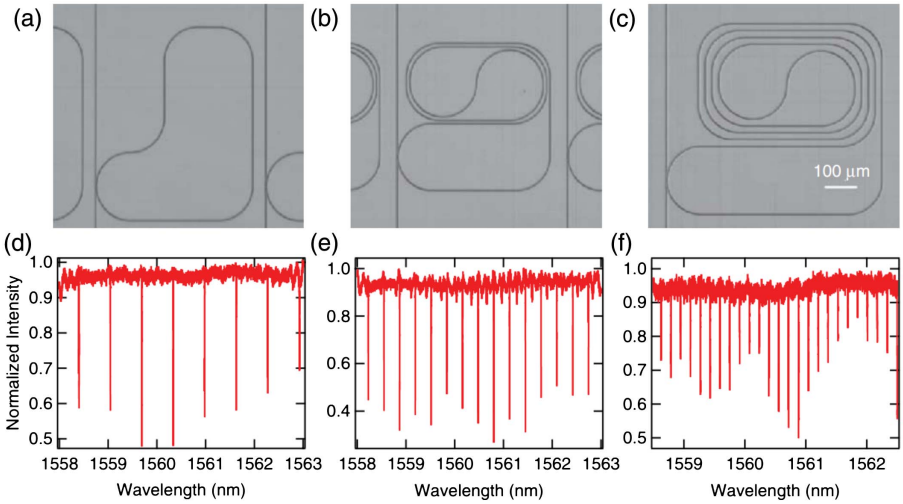

Integrated silicon nitride racetrack resonators. Folded trajectories allow achievement of longer optical paths and therefore shorter FSRs in a small surface footprint. These resonators feature a loaded quality factor $Q \sim 10^5$ at 1550 nm and have a FSR of (a) 80 GHz, (b) 40 GHz, and (c) 20 GHz. Figures (d)–(f) display the transmission spectra where the corresponding WGM resonances can be observed. Adapted from [41]. Copyright 2012 Optical Society of America.

$$\frac{dE_2}{dz} = \frac{-i\omega_2^2}{c^2 k_2}\chi^{(2)} E_2^2 e^{i\Delta kz}, \tag{1}$$

where $E_{1,2}$ and $\omega_{1,2}$ are the electric field amplitudes and frequencies of light, the sub-indices 1,2 represent the pump and harmonic fields, respectively, c is the speed of light in vacuum, and $\Delta kz = (k_2 - 2k_1)z$ is the phase difference between pump and harmonic wavenumbers. Mathematically, one sees that the harmonic light can grow coherently if the phase mismatch term Δk becomes zero. The corresponding techniques to fulfill this condition are birefringent phase matching and modal phase matching. On the other hand, in the case of a stationary phase mismatch, the harmonic light would beat as it propagates in the medium. However, if one flips the sign of $\chi^{(2)}$ with a period $\Lambda = 2\pi j/\Delta k$ where j is an integer, then efficient SHG can also be possible. This method is referred to as quasi-phase matching. For doubly resonant enhanced SHG in WGMRs, these phase matching approaches can be written in the form of azimuthal mode numbers following $m_2 = 2m_1 + M$, where $m_{1,2}$ are the azimuthal mode numbers with the sub-indices representing the pump and harmonic modes, respectively, and M is an integer [62]. For birefringent and modal phase matching, M is equal to zero, while for quasi-phase matching, M is any nonzero integer.

The third and last key condition for efficient SHG is to ensure a good mode overlap between the pump and harmonic waves in both spectral and spatial regimes.

Table 1 shows the reported SHG in crystalline WGMRs under CW pump [56,69–78]. Different PM techniques have been explored, depending on the size and the material

Figure 5

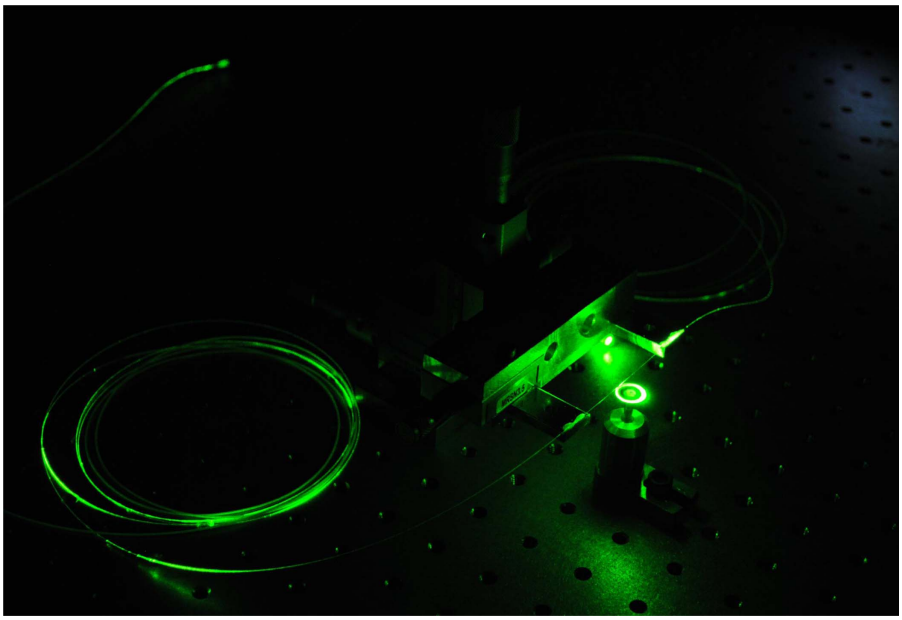

Millimeter-size WGMR coupled with a green laser using a tapered fiber at the FEMTO-ST Institute, France. The laser is in the upper left part of the picture and cannot be seen, for being in the dark. The resonator, which is in the lower right part of the picture, is held by a metallic stem. This resonator is made with MgF_2 and features an intrinsic quality factor in excess of 10^9 at 1550 nm. The optical fiber connecting the laser to the resonator is bare, and its spooled path can therefore be identified owing to the scattering of the green laser light.

Table 1. Summary of Reported CW SHG in Crystalline WGMRs

Phase Matching	Crystal	D (mm)	λ_P	η_m at P_P(mW)	η (mW^{-1})	References
Quasi-PM	$LiNbO_3$	3.0	1550	50% at 25		[56]
			1319	2% at 30		
Natural PM	$LiNbO_3$	3.8	1064	9% at 0.03		[69]
	$Li_2B_4O_7$	2.3	490	2.2% at 5.9	0.37%	[70]
cyclic PM	BBO	1.8	1557	0.069% at 1.1	0.063%	[71]
			974	1.15% at 0.25	4.6%	
			870	1.57% at 0.87	1.8%	
			634	0.31% at 0.42	0.74%	
	$LiNbO_3$	0.10	1540	1.1% at 10	0.11%	[72]
$\bar{4}$ Quasi-PM + Modal PM	GaAs	5.2×10^{-3}	1985		5×10^{-5}	[73]
	AlGaAs	3.8×10^{-3}	1584		7×10^{-7}	[74]
	GaP	6.5×10^{-3}	1545		3.8×10^{-4}	[75]
Modal PM	$LiNbO_3$	28×10^{-3}	1546		1.1×10^{-4}	[76]
	ZnSe	15×10^{-3}	1550		8.8×10^{-7}	[77]
	GaN	8×10^{-3}	1550		2×10^{-9}	[78]

of the resonators. Here, we consider WGMRs with diameters (D) of the order of a few millimeters as large resonators, while WGMRs with few or a few tens of micrometers are considered as small resonators. The impact of modal dispersion is present everywhere in WGMRs, but it is only dominant in small WGMRs. Additionally, it should be noted that $\bar{4}$ quasi-phase matching corresponds to $M = \pm 2$. Thereby, it is only dominant for small WGMRs that have optical modes with small m numbers. In large uniaxial crystalline WGMRs where m is easily above a thousand, three types of phase matching methods have been demonstrated, as illustrated in Figs. 6(a)–6(c). In Table 1, D is the diameter of the resonator, λ_P is the pump wavelength, and η_m presents the maximum observed conversion efficiency observed at the pump power of P_P. Saturation effects have been observed in $LiNbO_3$ WGMRs [56,69], in which the conversion efficiency per milliwatt pump power is not provided and thus is left empty in the table.

3.1a. Quasi-Phase Matching

Quasi-phase matching as shown in Fig. 6(a) requires periodical inversion of the nonlinear susceptibility to compensate for a stationary phase mismatch between the pump and harmonic fields. This phase matching method in crystalline WGMRs was first proposed and theoretically investigated for optical parametric oscillation by Ilchenko *et al.* in 2003 [79]. A year later, they succeeded to demonstrate efficient

Figure 6

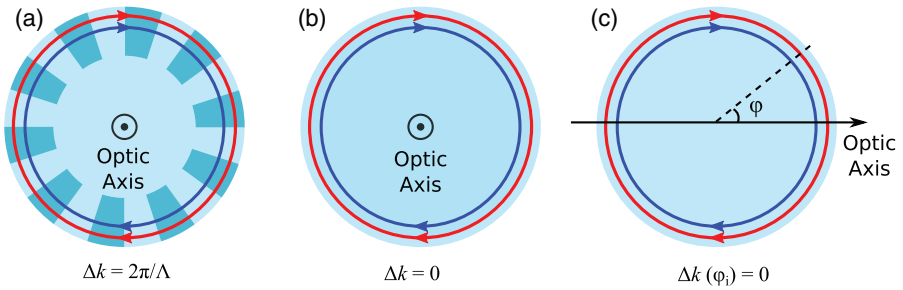

Schematic drawing of phase matching methods in large uniaxial crystalline WGMRs. Red: pump light. Blue: second-harmonic light. (a) Quasi-phase matching. (b) Natural phase matching. (c) Orientation-based birefringent *cyclic* phase matching. Note: modal phase matching not shown here is a dominant method for SHG in microscale WGMRs.

CW SHG in a WGM made of lithium niobate ($LiNbO_3$) crystals [56]. Figure 7(a) shows the illustration and photography of the $LiNbO_3$ WGMR. The photo presents a disk resonator cut out from a commercially available Z-cut $LiNbO_3$ wafer with a linearly poling structure. In Fig. 7(b), one can clearly observe the WGM resonances spectrum from the pump transmission as the pump lasers were scanned across several WGMs around 1.55 μm. When phase matching and good mode overlap for pump and harmonic waves are achieved, one obtains efficiently converted harmonic signal at 775 nm. The maximum conversion efficiency reached about 50% with only 25 mW pump power, as listed in Table 1. The conversion efficiency was found to saturate at a pump power of 300 mW in Fig. 7(c).

If one unfolds the circulating light of a WGM into a straight line, it can be seen that the light would experience a nonconstant poling period in one round trip. Although it would not reach the best conversion efficiency compared with a radially poled structure, it has an increased phase matching spectral bandwidth [67,79,80]. For example, cascaded harmonic generation up to the fourth harmonic was demonstrated using a linearly poled $LiNbO_3$ disk [65]. We also show here SHG in a radially poled $LiNbO_3$ disk for comparison, although the poling period was not optimized and the pump source was a pulsed laser [81]. Currently, quasi-phase matching in WGMRs can be obtained by periodical poling using lithography-based or calligraphic methods [62].

3.1b. Natural Phase Matching

Phase matching $\Delta k = 0$ can also be achieved by using the natural birefringence of crystals in WGMRs by carefully adjusting the temperature, as illustrated in Fig. 8.

Figure 7

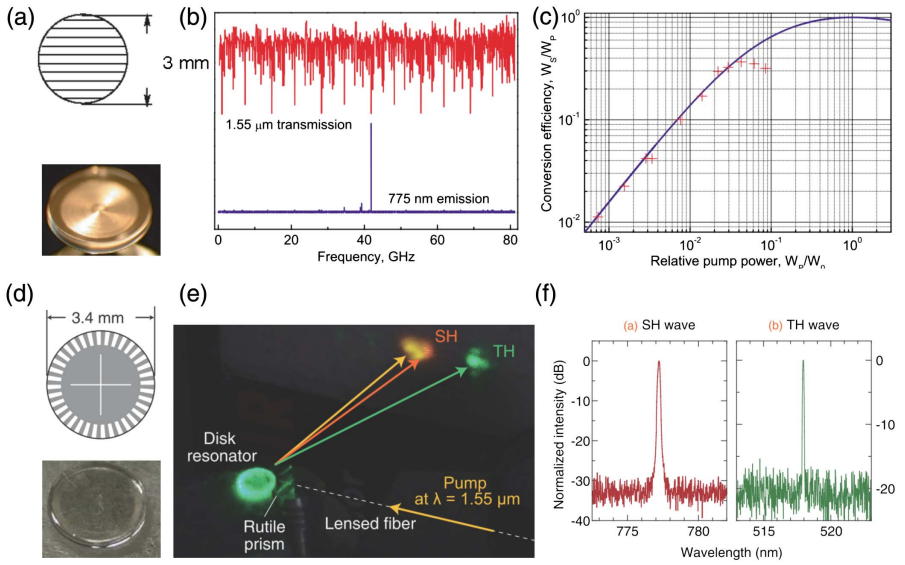

SHG in linearly poled $LiNbO_3$ WGMRs: (a) Schematic of the poling pattern and an image of the disk. (b) The transmitted pump (red) and second-harmonic (blue) signals when the pump frequency scanning covers several WGM FSRs. (c) Conversion efficiency as a function of the normalized pump power. Figures 1, 2, and 3 reprinted with permission from Ilchenko, *et al.*, Phys. Rev. Lett., **92**, 043903 (2004) [56]. Copyright 2004 by the American Physical Society. SHG in radially poled $LiNbO_3$ WGMRs: (d) Schematic and image of the disk. (e) Photo of the coupling setup with visible harmonic signals. (f) Spectra of harmonic signals. Reprinted with permission from [81]. Copyright 2009 The Japan Society of Applied Physics.

This natural phase matching method is also referred to as noncritical phase matching (NCPM). In the case of a negative uniaxial crystal, one can set the pump as ordinary polarized light and the harmonic field will be extraordinary polarized light. In Z-cut WGMRs, they correspond to a TM-polarized mode at pump and TE-polarized mode at harmonic, respectively. This method is functional at a specific spectral window and a particular temperature range. In 2010, Fürst *et al.* demonstrated efficient SHG using NCPM in a MgO-doped $LiNbO_3$ disk resonator [69]. Figure 8(a) presents a typical prism coupled WGMR setup. Tuning methods were achieved by adjusting the temperature and bias voltage of the resonator. Efficient harmonic generation was found when the temperature was tuned to a specific value in the range from 94°C to 122°C. Although this method sometimes requires an operation temperature point far from room temperature, it enables very high conversion efficiency at low pump power. Maximum efficiency up to 9% was obtained at coupled pump power of only 30 μW, as shown in Fig. 8(b). Recently, NCPM-based SHG using WGMRs made from lithium tetraborate ($Li_2B_4O_7$ or LB_4) was reported for efficient CW UV harmonic light generation at 245 nm [70].

Besides the selection rule from the formerly mentioned phase matching condition of $m_1 = 2m_2$ in WGMRs, additional conditions have to be imposed when considering the 3D picture of light in WGMRs. To assure efficient three-wave coupling in the resonator, one also has to consider the cross-section overlap between the resonant pump and harmonic modes, especially in large resonators. In a spherical WGMR, these rules have been derived as $p_2 \leq 2p_1$, where $p_{1,2} = 0, 1, 2\ldots$ are the polar mode numbers [69].

3.1c. Orientation-Based Cyclic Phase Matching

Although high conversion efficiency for CW SHG has been demonstrated with a low-power pump laser using either quasi-PM or naturally PM in WGMRs, these methods have specific requirements. For instance, quasi-PM requires ferroelectric nonlinear materials. On the other hand, NCPM has a specified phase matching spectral range determined by the material. Research efforts have then been devoted to asymmetric crystalline resonators, such as angle-cut beta barium borate (BBO) WGMRs [82]. In 2013, Lin *et al.* demonstrated a crystal orientation-based birefringent *cyclic* phase matching method in a WGMR made from BBO [71]. This method provides another way for efficient SHG in large WGMRs, as illustrated in Fig. 6(c). The phase

Figure 8

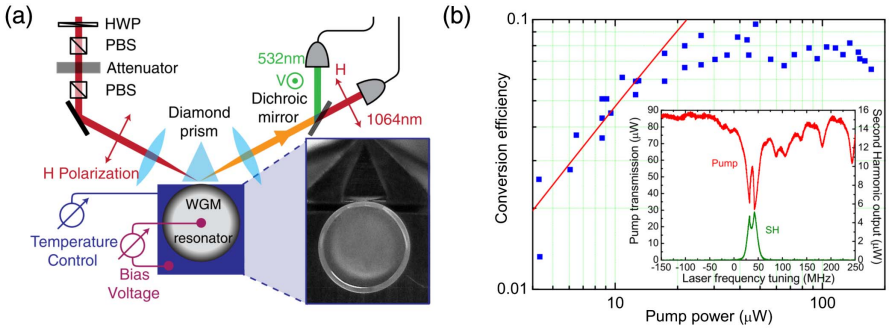

Natural phase matching in SHG with MgO-doped $LiNbO_3$ WGMRs. (a) Schematic of experimental setup. (b) Conversion efficiency as a function of the pump power. Inset: transmitted pump and harmonic signals as a function of the pump frequency. Figures 3 and 5 reprinted with permission from Fürst, *et al.*, Phys. Rev. Lett., **104**, 153901 (2010) [69]. Copyright 2010 by the American Physical Society.

matching spectral range is broader but at the expense of reduced efficiency, as listed in Table 1.

Such BBO WGMRs were cut out from an X-cut or XY-cut wafer so that the crystal orientation breaks the symmetry of a WGMR. In this configuration, the optic axis lies in the equatorial plane of the disk, as shown in Fig. 9(a). Similar to Z-cut uniaxial crystalline WGMRs, the resonant modes still feature either TE or TM polarizations. However, as light travels along the circumference, the TM mode encounters an oscillating refractive index, which can be estimated as

$$\frac{1}{n_{\mathrm{TM}}^2(\lambda,\varphi)} = \frac{\cos^2(\varphi)}{n_o^2(\lambda)} + \frac{\sin^2(\varphi)}{n_e^2(\lambda)}. \tag{2}$$

Considering TE modes for pump and TM modes for harmonic, discrete phase matching positions can be formed due to the nature of TM modes whose refractive indices oscillate from ordinary to extraordinary ones. An example is shown for the pump around 1557 nm in Fig. 9(b). Within one round trip, there are four or two (in degenerate cases) locations where $\Delta k(\varphi_i) = 0$ occurs. In this case, Eq. (1) governs the growth of the harmonic field and can be rewritten as follows [71]:

$$\frac{dE_2}{dz} = \frac{ik_2(z)}{n_2(z)^2}\chi^{(2)}(z)E_1^2 \exp\left[i\int_0^z \Delta k(z)\mathrm{d}z\right]. \tag{3}$$

Numerical simulations based on this equation reveals that the harmonic field can grow constructively or destructively within the whole birefringent phase matching range of the crystal [71]. These regimes depend on the wavelengths and can be tuned by choosing high-order WGMs with different effective indices. Although the *cyclic* phase matching feature comes at the price of a reduced efficiency when compared with the two other methods, it provides a new approach for SHG using WGMRs and has potential applications for generating vacuum UV lasers considering KBBF crystals as the host material. Recently, SHG based on a *cyclic* phase matching method in a $LiNbO_3$ microdisk cavity was also reported [72].

Figure 9

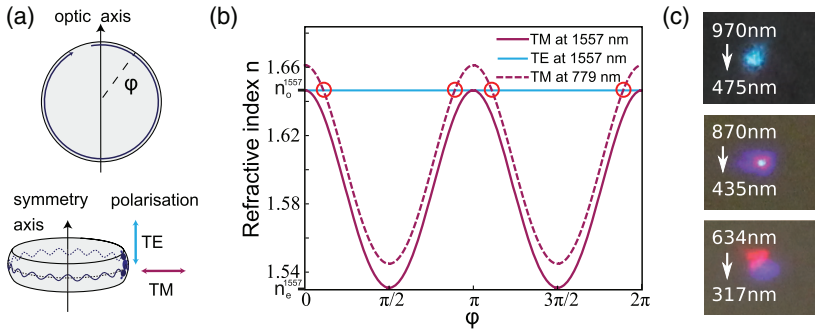

Orientation-based cyclic birefringent phase matching in SHG with a X-cut or XY-cut BBO WGM resonator. (a) Schematic of the BBO disk in the XY-cut geometry. (b) Refractive indices along the circumference for the pump and harmonic waves. (c) Photographs of second-harmonic light output on a sheet of paper with different pump wavelengths in the same disk. Note that the visible second-harmonic at 317 nm is due to its fluorescence on paper. Reprinted from [71], with the permission of AIP Publishing.

3.1d. Modal and 4-Bar Phase Matching

In small optical resonators, the radial mode order has a great impact on the effective refractive index. The resulting modal dispersion can be large enough to compensate for the bulk material dispersion between pump and harmonic waves. Recently, modal phase-matched SHG has been successfully demonstrated based on chip-scale micro-ring (racetrack) resonators made from GaN [83], Si_3N_4 [84], and AlN [85,86]. Similarly, it can also be used for small size WGMRs, such as microdisk or micro-cylinders [76–78]. It should be noted that nonlinear thermal effects also appears in such integrated microresonators, for instance, in $LiNbO_3$ microdisks [87,88]. In addition, a natural quasi-phase matching method can also be applied based on the orientation of $\bar{4}3m$ or $\bar{4}2m$ crystals with respect to the disk symmetry. This method referred to as $\bar{4}$ quasi-phase matching was first theoretically studied [89,90] and experimentally demonstrated on a GaAs microdisk by Kuo *et al.* [73].

An example of a GaAs microdisk is shown in Fig. 10, left. The orientation of the crystal is chosen such that the $\bar{4}$-axis is perpendicular to the disk plane (or 001-cut). In this case, the light experiences an effective domain inversion period of 2 when it travels along the circumference for one round trip. Such a quasi-phase matching condition thereby corresponds to the case $m_2 = 2m_1 \pm 2$ (that is, $M = \pm 2$). For a small microdisk, the large modal dispersion can lead to a small phase mismatch or a small value of $\Delta m = m_2 - 2m_1$, which can then be compensated by $\bar{4}$ quasi-phase matching. For the GaAs microdisk with a diameter of 5.2 μm and a thickness of 160 nm, a TE WGM with $q = 1, m = 13$ at the pump wavelength of 1985 nm and a TM WGM with $q = 2, m = 24$ at the harmonic wavelength were found [73]. Figures 10(a) and 10(b) give the corresponding calculated WGM field distribution for the pump and second-harmonic waves using finite-difference time-domain (FDTD) methods, showing the employment of modal dispersion. Subsequently, harmonic generation was observed with efficiency curve as a function of the fundamental pump power, shown in Fig. 10(c). Recently, $\bar{4}$ quasi-phase matched SHG has also been demonstrated on other crystalline microdisks made from AlGaAs and GaP [74,75]. Theoretically, an antiphase domain tailoring method was also proposed for SHG using a GaP microdisk [91].

Figure 10

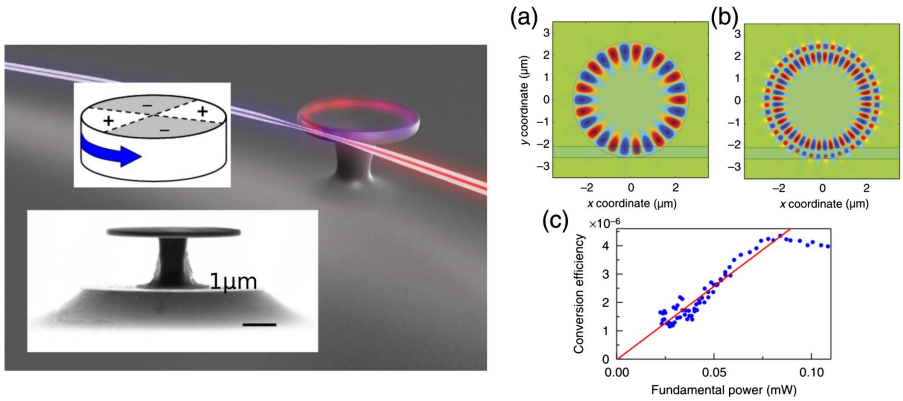

Modal phase matching and $\bar{4}$ quasi-phase matching in a small GaAs microdisk. Left: schematic and SEM image of the microdisk. Top right: calculated WGM field amplitude distribution for the pump and SH waves. Top bottom: conversion efficiency as a function of the pump power. Reprinted by permission from Macmillan Publishers Ltd.: Kuo *et al.*, Nat. Commun., **5**, 3109 (2014) [73]. Copyright 2014.

3.1e. Tuning Methods for Phase-Matched CW SHG in WGMRs

We have reviewed different phase matching methods for SHG with both pump and harmonic fields resonant in WGMRs. Compared to nonresonant or singly resonant SHG, the doubly resonant condition can greatly enhance SHG in high-Q WGMRs with very low pump power. However, high conversion efficiency comes at the price of limited tunability. In WGMRs, optical modes can be tuned in several ways through electro-optic effect, thermal- or stress-induced size, and refractive index changes [11]. Precise control on the size of the microdisks or the coupling gap between the coupler and resonator can also change the resonant conditions [78]. Theoretical investigations of the dependence of SHG efficiency on the coupling strength regarding to the ratio of coupling to intrinsic Q-factors or to the temperature change have also been carried out [92,93].

Due to noncoordinate optical frequency shifts at pump and harmonic modes, the single tuning method usually leads to a limited continuous tuning bandwidth. To tune the harmonic signal continuously and widely, combined tuning methods can be used. For instance, both temperature and stress tuning methods have been applied simultaneously for a 317 nm UV laser generated from a BBO WGMR [94]. Figure 11(a) shows the tuning spectra of SHG in such a resonator with a piezo applied for stress tuning. The top curves show the resonance shift spectra of the pump mode, while the bottom curves are the corresponding harmonic output signals. A 3 dB bandwidth of 1 GHz at the pump was then shown, corresponding to an applied voltage tuning on a piezo of 6 V. The maximum conversion efficiency is obtained when the spectral mismatch $\Delta\lambda^{\mathrm{WGM}}$ equals 0. For temperature tuning, a similar 3 dB tuning range of 0.2°C was reported. If one combines both tuning methods, the spectral mismatch during the tuning can be self-compensated, leading to a mode-hop-free tuning situation, as shown in Fig. 11(b), with at least 35 times larger tuning range.

3.2. Optical Parametric Oscillations

Optical parametric oscillations (OPOs) based on second-order nonlinearity is another interesting three-wave mixing parametric process, where one pump photon is converted into one signal and one idler photons. The corresponding energy and momentum conservation laws are expressed as $\omega_{\mathrm{p}} = \omega_{\mathrm{s}} + \omega_{\mathrm{i}}$ and $\mathbf{k}_{\mathrm{p}} = \mathbf{k}_{\mathrm{s}} + \mathbf{k}_{\mathrm{i}}$, where the sub-indices p, s, and i represent the pump, signal, and idler waves. In contrast to SHG, this process is a parametric downconversion (PDC) that generates optical photons with

Figure 11

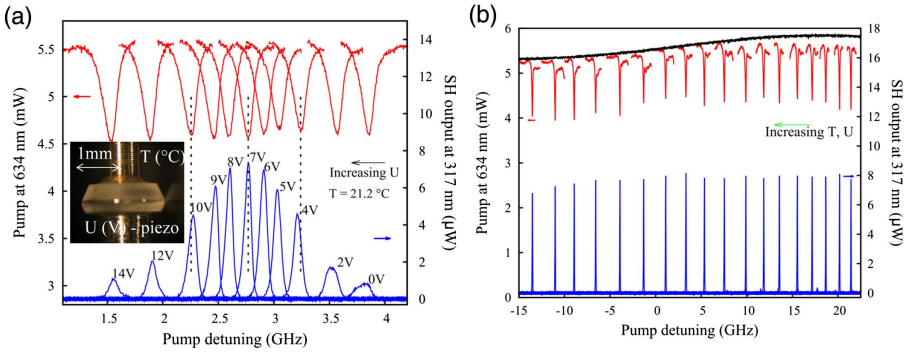

Continuous mode-hop-free tuning of harmonic light at 317 nm with a BBO WGM disk. (a) Tuning spectra with increasing voltage applied on the piezo. (b) Tuning spectra with simultaneously increasing the temperature (ΔT is 0.2°C) and piezo voltage (ΔU is about 6 V). Reprinted from [94]. Copyright 2014 Optical Society of America.

longer wavelengths. It can be applied for mid-IR coherent light generation and broadband spectroscopy.

With high-Q WGMRs, the triply resonant condition can greatly enhance such processes. The key condition to enable efficient OPO lies on the phase matching condition. Similar to doubly resonant SHG in WGMRs, the phase matching condition can be written in the forms of azimuthal mode numbers of WGMs following $m_p = m_s + m_i + j$, where j is an harmonic integer [62]. For naturally phase matching, j becomes 0. For quasi-phase matching, j is then a nonzero integer. Additional conditions required by mode overlap should also be satisfied [95]. In spheroidal WGMRs, they are expressed by the polar mode orders p as $p_p \le p_i + p_s$ and $p_p + p_s + p_i = 0, 2, 4\ldots$. The threshold power for phase-matched OPO can then be estimated as [96]

$$P_{th} = \frac{\omega_p \varepsilon_0 n_p^2 n_s^2 n_i^2}{32 d^2} \frac{V_p V_s V_i}{V_{psi}^2 Q_p Q_s Q_i} \frac{(1 + r_p)^2 (1 + r_s)(1 + r_i)}{r_p}, \tag{4}$$

where d is the effective nonlinear coefficient, $n_{p,s,i}$ are the refractive indices, V_{psi} is the mode overlap volume, $V_{p,s,i}$ are the mode volumes, $Q_{p,s,i}$ are intrinsic Q-factors, and $r_{p,s,i}$ are the ratios between the coupling coefficient and the round-trip losses.

Until now, high-Q WGMR-based OPO experiments have been demonstrated with millimeter-size nonlinear crystalline resonators [95–103]. CW threshold power as low as 6 μW was demonstrated using the naturally phase matching method [95] in 2010. Figure 12(a) shows the observation of the pump and OPO signals with the pump frequency scanned across a WGM in such experiments. Due to the efficient conversion of the pump into the OPO signals, the resulting depletion of pump alters its Lorentzian resonance. In this figure, it can be found that the threshold and coupling efficiency depend on the coupling gap, as expected from the theoretical analysis [92]. Thereby, balances have to be found depending on the different applications. Conversion efficiency larger than 55% was recently observed with a threshold power of 2 mW, achieved in an over-coupled resonator [101]. Tunable OPO has also been demonstrated with quasi-phase matching in a radially poled $LiNbO_3$ resonator, as shown in Fig. 12(b). Depending on the pump wavelengths (from visible to infrared light), OPO signals from 571 nm to 2600 nm have been generated [62]. The advantages of quasi-phase matching include the fact that larger effective nonlinear coefficients can be exploited and its versatile tunability based on the modes involved (different polarization or mode numbers) [102]. Recently, WGMR-based OPO has been applied for broadband spectroscopy [99]. Below threshold, it can also generate bright heralded single photons [104]. The subsequent application with the coupling of such photon pairs to alkali dipole transitions was also demonstrated [100].

3.3. Sum-Frequency Generation

As the reverse process of OPO, nondegenerate SFG based on the second-order nonlinearity also requires a triply resonant condition in WGMRs. Similarly, the phase matching condition in the form of WGM mode numbers is expressed as $m_1 + m_2 + j = m_3$, where $m_{1,2,3}$ represent the azimuthal mode numbers, j is 0 for natural phase matching and a nonzero integer for quasi-phase matching. However, with two pump lasers at different frequencies which should be simultaneously resonant, such experiments are more difficult to design and carry out. SFG in high-Q WGMRs were experimentally observed in cascaded nonlinear processes where only one pump laser is used. It has been observed in third-harmonic generation resulting from the cascading of SHG and SFG in radially poled and linearly poled disks [65,81].

SFG has also been reported in OPO experiments where the PDC and pump photons in infrared are summed into visible photons [98]. In 2014, Strekalov *et al.* demonstrated SFG in a $LiNbO_3$ resonator using the natural phase matching method, with two pump lasers at 1560 nm and 780 nm [105]. It should be noted that SFG based on the third-order nonlinearity has also been observed.

4. KERR EFFECTS

In a centrosymmetric material, the nonlinear motion of the electron clouds under the influence of an electromagnetic wave cannot result in an even-order nonlinear polarization. The first higher-order term in the Taylor expansion of the polarization is therefore the third, and the material polarization can be expressed as $P^{(3)}(t) = \varepsilon_0 \chi^{(3)} E^3(t)$, where $\chi^{(3)}$ is the third-order nonlinear susceptibility of the medium. The susceptibility $\chi^{(3)}$ is usually negligible compared to $\chi^{(2)}$, such that third-order effects are hardly visible in noncentrosymmetric materials. The tensor nature of the nonlinear susceptibility implies a threefold interaction between the different components of the electric field. This additional complexity compared to the second-order nonlinearity can give rise to various nonlinear effects.

4.1. Third-Harmonic Generation

Third-order sum-frequency generation and its degenerate version, THG, is one of the nonlinear effects stemming from the third-order susceptibility. It consists of three

Figure 12

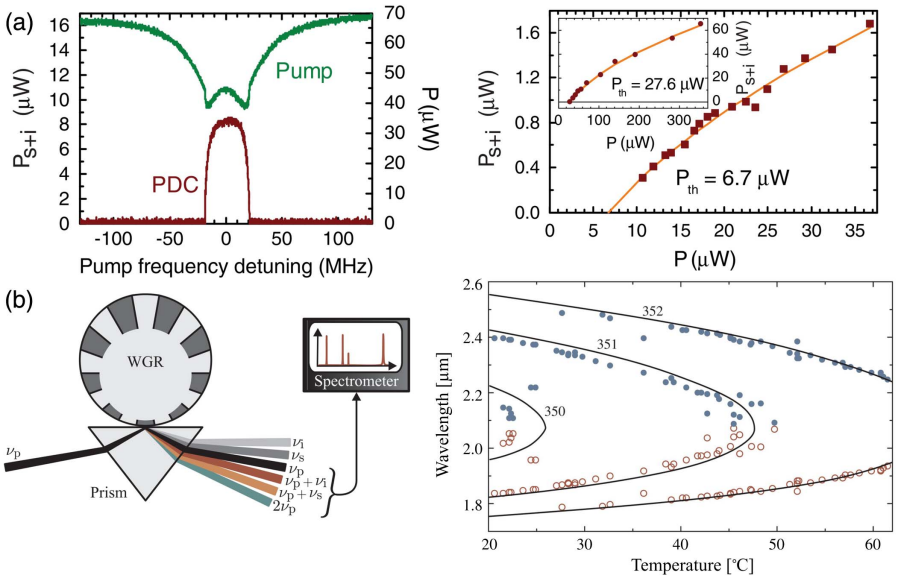

Experimentally demonstrated WGMR-based OPO using (a) natural phase matching and (b) quasi-phase matching: (a) Left: pump and OPO signals as a function of pump frequency detuning. Right: OPO output as a function of in-coupled pump power for critically coupled (inset) and under-coupled condition. Figures 4 and 5 reprinted with permission from Fürst *et al.*, Phys. Rev. Lett., **105**, 263904 (2010) [95]. Copyright 2010 by the American Physical Society. (b) Left: schematic of experimental setup using an off-center radially poled $LiNbO_3$ disk resonator. Right: experimentally observed signal and idler wavelengths (open and closed dots) as a function of temperature. Solid lines are the calculated tuning curves for $j = 350, 351, 352$. Figures 3 and 5 reprinted with permission from Beckmann *et al.*, Phys. Rev. Lett., **106**, 143903 (2011) [98]. Copyright 2011 by the American Physical Society.

photons interacting in the dielectric material to produce a single photon with different frequency. Similarly to the second-harmonic generation in noncentrosymmetric material, the energy conservation law has to be verified: $\omega_t = \omega_1 + \omega_2 + \omega_3$, where ω_t is the frequency of the output photon and $\omega_{1,2,3}$ are the frequencies of the input photons. For this third frequency generation to be efficient, the pump and generated frequency should be phase matched so as to preserve the total momentum. This translates as having all the interacting electromagnetic waves propagating at the same speed, that is the effective indices of each wave should be equal: $n_1^{\text{eff}} = n_2^{\text{eff}} = n_3^{\text{eff}} = n_t^{\text{eff}}$. In whispering-gallery mode resonators, an additional requirement imposes that the pump and created light have to resonate in the WGMR. When this condition is fulfilled, the interaction is enhanced by the high quality factor of the resonator. These three conditions are quite difficult to fulfill simultaneously, and a solution has recently been proposed, making use of the different spatial modes of a WGMR. Using the intermodal dispersion of higher-order modes in silica microspheres and microtoroids, efficient frequency conversions based on the third-order susceptibility was experimentally demonstrated [106–108]. Third-harmonic generation can also be observed in conjunction with other $\chi^{(2)}$ and $\chi^{(3)}$ interactions, namely second-harmonic generation [109], Raman scattering [110], four-wave mixing (FWM), and frequency combs [111–113].

4.2. Kerr Optical Frequency Combs

4.2a. Four-Wave Mixing in WGMRs

In the presence of Kerr nonlinearity, the refractive index of the material can be written as $n(I) = n_0 + n_2 I$, where n_0 is the linear index of the material, obtained when the optical power remains low, $n_2 = 3\chi^{(3)}/(2n_0^2\varepsilon_0)$ is the nonlinear index of this material, and I is the intensity (irradiance) of the electromagnetic wave [68]. This effect is often referred to as the *Kerr effect*, and leads to a variety of nonlinear processes where the newly generated frequencies can remain close to the pump frequency, especially self-phase modulation and FWM. Provided the material and geometric dispersions remain small, the conservation of the momentum condition is naturally fulfilled, and the system can fully take advantage of the resonant nature of the WGMRs to efficiently generate new frequencies. This same resonant nature of the WGMR also imposes that the newly created frequencies are discrete, and one can expect the formation of a frequency comb.

A Kerr optical frequency comb is a set of equidistant spectral lines generated in a high-Q dielectric WGMR via its Kerr nonlinearity. In a typical Kerr comb generation setup such as the one shown in Fig. 13(a), the light from a continuous-wave laser is coupled in the WGMR close to a resonance of azimuthal order ℓ_0. In the simplest and most widespread case, Kerr combs only involve azimuthal modes belonging to the *same* family. As a consequence, all the interacting modes can be unambiguously labeled by their azimuthal eigennumber ℓ. It is convenient in that case to introduce the reduced eigennumber $l \equiv \ell - \ell_0$, such that the pumped mode is $l = 0$ while the side modes symmetrically expand as $\pm 1, \pm 2, \ldots$. When the resonator is pumped above a given threshold, the resonant enhancement of the pump light triggers nonlinear effects, such as, for example, degenerate four-wave mixing, which leads to the generation of two first comb lines following $2\omega_0 = \omega_{-l} + \omega_l$, where ω_0 is the eigenfrequency of the pumped mode, and $\omega_{l,-l}$ are those of the excited side modes. In this context, it is common to label ω_{-l} as the *idler*, and ω_l as the *signal*. Since only resonant modes can be excited within the WGMR, the whole process leads to the frequency conversion from the pump to two symmetrical modes of the WGMR, separated from the pump by the same integer number of FSRs. From here, a complex set of interactions between the different modes of the WGMR arises through four-wave mixing in the dielectric

material. As per usual, the energy has to be preserved, which translates to the *non-degenerate* FWM interactions $\omega_m + \omega_p = \omega_n + \omega_q$, where $\omega_{m,p,n,q}$ are the different interacting comb lines (note that here, m, n, and p are reduced azimuthal eigennumber, unlike in Subsection 2.1b). By cascading this process, one can eventually obtain a whole frequency comb with hundreds or thousands of comb lines spanning an entire octave. This intuitive explanation of Kerr comb generation is summarized in Fig. 13(b).

In 2004, pioneering experiments reported the generation of optical hyperparametric oscillations in silica microtoroids and CaF_2 WGMRs [34,49], revealed by the excitation of a couple mode on each side of the pump mode. This corresponds to the phenomena involved in degenerate four-wave mixing, with three modes corresponding to pump, signal, and idler waves. Interestingly, WGMRs only needed power levels in the milliwatt range to exhibit substantial four-wave mixing owing to their high-Q resonances.

Three years after these first contributions, a decisive breakthrough was achieved owing to a seminal experiment that demonstrated massively cascaded hyperparametric interactions, yielding a broadband Kerr comb with several tens of sidebands for the first time [36]. This foundational work was an important milestone because it provided unambiguous proof that the topic of Kerr optical frequency combs could be bridged to time-frequency metrology. Subsequently, Kerr combs have been reported in various WGMR geometries, various materials, with comb line spacings ranging from a few gigahertz to several terahertz, with central wavelengths going from the visible [114] to the mid-infrared [115,116], and spanning as wide as an octave [117,118]. The choice of material is mainly guided by its intrinsic loss and ability to be shaped into a WGMR with very high quality factors. Fused silica is therefore frequently used [34,36,47,119,120], its amorphous nature allowing the formation of various resonators while keeping a very small surface-tension controlled roughness. Silica WGMRs are limited to Q-factors in the 10^8 range due to hydroxyl bonds on their surfaces. The intrinsic transmission range of SiO_2 also stops at around 2.8 μm making it not suitable for comb generation in the mid-infrared region. For higher quality factors and extended transmission in the infrared, fluoride crystals have been the materials of choice for Kerr comb generation [46,49,50,55,121,122]. CaF_2, MgF_2, and SrF_2 all feature transmission windows from about 100 nm in the UV to 10 μm in the IR, and can be shaped and polished into WGMRs with quality factors up to 10^{11}. Such high Qs reduce the threshold for comb generation to power levels easily obtainable in

Figure 13

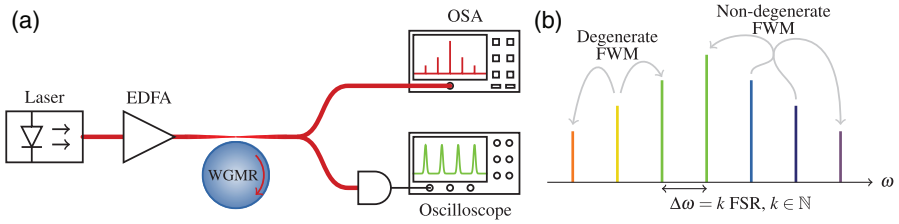

(a) Typical experimental setup for the generation of a Kerr frequency comb in a WGMR. A continuous-wave laser is used to pump a resonance of the WGMR, and the newly generated frequencies can be observed, analyzed, and used for ulterior purposes. (b) Intuitive explanation of the processes leading to the generation of a Kerr frequency comb, with degenerate and nondegenerate four-wave mixing that leads to the formation of equidistant spectral lines.

the lab. Kerr frequency combs have also been generated in on-chip ring resonators in high-index silica glass [123], silicon on insulator [116,124], diamond [125], aluminum gallium arsenide on insulator [126], aluminum nitride [127,128], or silicon nitride [41–43,117,129,130], this latter material benefiting from very low absorption losses at the telecom wavelength. In these cases, the lower Q-factors compared to bulk resonators (in the 10^6 range) are compensated by smaller mode volumes, higher field confinement, and larger nonlinearity, allowing for comb generation at reasonably low pump power.

4.2b. Theoretical Description

The numerous experimental results reported in the literature show that Kerr combs can be generated in different materials, with resonators of different shapes, suggesting that a global description of the processes at stake is possible. Furthermore, the combs come in all sort of shapes and frequency spans, hinting at very rich and diverse dynamics (see [131] and references therein).

The earliest theoretical models for the description of Kerr comb generation were based on the so-called *modal-expansion formalism*, where the dynamics of each mode is described by an ordinary differential equation. This approach allowed explanation of hyperparametric optical oscillations via the excitation of few modes around the pump [34,49,132]. The generalization of the modal expansion approach for an arbitrary number of modes followed shortly after [133–135], and permitted for the first time simulation of the dynamics of wide-span combs including several hundreds of modes. The modal model considers the evolution of the slowly varying complex amplitude (or envelope) of each mode in interaction with all the others through four-wave mixing, and can be explicitly written as

$$\frac{d\mathcal{E}_l}{dt} = -\frac{1}{2}\Delta\omega_{\text{tot}}\mathcal{E}_l + i\sigma\mathcal{E}_l - i\left[\sum_{k=2}^{K}\frac{\zeta_k}{k!}l^k\right]\mathcal{E}_l + \delta(l)\sqrt{\Delta\omega_{\text{ext}}/T_{\text{FSR}}}\sqrt{P_{\text{L}}} + iv_{\text{g}}\gamma\sum_{m,n,p}\delta(m-n+p-l)\mathcal{E}_m\mathcal{E}_n^*\mathcal{E}_p, \tag{5}$$

where $\mathcal{E}_l(t)$ is the field envelope of the mode of azimuthal order l, normalized such that $|\mathcal{E}_l|^2$ is the corresponding power in watts. The Kronecker function $\delta(x)$ equals 1 for $x = 0$ and 0 elsewhere. The parameters for the linear part of this equation are the frequency detuning $\sigma = \omega_{\text{L}} - \omega_0$ between the laser and the resonance frequency of the pumped mode, the total and external (in-coupling) bandwidths $\Delta\omega_{\text{tot}} = \omega_0/Q_{\text{tot}}$ and $\Delta\omega_{\text{ext}} = \omega_0/Q_{\text{ext}}$, the intra-cavity round-trip time $T_{\text{FSR}} = 2\pi/\Omega_{\text{FSR}}$, the k-th order dispersion parameters ζ_k introduced in Subsection 2.1b, and the laser pump power P_{L}. The FWM term induces a global coupling and is weighted by the nonlinear parameter $\gamma = n_2\omega_{\text{L}}/cA_{\text{eff}}$, where n_2 is the Kerr nonlinearity (proportional to $\chi^{(3)}$), and $A_{\text{eff}} = V_{\text{eff}}/L$ is the effective mode area inside the resonator, with L being its perimeter. The parameter $v_{\text{g}} = c/n_{\text{g}}$ stands for group velocity in the resonator at the pump frequency. This modal expansion model was originally written in terms of the variables $\mathcal{A}_l = \sqrt{T_{\text{FSR}}/\hbar\omega_{\text{L}}}\mathcal{E}_l$, which are such that the square modulus $|\mathcal{A}_l|^2$ stands for the intra-cavity photon number in the mode l. In that case, the relevant nonlinear coefficient is $g_0 = n_2c\hbar\omega_{\text{L}}/n_0^2V_{\text{eff}}$, which stands for the Kerr phase shift induced by one photon, n_0 being the refraction index at ω_0. Evaluating the intra-cavity field in terms of photons becomes useful at the time to investigate the quantum properties of Kerr combs [136,137]. It is important to note that the above model assumes spatial degeneracy of the azimuthal modes, and assumes as well that their losses are the same. These assumptions are valid as long as the spectral extension of the comb is not too large ($\ll \omega_0$).

This modal approach is especially convenient to determine the threshold value of the intra-cavity: for critical coupling and under the simplifying assumptions that the Q-factor does not depend on the mode number, the absolute minimum pump power required to generate a comb is given by [34,132,134,138]

$$P_{\mathrm{th}} = \frac{\omega_{\mathrm{L}} n_0^2 V_{\mathrm{eff}}}{4 c n_2 Q^2} \propto \frac{1}{n_2} \frac{V_{\mathrm{eff}}}{Q^2}, \tag{6}$$

where Q is the loaded quality factor. This threshold is a minimum requirement under which no comb is generated, no matter what are the values of the other parameters such as the detuning and the dispersion. The threshold power is inversely proportional to the nonlinear index and to the square of the quality factor, confirming the experimental choice of low-loss material as opposed to highly nonlinear ones. Another noteworthy feature is that small volume resonators will generate comb at lower input powers, as it could be expected. It should be noted as well that pumping the WGMR above the absolute minimal threshold defined by Eq. (6) is a necessary but not sufficient condition to trigger Kerr comb generation [134,139].

Another approach has been developed that considers the nonlinear propagation of the whispering-gallery modes in the time domain, in a similar fashion to what is done in optical fibers with the nonlinear Schrödinger equation (NLSE) [119]. These models require the numerical simulation of millions of round trips to account for the extremely high Q of the WGMR; however, the time-domain description can be refined and simplified using the valid approximation that the electromagnetic field envelop is only slightly modified from one round trip to the other (slowly varying envelope approximation). Under this assumption, the description of the system can be brought down to the following partial differential equation [131,140–142], which is generally referred to as the generalized Lugiato–Lefever equation (LLE):

$$\begin{aligned} \frac{\partial \mathcal{E}}{\partial t} = &-\frac{1}{2}\Delta\omega_{\mathrm{tot}}\mathcal{E} + i\sigma\mathcal{E} + i v_{\mathrm{g}} \sum_{k=2}^{K} (i\Omega_{\mathrm{FSR}})^k \frac{\beta_k}{k!} \frac{\partial^k \mathcal{E}}{\partial \theta^k} + i v_{\mathrm{g}} \gamma |\mathcal{E}|^2 \mathcal{E} \\ &+ \sqrt{\Delta\omega_{\mathrm{ext}}/T_{\mathrm{FSR}}}\sqrt{P_{\mathrm{L}}}, \end{aligned} \tag{7}$$

where $\mathcal{E}(\theta, t) = \sum_l \mathcal{E}_l(t) e^{il\theta}$ is the envelope of the total intra-cavity field, which depends on the azimuthal angle along the closed-path circumference of the resonator $\theta \in [-\pi, \pi]$ and on the time variable t. In this equation, the dispersion coefficients are now expressed in terms of $\beta_k = -\zeta_k/(-\Omega_{\mathrm{FSR}})^k v_{\mathrm{g}}$, which can be related to the Taylor series expansion of the propagation constant $\beta(\omega)$. It can be shown that Eq. (7) is strictly equivalent to the modal description of Eq. (5) by means of a simple Fourier transform [141].

The LLE is a variant of the NLSE with periodic boundary conditions, and efficient algorithms such as the split-step Fourier algorithm are particularly suitable for its numerical simulation.

When dispersion is limited to the second order, this equation mathematically corresponds to the one that was originally derived by Lugiato and Lefever in the context of spatial dissipative structures in cavity optics [143]. The LLE was later reintroduced for the study of dispersive ring cavities by Haelterman, Trillo, and Wabnitz [144]. It is interesting to note that the stability analysis of the LLE was first performed in the context of mathematical physics [145,146], and then in the context of Kerr combs [139,147]. It allowed us to understand the complex interactions leading to the

generation of Kerr combs, and the identification of various spatiotemporal structures within the WGMR.

4.2c. Regimes of Kerr Frequency Combs

The various types of combs that have been experimentally observed so far generally correspond to Turing rolls, (multi-)solitons, breathers, or spatiotemporal domain, as displayed in Figs. 14 and 15.

The first experimental combs reported were most of the time corresponding to Turing rolls (patterns). They are very often labeled by various different names [36,49,119,121,134], such as optical parametric oscillations, primary combs, modulation instability, etc. The line spacing of these combs consist of an integer number of FSRs [148,149], as shown in Fig. 16, and that translates into a series of equidistant rolls (pulses) distributed within the WGMR. These Turing rolls can be connected to the cnoidal waves that arise as asymptotic solutions of the LLE in the lossless cavity limit [150]. It was found that they could be generated in both normal and anomalous regimes of dispersion [139,151]. As shown in Figs. 14 and 15, their bifurcation structure was analyzed and found to lead to chaotic regimes in the anomalous regime and numerical simulations were able to predict their behavior with a very good accuracy [152], as displayed in Fig. 17.

The analysis of the LLE predicts that localized structures such as cavity solitons can be stationary solutions given appropriate parameters [141,153]. Later on, experiments confirmed this theoretical prediction: its optical spectrum [154], dependency on the pump power [155], and detuning or time duration [154–156] have been characterized and successfully compared to numerical simulations or analytical approximations, as

Figure 14

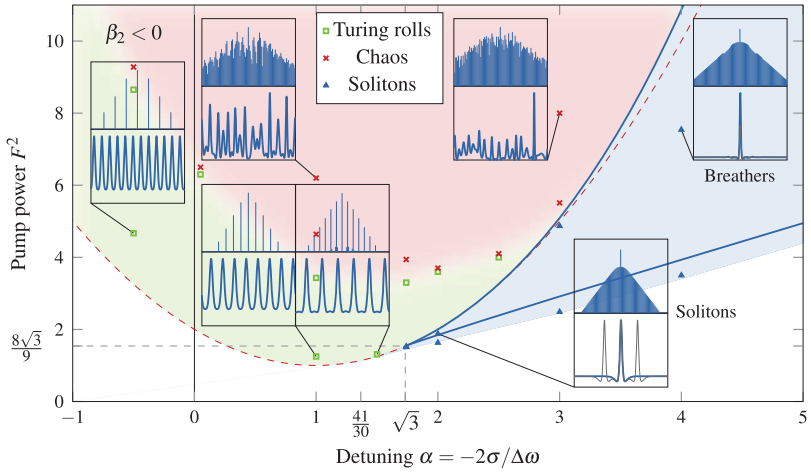

Bifurcation diagram of the Lugiato–Lefever equation in the anomalous dispersion case $\beta_2 < 0$. The normalized detuning $\alpha = -2(\omega_L - \omega_0)/\Delta\omega_{tot}$ and the normalized pump power $F^2 = (8g_0\Delta\omega_{ext}/\Delta\omega_{tot}^3)(P_L/\hbar\omega_L)$ are the two parameters available during an experiment and therefore make up the axis of the diagram. In the white region at low pump powers, only the steady-state solution is stable. Turing patterns (green area) are generated above the threshold (red dashed line) and evolve into chaos at even higher excitation (red region). The soliton solutions appear for larger positive detunings α, in the blue region. At higher excitation, they evolve to nonstationary breathing solutions. Adapted with permission from [139]. Copyright 2014 by the by the American Physical Society.

shown in Fig. 18. The spectrum of the soliton presents a smooth hyperbolic secant shape [157], making this comb particularly useful for potential applications. Kerr soliton generation is, however, challenging for various reasons. First, the soliton can only appear when the pump frequency is smaller than the pumped resonance (i.e., on the red side of the resonance, $\Omega_0 < \omega_{\ell_0}$). This proves difficult because thermal nonlinearities render this side of the resonance unstable. Second, the soliton emerges in a multi-stability area, where the absence of comb is a stable solution of the LLE, and solutions with several solitons (provided they do not interact with each other) are also stable [139]. For these reasons, in the simple case where the pump wavelength is swept across the resonance, the system evolving from Turing patterns to chaos, multiple solitons states and, finally, to a single soliton [158], can almost never be achieved. More advanced schemes have been proposed and demonstrated experimentally: fast wavelength tuning to circumvent thermal instability [154,159], slow wavelength tuning combined with careful pump power modifications [160], fast pump power changes coupled with wavelength locking techniques [161], phase or amplitude modulation of the pump [162], and backward wavelength tuning [163]. If multiple solitons are present in the cavity, they can strongly interact due to mode-coupling, and self-organize to form soliton crystals [164–166], leading to rich and complex dynamics and a wide variety of phase-locked frequency combs. Experiments and theoretical studies have shown that the generation of the soliton can be facilitated by an appropriate dispersion including higher-order dispersion terms [167,168], and more importantly, by avoiding crossings with other spatial mode families [154,169]. It should also be noted that research remains very active for the understanding of the Kerr soliton dynamical properties, as well as for their control in view of technological applications in photonics [170–174].

In the normal dispersion regime, localized structures can also be generated in the form of dark pulses [139,175] resulting from the stabilization of two switching waves [176]: switching waves connect the upper and lower continuous-wave solutions of the LLE, and can undergo stabilizing interactions to form one or several localized dips.

Figure 15

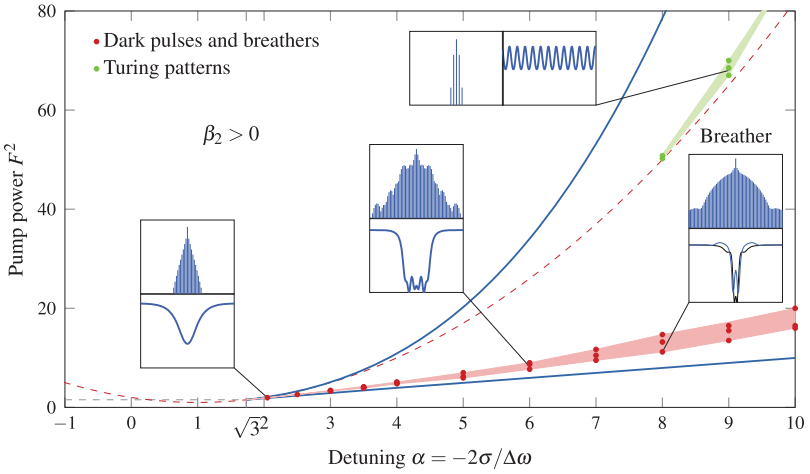

Bifurcation diagram of the Lugiato–Lefever equation in the normal dispersion case $\beta_2 > 0$. In this case, Turing patterns with multi-FSR spacings can spontaneously arise from noise above the red dashed line when the detuning is large. Dark pulses and dark breathers can be excited in the red region. Adapted with permission from [139]. Copyright 2014 by the American Physical Society.

The theoretical conditions required for the generation of such structures are quite difficult to match: the region of the parameter space where they are stable is quite restricted (see Fig. 15), and similarly to the case of the bright soliton, it needs a seed to grow from, since the continuous-wave background is also a stable solution in this region [139,176]. As these dark structures come from the subtle interaction and stabilization of two switching waves, the seed needs to be particularly well chosen. Despite all these difficulties, dark localized structures have been recently observed in WGMR [177–181], as shown in Fig. 19. The spectrum of such structures is very distinctive, as shown in Fig. 19, and numerical simulations of the LLE accurately reproduce the experimental results [178,180]. In these experiments, modulation instability and mode coupling are likely responsible for the seeding and stabilization of the

Figure 16

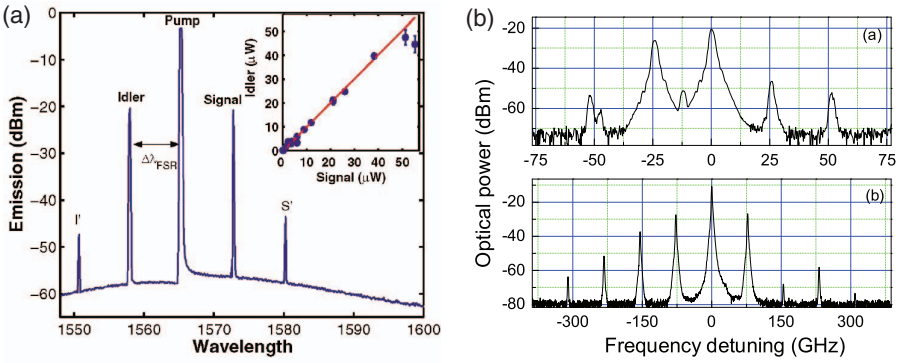

(a) First experimental generation of a Kerr frequency comb corresponding to an optical parametric oscillation. Figure 3 reprinted with permission from Kippenberg *et al.*, Phys. Rev. Lett., **93**, 083904 (2004) [34]. Copyright 2004 by the American Physical Society. (b) Experimental spectra of two Turing patterns with different line spacings corresponding to different integer numbers of FSR. Both combs were generated using the same resonator and pumping at different detunings. Figure 2 reprinted with permission from Savchenkov *et al.*, Phys. Rev. Lett., **101**, 093902 (2008) [148]. Copyright 2008 by the American Physical Society.

Figure 17

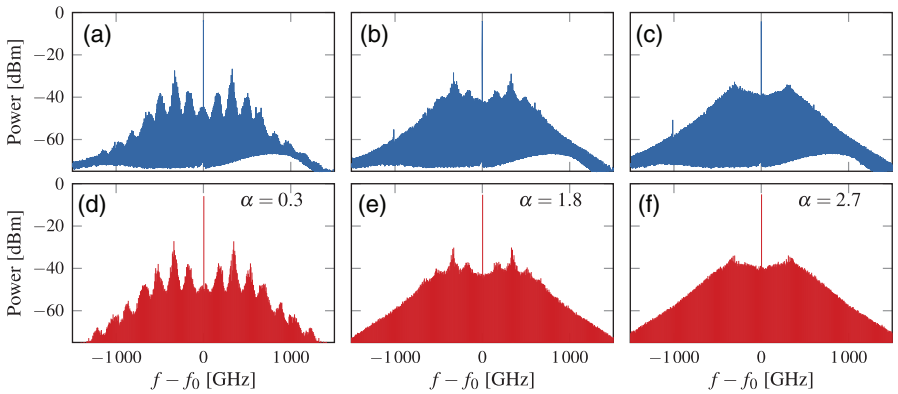

Comparison between (a)–(c) experimental combs generated in a MgF_2 WGMR and (d)–(f) numerical simulations of the Lugiato–Lefever equation [152]. In both cases, the pump power is kept constant ($F^2 = 12$) and the laser wavelength is increased (α is increased). Reprinted from [152] with the permission of AIP Publishing.

combs [175,182]. Since then, new schemes have been proposed to reliably excite normal dispersion dark pulses using parametric seeding [183,184]. A common characteristic of these localized structures is that they can evolve into breathing solutions if the pump power is increased. Indeed, when they become unstable, intra-cavity dark pulse and bright solitons see their peak intensity oscillate [139,185–187]. Bright soliton breathers have recently been experimentally observed and characterized [188].

Finally, at very high pump powers, Kerr frequency combs can exhibit different chaotic regimes where the intensity and phase of each individual optical mode evolves with time in an irregular fashion [152,189]. Contrary to the previous regimes, the beat note frequency detected by a fast photodiode of this chaotic comb produces a noisy microwave frequency whose spectral width far exceeds the natural resonance linewidth. Numerical simulations of such combs have shown that extremely intense and sudden optical pulses can occur in the system. These pulses qualify as rogue waves, and can be explained as a collision of several breathing solitons [190].

It should be noted that the overall dispersion of the resonator tailors the spectral characteristics of the comb [191–197], and can induce various dynamical features such as dispersive wave mode crossing [179,198], among others.

4.2d. Experimental Characterization Of Kerr Combs

The generalized LLE has been shown to accurately describe the generation of Kerr frequency combs in a variety of materials and WGMR shapes, predicting several regimes that were later confirmed in experiments.

The experimental study of Kerr frequency combs in WGMRs is particularly challenging for various reasons. A first one is that the pulse trains repetition rates are often higher than the bandwidth of available electronics. High-Q resonators also have linewidths in the mehahertz range, requiring ultrastable pump lasers. Another important challenge is the control of thermal effects, which might be beneficial or detrimental depending on the relative signs of the thermo-optic and thermo-elastic coefficients:

Figure 18

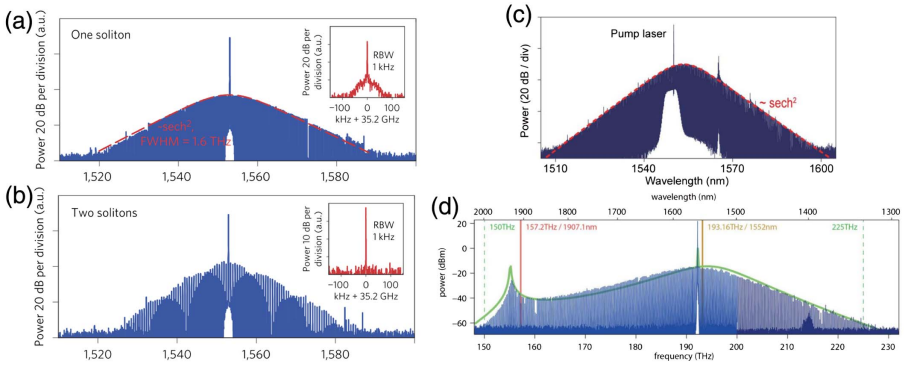

(a) Spectrum corresponding to a single intra-cavity soliton observed in a crystalline MgF_2 resonator and (b) spectrum of two solitons in the same cavity. Reprinted by permission from Macmillan Publishers Ltd.: Herr *et al.*, Nat. Photonics, **8**, 145–152 (2014) [154]. Copyright 2014. (c) Spectrum of a soliton generated in a silica wedge disk resonator. Reprinted with permission from [155]. Copyright 2015 Optical Society of America. (d) Spectrum of a soliton generated in a silicon nitride on-chip resonator. A dispersive wave is visible at the short frequency side, due to the presence of a close-by zero-dispersion wavelength. From Brasch *et al.*, Science, **351**, 357–360 (2016) [156]. Reprinted with permission from AAAS.

for example, it is already well known that thermal instabilities can impede efficient stabilization of the coupled WGM resonator [149,199,200].

Several measurement techniques have therefore been developed to provide the tools needed for better understanding Kerr frequency comb generation. While the optical spectrum of Kerr combs is straightforward to obtain, it is not the case for the phase information. A first method makes two adjacent comb lines interfere using an electro-optic modulator driven by a radio-frequency signal at half the repetition rate [201]. Another method consists of manipulating the phase and amplitude of each comb line separately in a waveshaper in order to obtain a Fourier-limit pulse [164,165]. For that purpose, an optimization routine is used to maximize the autocorrelation trace of the transformed pulse.

The measurement of the comb line position with respect to the WGMR resonances is a critical piece of information, and microwave-photonics techniques have been developed for that purpose. These methods probe the resonances using either another CW laser [165] or an electro-optic modulation of the pump [163]. Instead of measuring the detuning, one can lock the pump wavelength on the pumped resonance, by adapting the Pound–Drever–Hall (PDH) [148,154] and self-injection locking [202] techniques to Kerr combs, or by having a simple feedback on the comb power onto the pump laser [161].

Many applications of Kerr frequency combs require the comb to be stable and coherent from one end to the other. The radio-frequency beat note of the comb gives us hints about the comb's coherence [44,59], and optical heterodyne measurements [122] or spectral pulse shaping [43] can provide more detailed results. Spectral interference techniques usually used in the context of supercontinuum generation have also been adapted to Kerr combs to reveal how the coherence varies across the comb bandwidth [203]. All these methods conclude that the degree of coherence of the comb is highly dependent on the comb regime [203,204], in good agreement with numerical simulations of the LLE [205–207]. It should also be noted that closed-loop pumping [208]

Figure 19

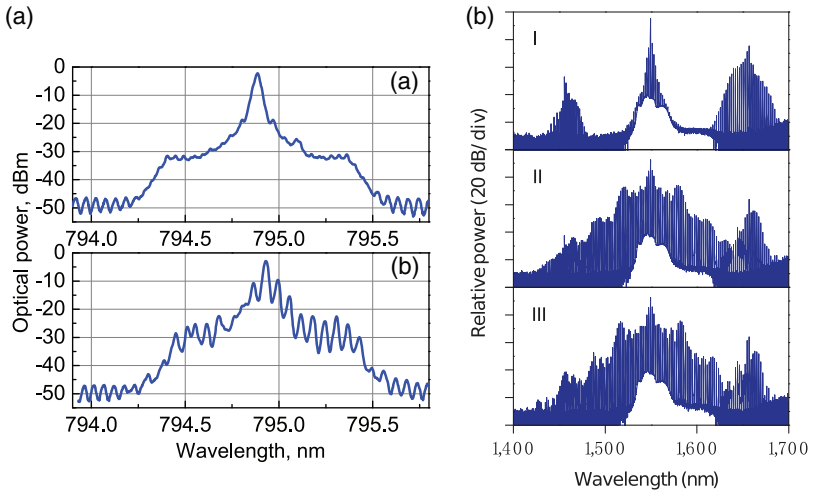

(a) Spectrum corresponding to a dark pulse generated in a crystalline MgF_2 resonator with normal dispersion at 795 nm. Reprinted with permission from [178]. Copyright 2014 Optical Society of America. (b) Generation of various regimes of dark pulses in the normal dispersion regime in a silicon nitride ring resonator. Reprinted by permission from Macmillan Publishers Ltd.: Xue *et al.*, Nat. Photonics, **9**, 594–600 (2015) [180]. Copyright 2015.

or parametric seeding [209,210] can be implemented to excite certain Kerr combs with particular spectral characteristics.

4.2e. Applications of Kerr Frequency Combs

Optical Kerr frequency combs mainly find applications in ultrapure microwave generation, spectroscopy, and coherent optical communications [131,211].

Using Kerr combs for radio-frequency synthesis has been an early technological drive in this area. This trend was motivated by the pioneering works of Theodor Hänsh and John Hall, for which they were awarded the Nobel Prize of Physics in 2005, where they demonstrated the potential of optical frequency combs for high-precision metrology. The microwaves are obtained by direct demodulation of the comb via a fast photodiode, and it can be shown that up to half the power of the incoming optical comb can be converted into a microwave signal [212]. The best phase noise performances achieved so far typically range from −100 to −120 dBc/Hz at 10 kHz from carrier at 5–50 GHz [40,59,202,213–215]. Kerr combs can be stabilized [216,217] and become suitable for high-precision clocks [218] with residual one-second instability of 10^{-15}. Octave spanning combs have already been experimentally demonstrated [111,117,118], and as required by most time-frequency metrology applications, been self-referenced as well [219,220]. It should be noted that WGMRs are also used for metrological applications in the linear regime, where they perform ultranarrow filtering in optoelectronic microwave oscillators [58,60,221–225]. Metrological applications of WGMRs also require them to be isolated from external vibrations [226].

Kerr combs are straightforwardly appealing as coherent multi-wavelength sources for optical fiber communications [204,207,227–230]. Early experiments reported 10 Gbit/s transmissions using an on-off keying modulation scheme [204,227]. Later on, the coherence properties of the comb were used to implement 16-quadrature amplitude modulation (16QAM) and transmit data at 432 Gbit/s using a crystalline resonator [207]. The performance of 1.44 Tbit/s has been achieved using quadrature phase shift keying on a Kerr comb originating from an integrated ring resonator [228]. The use of Kerr solitons has recently permitted an impressive leapfrog improvement toward a 50Tbit/s performance [230].

Spectroscopy also expects to gain multiple benefits from Kerr comb technology. This is due to the fact that these combs can cover various spectral ranges, typically from near- to mid-infrared. The 3–10 μm range is, however, one of the most interesting because it overlaps the spectroscopic signature of several molecules that are particularly relevant in several areas [115,116,122].

Finally, it should be noted that beyond optical frequency comb generation, Kerr-nonlinear WGM resonators are investigated as well for other applications, such as optical isolation, for example [231].

5. STIMULATED RAMAN SCATTERING

Stimulated Raman scattering (SRS) is an inelastic scattering process where photons interact with optical phonons. Unlike the Kerr effect, which results from the optical-field-induced electron-cloud distortion, the mechanism of SRS is attributed to the molecular motion of material. The nonlinear polarization response time to the input electric field is thereby delayed. SRS can be regarded as a third-order nonlinear optical process. It exists in all dielectric materials including crystals with all symmetries and glasses. Early investigation of SRS in WGMRs was carried out in liquid droplets [232]. The use of solid-state ultrahigh-Q WGMRs has further facilitated the investigation of SRS with very low pump power in the CW regime [233,234]. It should be

noted that CW SRS has also been studied in other resonator structures, such as racetrack types [235,236].

Figure 20 illustrates the cavity-enhanced Stokes SRS with WGMRs. The energy level diagram shows that one pump photon can be converted to one Stokes photon with an optical phonon. The energy conservation writes as $\omega_p = \omega_S + \Omega_R$, where p,S designate the pump and Stokes signals and Ω_R is the Raman frequency shift. It should be noted that $\Omega_R/2\pi$ is usually very large (~10 THz), while the bandwidth $\Delta\Omega_R/2\pi$ of the Raman gain can be much narrower in crystals (typically <1 THz). Compared with Kerr frequency comb generation, SRS has no strict phase matching conditions as it is automatically fulfilled. If the Raman gain provided by the pump laser overcomes the cavity mode losses, single- or multi-mode Raman lasing can be realized in WGMRs in both clockwise and counterclockwise directions. In the following, we will review recent SRS results in high-Q WGMRs.

5.1. Stimulated Raman Scattering in WGMRs

Considering the fact that the Raman gain bandwidth usually covers multiple FSRs of WGMRs with diameters above tens of micrometers, the doubly resonant condition for both pump and Stokes fields is usually fulfilled. In their simplest form (and in particular, neglecting frequency detunings from resonance), the SRS process in WGMRs can thereby be modeled by the coupled mode equations:

$$\frac{d\mathcal{E}_p}{dt} = -\frac{1}{2}\Delta\omega_{tot,p}\mathcal{E}_p - \frac{\omega_p}{\omega_R}\frac{g_R v_g}{2A_{eff}}|\mathcal{E}_s|^2\mathcal{E}_R + \sqrt{\Delta\omega_{ext}/T_{FSR}}\sqrt{P_L}, \tag{8}$$

$$\frac{d\mathcal{E}_R}{dt} = -\frac{1}{2}\Delta\omega_{tot,R}\mathcal{E}_R + \frac{g_R v_g}{2A_{eff}}|\mathcal{E}_p|^2\mathcal{E}_R, \tag{9}$$

where the sub-indices p, R indicate the pump and Raman Stokes fields, $A_{eff} = V_{eff}/v_g T_{FSR}$ with $V_{eff} = \int|\mathcal{E}_p|^2 dV \int|\mathcal{E}_R|^2 dV / \int|\mathcal{E}_p|^2|\mathcal{E}_R|^2 dV$ is the effective area for the interaction, g_R is the bulk Raman gain in m/W, P_L is the laser pump power, while $\mathcal{E}_{p,R}$, $\omega_{p,R}$, and $\Delta\omega_{tot,p,R}$ represent the slowly varying amplitudes (with $|\mathcal{E}_{p,R}|^2$ in W), the resonant frequencies, and total resonance linewidths at these frequencies, respectively.

Using high-Q WGMRs as versatile platforms to study Raman lasing can greatly reduce the corresponding threshold pump power. Indeed, the threshold power of Raman lasers can be expressed as [233]

Figure 20

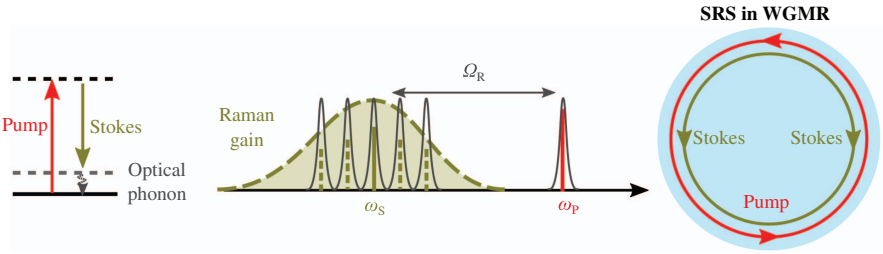

Illustration of resonant SRS in WGMRs. (a) Dashed curve (olive): Raman gain. Gray curves: WGMs. Vertical lines: pump laser (red), Raman Stokes (olive). (b) Energy level diagram with virtual excitation states. (c) SRS in WGMRs showing the nature of bi-directional Raman lasing.

$$P_{\mathrm{th}} = \frac{\pi^2 n^2}{\xi g_{\mathrm{R}}} \frac{V_{\mathrm{eff}}}{Q_{\mathrm{R}} Q_{\mathrm{p}} \lambda_{\mathrm{R}} \lambda_{\mathrm{p}}} \propto \frac{1}{g_{\mathrm{R}}} \frac{V_{\mathrm{eff}}}{Q^2}, \tag{10}$$

where n is the refractive index, ξ is determined by the spatial mode overlap and coupling condition, g_{R} is the bulk Raman gain coefficient, V_{eff} is the effective volume for the interaction, $Q_{\mathrm{p,R}}$ are cavity quality factors for pump and Stokes modes, and $\lambda_{\mathrm{p,R}}$ are the corresponding wavelengths. Interestingly, compared with the threshold power for Kerr comb generation in Eq. (6), the Raman lasing threshold is proportional to the effective volume, and inversely proportional to both the nonlinearity and the square Q-factor.

Deeper understanding of SRS in WGMRs can be gained by using a spatiotemporal formalism, which simultaneously accounts for the interaction between Kerr, Raman, and all-order dispersion effects [237]. This latter aspect is usually very important because the Raman shift Ω_{R} is relatively far away from the pump. This spatiotemporal model explicitly reads

$$\begin{aligned} \frac{\partial \mathcal{E}}{\partial t} = &-\frac{1}{2}\Delta\omega_{\mathrm{tot}}\mathcal{E} + i\sigma\mathcal{E} + iv_{\mathrm{g}} \sum_{k=2}^{K} (i\Omega_{\mathrm{FSR}})^k \frac{\beta_k}{k!} \frac{\partial^k \mathcal{E}}{\partial \theta^k} + \sqrt{\Delta\omega_{\mathrm{ext}}/T_{\mathrm{FSR}}}\sqrt{P_{\mathrm{L}}} \\ &+ iv_{\mathrm{g}}\gamma \left[\mathcal{E}(\theta, t) \int_{-\pi}^{\pi} R(\theta'/\Omega_{\mathrm{FSR}}) |\mathcal{E}(\theta - \theta', t)|^2 \mathrm{d}\theta' \right], \end{aligned} \tag{11}$$

where $R(t) = [1 - f_{\mathrm{R}}]\delta(t) + f_{\mathrm{R}} h_{\mathrm{R}}(t)$ is the impulse response ruling the time-domain behavior of the nonlinear host material. The first term of $R(t)$ stands for the quasi-instantaneous electronic response of the Kerr effect, while the second term accounts for the delayed molecular response of the Raman effect. If we model the Raman gain $g(\Omega)$ as a Lorentzian function of peak value g_{R}, center frequency Ω_{R}, and linewidth $\Delta\Omega_{\mathrm{R}}$, the fractional impulse response can be expressed as

$$h_{\mathrm{R}}(t) = H(t) \frac{\tau_1^2 + \tau_2^2}{\tau_1 \tau_2^2} e^{t/\tau_2} \sin(t/\tau_1), \tag{12}$$

where $\tau_1 = 1/\Omega_{\mathrm{R}}$, $\tau_2 = 2/\Delta\Omega_{\mathrm{R}}$, $H(t)$ is the Heaviside step function, and the fractional coefficient is calculated as

$$f_{\mathrm{R}} = \frac{c}{\pi \omega_{\mathrm{L}} n_2(\omega_{\mathrm{L}})} \int_0^{+\infty} \mathrm{d}t \int_0^{+\infty} \mathrm{d}\Omega g(\Omega) \sin(\Omega t). \tag{13}$$

It is important to note that this model is only valid in the approximation $\Omega_{\mathrm{FSR}} \ll \Omega_{\mathrm{R}}$ [237,238], and that by setting $f_{\mathrm{R}} \equiv 0$, we fold back the Lugiato–Lefever Eq. (7).

To date, Raman lasing has been demonstrated in high-Q WGMRs made of both amorphous and crystalline host materials. Concerning amorphous materials, CO_2 laser machined ultrahigh-Q fused glassy WGMRs have been investigated [35,233,234,239–255]. The first CW Raman laser based on solid-state high-Q WGMR was demonstrated with a fused silica microsphere resonator by Spillane *et al.* in 2002 [233]. Figure 21(a) shows the typical single-mode Raman lasing spectrum in a 40 μm diameter silica microsphere at room temperature. The inset shows a measured CW threshold power as low as 86 μW. Cascaded Raman lasing behavior has also been demonstrated, as shown in Fig. 21(b) where a picture of the fiber taper coupled microsphere is presented [239]. Additionally, the surface coating method has also been applied to study Raman lasers with different materials on the resonator surface [245,256]. For instance, a polydimethylsiloxane-based Raman laser with a large

frequency shift of 2900 cm^{-1} was demonstrated using an on-chip silica host microsphere resonator [256]. Recently, WGMR-based Raman lasers have also been realized with chalcogenide glass (As_2S_3) using a 1550 nm pump laser [244,250]. Compared with silica, this material has a 100 times larger Raman gain coefficient and can extend the spectral window into the mid-IR. It should be noted that anti-Stokes SRS has also been reported in silica WGMRs [246].

Crystalline optical materials can feature a very wide transparent spectral window ranging from the UV to the mid-IR, as well as versatile nonlinear properties. They have also become interesting host materials for investigating SRS in WGMRs. Indeed, Raman lasing was, for instance, reported in WGMRs made of CaF_2 [237,257,258], BaF_2 [238,259], $LiNbO_3$ [260–262], SrF_2 [238], and MgF_2 [237]. Multi-photon and hyper-Raman scattering phenomena have been observed in $LiNbO_3$ [260,261]. Strong forward-backward asymmetry resulting from the polaritonic effect was also investigated in a $LiNbO_3$ resonator [262]. Figures 21(c) and 21(d) presents an ultralow-threshold Raman lasing in a CaF_2 disk resonator [257]. A threshold power as low as 3 μW was observed in a cavity with a Q-factor of 5×10^{10}. Up to eight Raman Stokes were obtained at only 1 mW of the pump power.

Figure 21

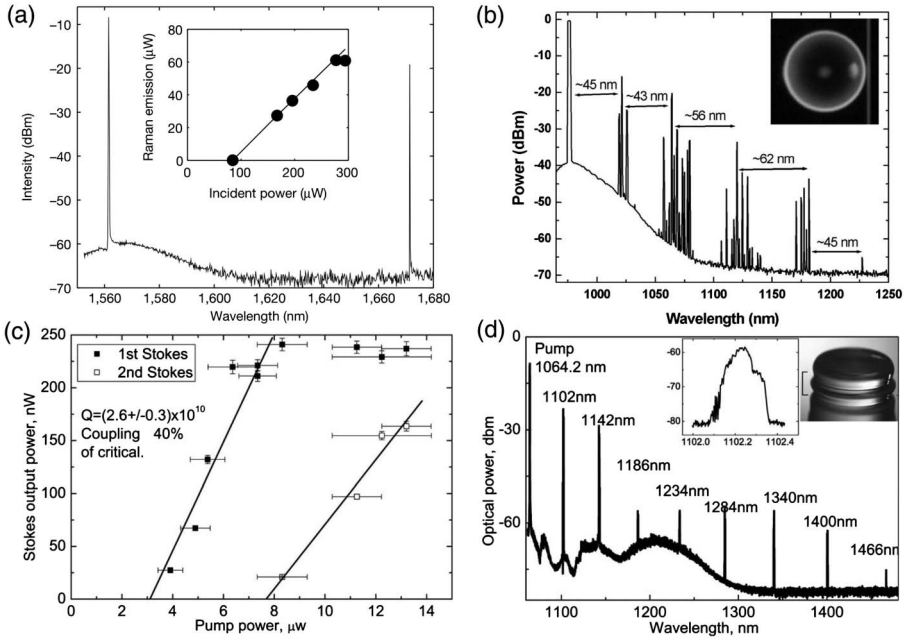

Raman lasing spectra in WGMRs. (a) Single-mode Raman lasing in a silica microsphere with Q of the order of 10^8. Inset: Raman laser power versus pump power. Reprinted by permission from Macmillan Publishers Ltd.: Spillane *et al.*, Nature, **415**, 621–623 (2002) [233]. Copyright 2002. (b) Cascaded Raman lasing spectrum in a silica microsphere. Inset: the picture of the WGMR coupled with a fiber taper. Reprinted with permission from [239]. Copyright 2003 Optical Society of America. (c) Raman laser power versus pump power for first and second Stokes in a CaF_2 WGMR with Q of the order of 10^{10}. (d) Cascaded Raman lasing spectrum in the crystalline resonator. Reprinted with permission from [257]. Copyright 2007 Optical Society of America.

5.2. Phase-Locked Raman Combs

Reported Raman lasers in WGMRs have shown various features, which include single-frequency lasing, multi-mode lasing involving one or multiple transverse mode families, anti-Stokes and multi-Stokes lasing. Among these features, the Kerr effect can be involved simultaneously with SRS and leads to the formation of interesting Kerr-Raman combs, despite that they usually compete with each other [237]. The dynamics of this complex interplay can be investigated using the spatiotemporal model of Eq. (11). Although simultaneous observation of Raman lasing with FWM was previously reported in silica and crystalline WGMRs [233,238], phase locking of Raman combs only occurs in a special regime. It depends on the dispersion profile, coupling condition, and the pump power.

Recently, phase-locked Raman comb generation has been investigated in the normal dispersion regime [258,259]. Figure 22(a) presents the schematic experimental setup and the optical spectrum of the coherent comb obtained in a CaF_2 resonator [258]. The pump laser was self-injection locked to a cavity mode, and the Raman lasing signal was out-coupled through a second prism into a fast photodetector. The resulting RF beat signal featured a linewidth of less than 100 Hz and a low phase noise profile. These phase-locked Raman combs were found with single FSR frequency spacings and without noticeable FWM-mediated sidebands around the pump. Another experiment in a BaF_2 WGMR shows that such phase-locked Raman combs can be generated with multiple FSR frequency spacing [259]. Figure 22(b) presents a Raman comb with triple-FSR frequency spacing. The pump frequency was locked to the mode using the

Figure 22

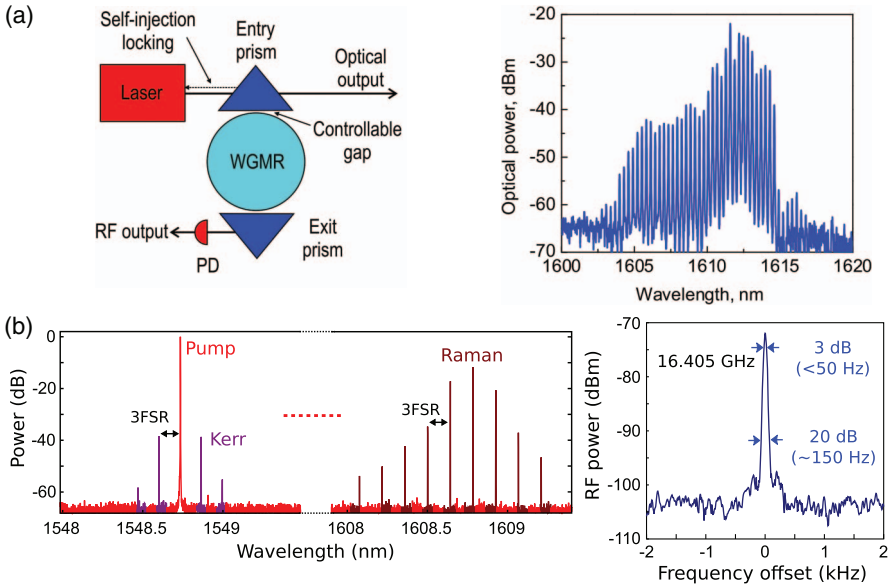

Passively mode-locked Raman comb with single and triple-FSR frequency spacing in crystalline WGMRs. (a) Left: schematic of experimental setup for a dual-prism coupled CaF_2 resonator. Right: optical spectrum of Raman comb with single FSR spacing. Figures 1 and 2 reprinted with permission from Liang *et al.*, Phys. Rev. Lett., **105**, 143903 (2010) [258]. Copyright 2010 by the American Physical Society. (b) Left: 3-FSR spaced Raman comb spectrum covering both pump and Stokes wavelengths. Right: the corresponding RF signal generated with a fast photodiode. Reprinted with permission from [259]. Copyright 2016 Optical Society of America.

PDH locking technique [263]. Also shown in this figure was the corresponding RF beat signal at 16.4 GHz obtained on an electrical spectrum analyzer. Its 3 dB linewidth is less than 50 Hz confirming the phase-locked comb state. Interestingly, a discontinuous step in the detected pump signal was also found, which coincided with the transition from single-frequency lasing to phase-locked Raman comb generation. This behavior is similar to the observed transition in the transmission of pump signal when soliton Kerr comb generation occurs [154].

Another phase-locked Raman comb has been recently demonstrated in on-chip silica wedge resonators, which is referred to as Stokes soliton [264]. These devices are operated in the anomalous dispersion regime at the pump wavelength. Unlike Raman-induced frequency shift in dissipative Kerr solitons [159], Stokes solitons involve two transverse family modes of the WGMR. A soliton Kerr comb is first generated around the pump frequency involving the primary mode family. The induced Raman amplification seeks another mode family that has the same FSR with the primary soliton within its gain bandwidth. The effective potential well generated by the primary soliton is then shared to counteract the dispersion for Stokes waves. Above a threshold of the primary soliton power under good spatial and temporal overlap between two pulse waves, the complex interaction leads to the formation of a Stokes soliton. Both theoretical models and experimental data have been obtained to understand this process [264]. Figure 23(a) provides the measured and simulated cavity FSR versus wavelength for mode families of Stokes solitons in three WGMRs. Also presented is the measured primary soliton FSR as horizontal vertical lines to

Figure 23

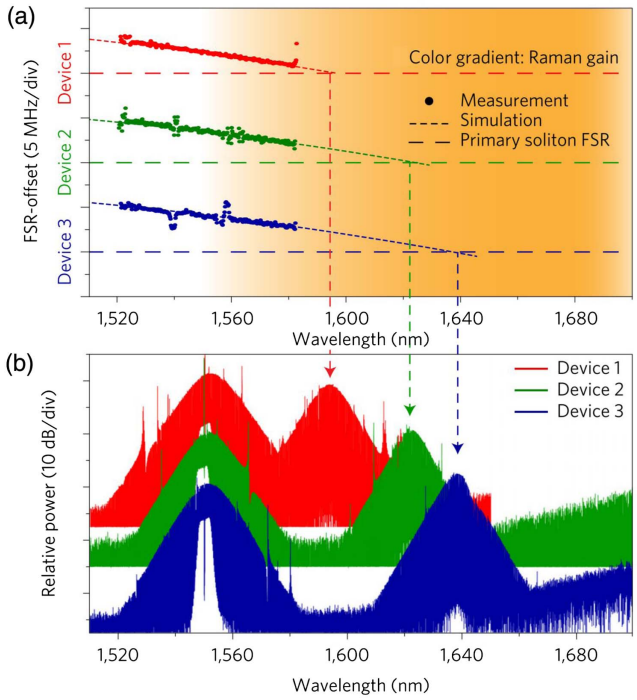

Stokes soliton Raman combs generated in three on-chip silica wedge resonators. (a) Measured and simulated FSR data as a function of wavelength for the Stokes-soliton-forming WGMs. (b) Optical spectra of primary and Stokes solitons. Vertical dashed arrows highlight the agreement with graphical prediction in (a). Reprinted by permission from Macmillan Publishers Ltd.: Yang *et al.*, Nat. Phys. **13**, 53–57 (2016) [264]. Copyright 2016.

predict the location of Stokes solitons. The spectra of Stokes solitons as shown in Fig. 23(b) clearly confirm the prediction.

5.3. Applications

Raman gain is dependent on the pump wavelength and the molecular structure of the host material. It is not limited to the transition between energy levels at specific wavelength windows. By changing the pump wavelength, low-threshold Raman lasers based on WGMRs can be used to produce coherent light waves in new frequencies. Moreover, phase-locked Raman comb generation also shows a path to the applications in the field metrology and microwave photonics. Besides the previously reviewed Raman lasers and combs, SRS in WGMRs has also been used to investigate fundamental questions on gain and loss [249,254]. For instance, Raman gain can be used to adjust the coupling regimes of WGMs without mechanically changing the gap between the resonator and the coupler [254]. It has also been used in studying a non-Hermitian system composed of two coupled microtoroid resonators for its lasing behavior in the vicinity of an exceptional point [249].

Raman lasing in WGMRs for highly sensitive label-free detection of nanoparticles has been demonstrated recently [247,248]. The mechanism is based on the detection of mode splitting caused by the surface nanoparticle scatterers. Raman gain is used to compensate the loss and improve the sensitivity, since the sensitivity limit of WGM sensors is fundamentally determined by the ratio of Q/V [14]. When operating above the threshold, the binding event of nanoparticles on the cavity surface can be detected and counted by monitoring the self-heterodyne beat note frequency shift of Raman laser signals. However, this beat frequency shift depends on both the particle size and its location. Statistical analysis is needed to extract the size of detected nanoparticles, as shown in Fig. 24 [248]. Figure 24(a) shows that large nanoparticles increase the probability of detecting larger beat note frequency change. The ratio of rms of the frequency changes and a threshold (δ/Δ_{th}) as a function of the threshold (Δ_{th}) for NaCl particles with radii of 15, 20, and 25 nm is plotted in Fig. 24(b), showing clear extraction of size information.

Figure 24

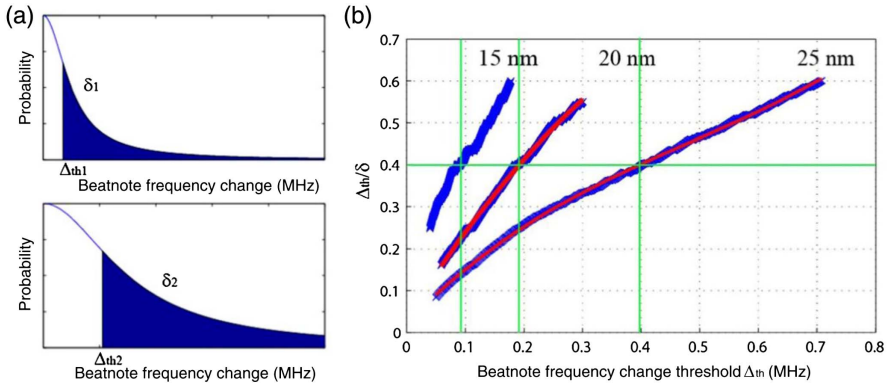

Self-heterodyne detection of nanoparticles using scatterer-induced mode splitting in a silica microtoroid Raman laser. (a) Distribution of beat note frequency changes for small and large nanoparticles (top and bottom). (b) The ratio Δ_{th}/δ versus beat note frequency change threshold Δ_{th} for NaCl particles with radii 15, 20, and 25 nm. Adapted from [248].

6. STIMULATED BRILLOUIN SCATTERING

Similar to stimulated Raman scattering, stimulated Brillouin scattering (SBS) is also an inelastic scattering. Instead of optical phonons, acoustic phonons take part in the interaction with photons. The macroscopic acoustic part of nonlinear polarization response thus makes it a delayed nonlinear optical process, slower than SRS. Until now, strong light confining structures such as fibers and on-chip waveguides have been exploited for investigating SBS [265,266]. In Stokes SBS, the creation of acoustic phonons is induced by the external pump laser via electrostriction. Radiation pressure can also contribute to it in nanoscale devices [267]. The generated traveling density wave acts as a refractive index grating and scatters the pump laser in a preferable direction. In turn, the pump and Doppler-shifted light (Stokes) waves also interfere in a way that strengthens the acoustic field. This stimulated process involving the creation of a Stokes photon and an acoustic photon is illustrated via a three-level energy diagram shown in Fig. 25(a). A reverse process also exists as anti-Stokes.

Resonance-enhanced SBS can further reduce its threshold power. An illustration is shown in Fig. 25(a) where pump and Stokes waves are both resonant. For WGMRs with ultrahigh Q-factors, the CW SBS threshold power at room temperature can be as low as a few microwatts [268]. Depending on the phonon lifetime and its cavity round-trip time, high Q-factor mechanical modes can also be formed in such resonators, especially in microscale sizes. A simplified model for the dynamics of the pump (forward) and Brillouin Stokes (backward) signals $\mathcal{E}_p$ and $\mathcal{E}_B$ can be explicitly written as [54]

$$\frac{d\mathcal{E}_p}{dt} = -\frac{1}{2}\Delta\omega_{tot}\mathcal{E}_p - \frac{g_B v_g}{2A_{eff}}|\mathcal{E}_B|^2\mathcal{E}_p + \sqrt{\Delta\omega_{ext}/T_{FSR}}\sqrt{P_L}, \tag{14}$$

$$\frac{d\mathcal{E}_B}{dt} = -\frac{1}{2}\Delta\omega_{tot}\mathcal{E}_B + \frac{g_B v_g}{2A_{eff}}|\mathcal{E}_p|^2\mathcal{E}_B, \tag{15}$$

where g_B is the bulk Brillouin gain (in m/W). This model is indeed quite analogous to the Raman model presented in Eqs. (8) and (9). The threshold power for SBS can be calculated using [269]

Figure 25

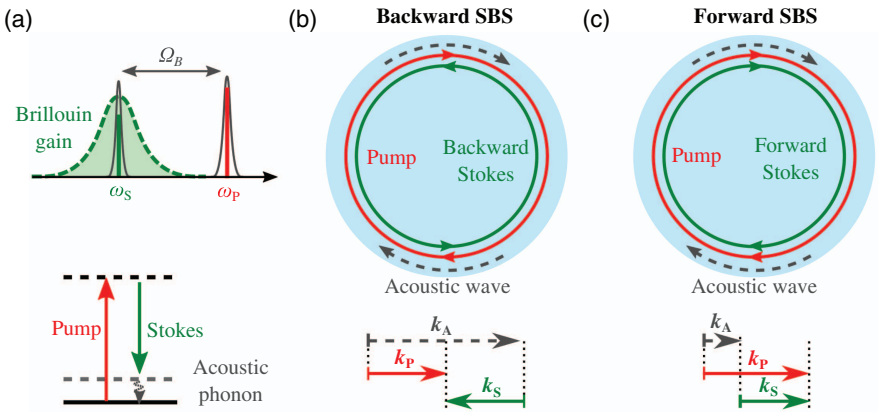

(a) Top: schematic of resonant enhanced SBS, with pump at ω_P (red) and Stokes at ω_S (green) resonant with cavity modes (black Lorentzian lines). Dashed line: Brillouin gain. Bottom: simplified energy diagram. (b),(c) Top: illustration of circulating optical and acoustic waves in WGMRs. Bottom: wave vector conservation law for backward and forward SBS, respectively.

$$P_{\mathrm{th}}^{\mathrm{SBS}} = \frac{\pi^2 n^2 V_{\mathrm{eff}}}{B g_{\mathrm{B}} \lambda_{\mathrm{p}} \lambda_{\mathrm{S}} Q_{\mathrm{p}} Q_{\mathrm{S}}} \frac{1}{1 + Q_{\mathrm{m}} \lambda_{\mathrm{m}} / 2\pi r} \propto \frac{1}{g_{\mathrm{B}}} \frac{V_{\mathrm{eff}}}{Q^2}, \tag{16}$$

where B is the mode overlap, $\lambda_{\mathrm{p,S,m}}$ and $Q_{\mathrm{p,S,m}}$ are the wavelengths and quality factors for the pump, Stokes, and mechanical modes, respectively. For millimeter-size crystalline resonators where the mechanical acoustic resonances are not excited, the second part on the right side of this threshold equation becomes unity. Once again, as in Eq. (6) for the Kerr case and in Eq. (10) for the Raman case, the threshold power is inversely proportional to nonlinearity and scales as V_{eff}/Q^2.

Although SBS is believed to feature the largest gain among all the third-order nonlinear optical processes, its narrow gain bandwidth imposes a challenge in fulfilling the multi-resonant condition in an optical cavity. Nonetheless, high-Q WGMRs can feature rich mode structures (see Subsection 2.1b), thus becoming advantageous in this regard. To date, WGMR-based SBS has been experimentally demonstrated using different host materials and geometries, including glassy microspheres [269–271], wedge-microdisks [39,272,273], microrods [274,275], microbottles and microbubbles [276,277], and crystalline disks [54,238,268,278]. Theoretical investigations of resonant SBS have also been carried out [54,279,280]. Both backward and forward SBS are realized with WGMRs, as illustrated in Figs. 25(b) and 25(c). Also shown in this figure is the corresponding momentum conservation laws (or phase matching condition) $\mathbf{k}_{\mathrm{p}} = \mathbf{k}_{\mathrm{A}} + \mathbf{k}_{\mathrm{S}}$. Together with the energy conservation law $\omega_{\mathrm{p}} = \Omega_{\mathrm{A}} + \Omega_{\mathrm{S}}$, the Brillouin shift Ω_{B} matching the acoustic frequency Ω_{A} can then be determined depending on the pump frequency, the acoustic velocity, and resonance modes. For backward SBS, this value is usually of the order of a few gigahertz for the pump in the infrared. But the magnitude of the Brillouin shift can be much smaller for the forward SBS process [265,266]. Recently, interesting cavity-enhanced Brillouin scattering of photons from magnons has been reported in YIG spherical WGMRs [281–283]. It should be noted that SBS is also extensively investigated using on-chip racetrack resonators [266,284]. In the following, we will summarize WGMR-based SBS and its applications in detail.

6.1. Backward Stimulated Brillouin Scattering

The observation of SBS with high- and ultrahigh-Q WGMRs was first reported in the backward direction in calcium fluoride disk resonators [268] and a silica microsphere [269] in 2009. For backward SBS, the phase matching condition determines the Brillouin shift according to $\Omega_{\mathrm{B}}/2\pi = 2n_{\mathrm{eff}} V_{\mathrm{A}}/\lambda_{\mathrm{p}}$, where n_{eff} and λ_{p} are the effective refractive index and the wavelength of the pump light, and V_{A} is the longitudinal acoustic wave speed. For crystalline materials, V_{A} can be calculated based on the elastic constants and crystal orientations [68].

Figure 26(a) presents the side view of a CaF_2 WGMR with a diameter of 5.5 mm. Its surface was finely polished and was able to support an intrinsic optical Q-factor in the order of 10^{10} for the pump laser at 1064 nm. The WGM field location is highlighted with white brackets. A continuous-wave threshold power around 3 μW was reported [268]. The bottom of Fig. 26(a) shows a typical two-Stokes SBS spectrum in the backward direction, featuring Brillouin shift of 17.5 GHz with a pump at 1064 nm. For crystalline WGMRs, SBS has also been reported in barium fluoride [238,278,285], lithium fluoride [54], and strontium fluoride [238].

For small WGMRs where the lifetime of an acoustic wave is longer than the round-trip time, mechanical modes at the acoustic frequency ω_{A} can be formed in such cavities. The threshold of SBS can be further reduced according to Eq. (16). Figure 26(b) shows the calculated stress and electric field distributions of the typical mechanical

and optical modes for a silica mircosphere resonator with a diameter of 100 μm [269]. Different mechanical modes are experimentally probed via the beat note measurements of Brillouin shift, as shown in Fig. 26(c). The corresponding acoustic mode field distributions are also calculated in this figure.

Traditionally, SBS competes with other nonlinear processes, such as Kerr and Raman effects. Nevertheless, it was shown that four-wave mixing can enhance SBS and lead to a comb-like cascaded SBS with anti-Stokes [238,276,285]. A theoretical investigation was also carried out on cavity-enhanced cascaded SBS with FWM [280]. Recently, the simultaneous interaction of photons with traveling acoustic phonons (Brillouin) and optical phonons (Raman) has been demonstrated with millimeter-size crystalline WGMRs (including BaF_2 and SrF_2). Together with FWM, this "triple" third-order nonlinear effect is referred to as universal nonlinear scattering (UNS) [238]. Figure 27 shows the UNS spectrum obtained from a BaF_2 disk, while in the SrF_2 resonator, the FWM process that couples together Raman and Brillouin Stokes was experimentally observed, as shown in Fig. 28. Comb lines with one FSR spacing of 6.1 GHz were observed around the pump in the forward direction and around both SBS Stokes and anti-Stokes in the backward direction. As these comb lines appeared together only with SRS, they were believed to be FWM results from Raman Stokes with the pump and with SBS Stokes, respectively. This interesting scattering led to the generation of a "triple comb" involving both acoustic and optical phonons. Note that the Raman Stokes at 1619.7 nm corresponding to a Raman shift of 283 cm^{-1} was out of the spectral range of the high-resolution optical spectrum analyzer (OSA) but was observed with another OSA.

Figure 26

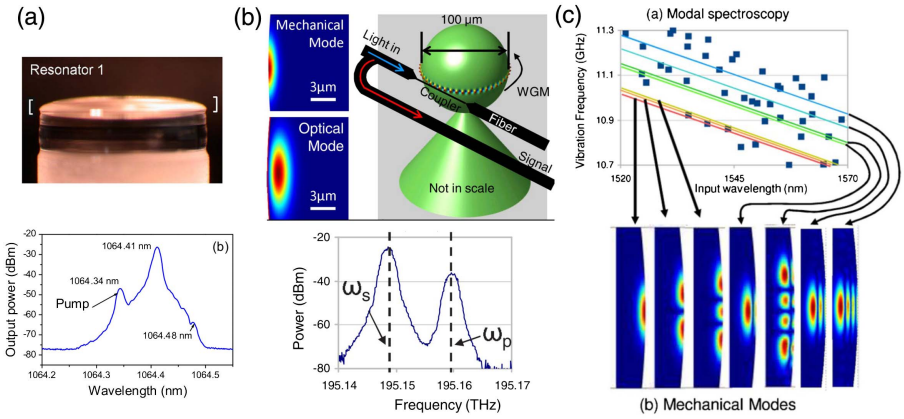

Observation of backward SBS in a CaF_2 disk and a silica microsphere. (a) Top: a side-view picture of CaF_2 disk. Bottom: optical spectrum in the backward direction showing two SBS Stokes. Figures 2 and 4 reprinted with permission from Grudinin *et al.*, Phys. Rev. Lett., **102**, 043902 (2009) [268]. Copyright 2009 by the American Physical Society. (b) Top left: calculated cross field stress and electric field distributions for the mechanical and optical modes in a silica microsphere. Top right: illustrated experimental setup with a fiber taper. Bottom: optical spectrum showing one Brillouin Stokes. (c) Top: experimental observed different SBS shifts in a single resonator. Bottom: corresponding calculated mechanical modes. Figures 1 and 3 reprinted with permission from Tomes and Carmon, Phys. Rev. Lett., **102**, 113601 (200) [269]. Copyright 2009 by the American Physical Society.

6.2. Forward Stimulated Brillouin Scattering

Compared with backward SBS, forward SBS enables the interaction between photons and low-frequency propagating phonons. As shown in Fig. 25(c), the momentum conservation requires that $k_p = k_A + k_S$. Subsequently, it permits the coupling of light waves with low-frequency acoustic waves in the co-propagating direction. Acoustic waves with frequency ranging from tens of megahertz up to 1.4 GHz have been observed with forward SBS in micro-WGMRs [270,277]. Due to the long lifetime of such phonons typically in the tens of microseconds, surface acoustic resonant modes can be formed and leads to a triply resonant condition in WGMRs. The resulting phase matching condition can then be expressed by $m_p = m_S + m_A$, where

Figure 27

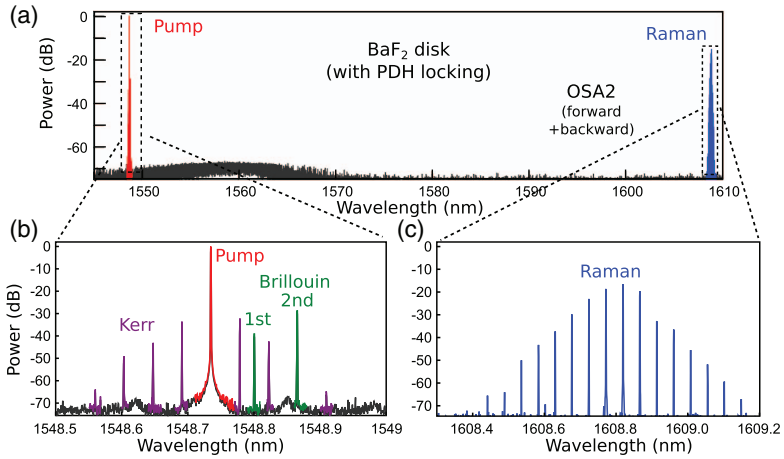

Observation of universal scattering in a BaF_2 disk resonator. Note: a high-resolution (5 MHz) APEX spectrum analyzer was used. Reprinted with permission from [238]. Copyright 2016 Optical Society of America.

Figure 28

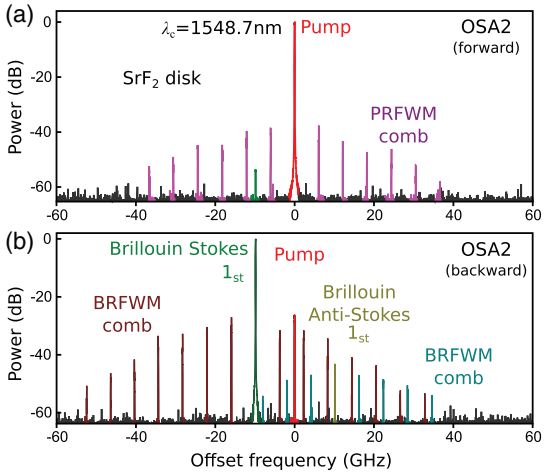

Observation of a "triple comb" generation involving backward SBS, Raman, and FWM in a SrF_2 disk resonator. Note: a high-resolution APEX (5 MHz) spectrum analyzer is used. Reprinted with permission from [238]. Copyright 2016 Optical Society of America.

$m_{p,s,A}$ represent the azimuthal mode numbers of both optical and acoustical modes. For optomechanics with radially breathing acoustic modes, m_A is equal to 0 [37]. Such phase matching conditions put a limit on resonant enhanced SBS. Fortunately, WGMRs can feature rich multi-mode spectra due to high-order modes [286], which can help to fulfill the multi-resonant condition.

Figure 29 shows the beat spectrum of the pump and forward SBS Stokes signals in a fast photodetector. It reveals various excited acoustic modes with different frequencies. The WGMR platform is a silica microsphere with a diameter of 320 μm and Q-factor of 4×10^8 coupled by a fiber taper. The CW threshold power for observing forward SBS is as low as 22.5 μW. With the pump laser frequency slowly scanned from 1520–1570 nm, different low-frequency acoustic modes were detected. Through finite-element simulation, the corresponding stress distribution of mechanical modes at different frequencies were calculated. Forward SBS was also demonstrated in a fused silica resonator with a microfluidic channel that can enable optomechanical investigation with liquids [277]. Recently, ultrasensitive gas detection has been reported using graphene-enhanced Brillouin optomechanical modes in a bottle-shaped capillary WGMR [287]. As we will discuss later, such forward SBS can also be used for applications such as cooling, slow and fast light applications [288–290].

6.3. Applications

6.3a. Spontaneous Brillouin Cooling

Phonons are created in Stokes Brillouin scattering. A reverse process called anti-Stokes scattering is based on the annihilation of already existing phonons.

Figure 29

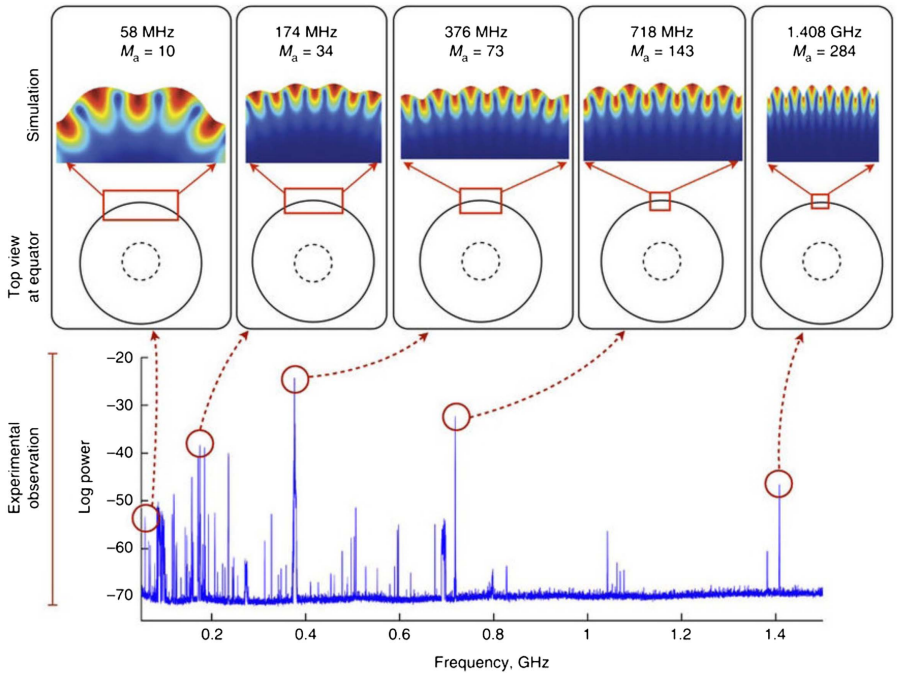

Experimentally observed mechanical modes ranging from 58 MHz–1.4 GHz in forward SBS with the pump swept from 1520–1570 nm. Bottom: the observed acoustic wave frequencies via the beating of the pump and Stokes in a fast detector. Top: the corresponding numerically calculated mechanical modes in a silica microsphere resonator. Reprinted by permission from Macmillan Publishers Ltd.: Bahl *et al.*, Nat. Commun. **2**, 403 (2011) [270]. Copyright 2011.

It is expected that the anti-Stokes process can be useful for cooling applications. In fact, the cooling of mechanical motions has been demonstrated in WGMR-based optomechanical systems [37,291]. In these experiments, the resolved-sideband method is usually implemented for cooling the radial breathing mechanical modes. As previously mentioned, forward Brillouin scattering enables interaction between photons and low-frequency phonons, which have longer lifetimes than gigahertz photons in backward Brillouin processes. It can form high Q-factor traveling mechanical modes in the surface of WGMR. The cooling of such modes was demonstrated by Bahl *et al.* in 2012 [288].

Figure 30 provides the experimental observation of cooling and heating of an acoustic mode around 95 MHz using forward Brillouin scattering in a silica microsphere cavity. Two optical modes with frequency separation matching the acoustic mode frequency (where phase matching also occurs) were confirmed by forward SBS. The lack of phase matching with neighboring modes confined Brillouin scattering among them. When a lower-frequency mode was excited as the pump, cavity-enhanced spontaneous scattering of photons into an anti-Stokes optical mode annihilated the mechanical mode. This process was confirmed with the observation of linewidth broadening with the increased pump power, as shown in Fig. 30(a). Also shown in this figure is the heating process when the higher-frequency mode was chosen as the pump mode instead. Effective acoustic mode temperatures calculated from the linewidth data are also presented in Fig. 30(b). It shows the convergence of both heating and cooling processes at low pump power, giving the acoustic linewidth of 7.7 kHz at room temperature [288].

Figure 30

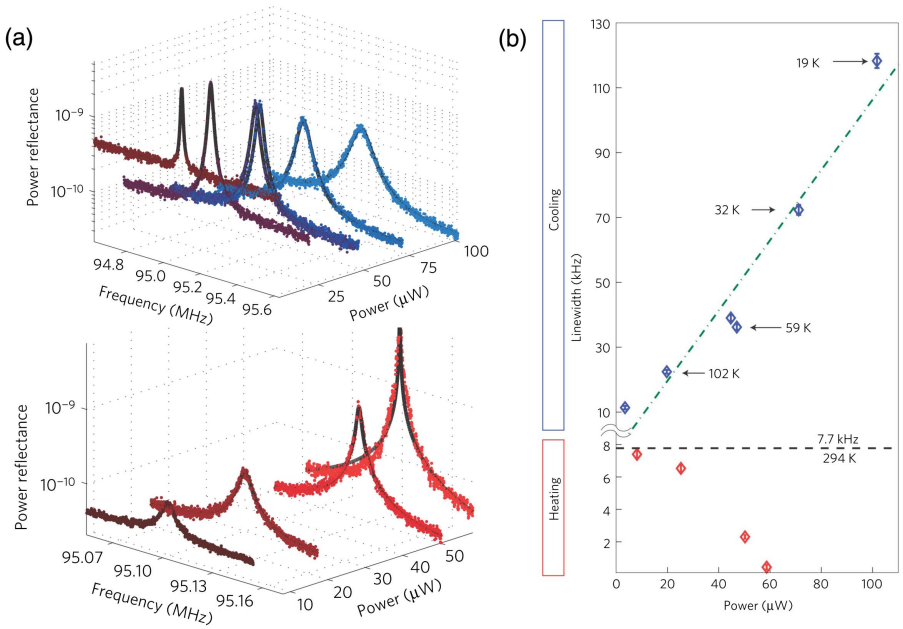

Observation of Brillouin cooling and heating of a 95 MHz acoustic mode in the silica microsphere system. (a) Spectra of power reflectance measured through the beat note as a function of input laser power for the cooling (top) and heating (bottom) experiments. (b) The corresponding calculated effective acoustical mode temperatures. Reprinted by permission from Macmillan Publishers Ltd.: Bahl *et al.*, Nat. Phys. **8**, 203–207 (2012) [288]. Copyright 2012.

6.3b. Low-Noise Microwave Synthesis, Lasers, and Gyroscopes

Due to larger damping rate of acoustic fields when compared with optical fields in backward SBS, a Stokes laser can feature a strongly reduced frequency noise as compared to the pump laser. Combined with ultrahigh Q-factors or long photon storage times in WGMRs, experiments for generating low-phase-noise microwave sources and lasers have been carried out [272,273,275]. In 2013, Li *et al.* succeeded to synthesize low-phase-noise microwave signals using cascaded backward SBS with an on-chip wedge resonator (~6 mm in diameter), as shown in Fig. 31 [272]. The microwave signal was generated by photomixing Stokes laser lines in a fast detector. By choosing the first and third Stokes lines, which share the same optical path, common noises can be greatly suppressed. For a silica WGMR, the generated microwave frequency equals 21.7 GHz, which is twice of the corresponding Brillouin shift. It should be noted that additional closed-loop control is needed to suppress the limited

Figure 31

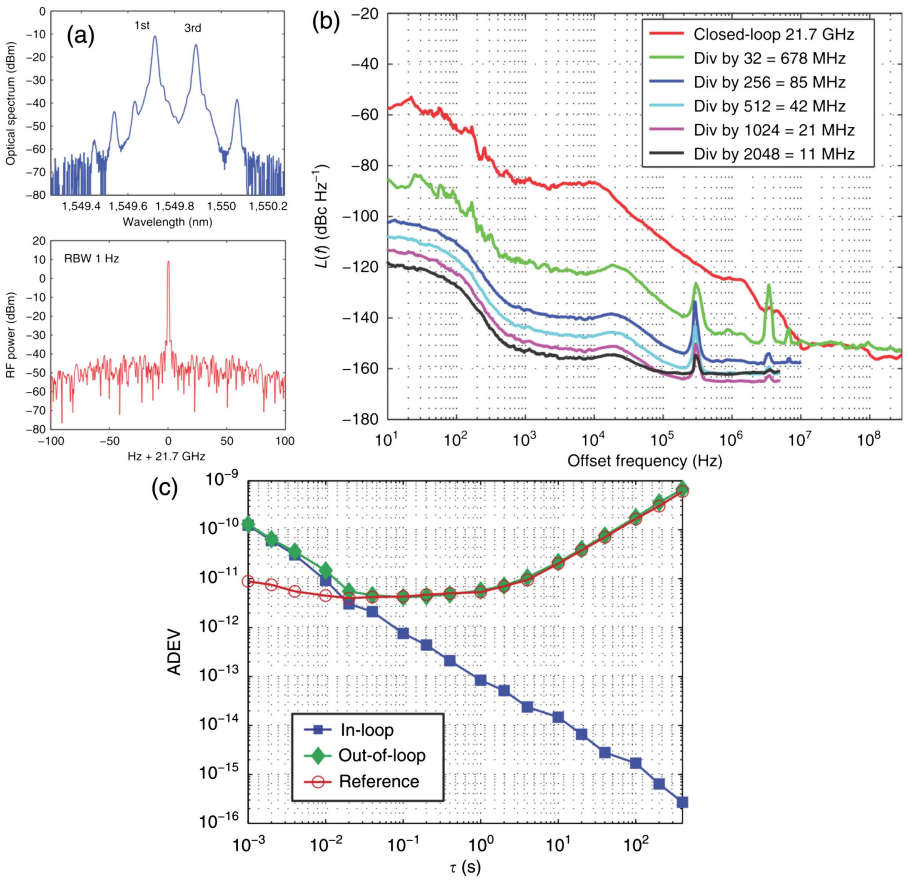

SBS-based microwave synthesizer. (a) Top: optical spectrum of the first and third Brillouin Stokes. Bottom: RF spectrum of a Brillouin microwave source at 21.7 GHz. A reference oscillator at 678 MHz is used for closed-loop phase comparison through frequency division. (b) Phase noise performances of RF frequencies by frequency division from the closed-loop Brillouin microwave oscillator. (c) Allan deviation measurements for the Brillouin oscillator normalized to 21.7 GHz with respect to different low-frequency references. In-loop: the microwave oscillator is phase-locked to an ultralow-noise oven controlled reference oscillator at 400 MHz. Reproduced from [272] under the terms of the Creative Commons Attribution 4.0 License. http://creativecommons.org/licenses/by/4.0/.

phase noise of the microwave synthesizer at low-offset frequency. The synthesizer was thus stabilized to a low-frequency oscillator via frequency division. Figure 31(a) shows the optical spectrum of cascaded SBS (top) and the closed-loop beat note (bottom). The phase noise performance of RF frequencies down to 11 MHz by frequency division based on such a Brillouin microwave oscillator is also shown in Fig. 31(b). Its white phase noise floor can be as low as −160 dBc/Hz. Allan deviation measurements normalized to 21.7 GHz with respect to different reference oscillators are also given in Fig. 31(c). Together with Kerr-comb-based microwave oscillators [202], Brillouin lasing in WGMRs provides a promising way for compact and low-phase-noise microwave generation.

Concerning low-frequency noise laser applications, important research efforts have been made recently using ultrahigh-Q (10^8) silica WGMRs [272,273,275,292]. High coherent Brillouin lasers using millimeter-scale on-chip silica wedge resonators were demonstrated [272,292]. A low-noise dual-cavity laser at 1550 nm with the combination of SBS on a wedge microdisk and a microrod resonator reference for active stabilization was developed, featuring a fractional frequency noise of 7.8×10^{-14} $\mathrm{Hz}^{-1/2}$ at 10 Hz offset [273]. A single microrod resonator-based Brillouin laser with an 240 Hz absolute linewidth and a white-frequency noise floor of 0.1 $\mathrm{Hz}^2\,\mathrm{Hz}^{-1}$ was reported [275]. In these experiments, thermal noises from the pump laser via thermo-optic and thermal expansion effects limited the performance of Brillouin lasers at low offset frequency. Besides using larger-scale resonators, active stabilization including relative intensity noise reduction was generally used [275].

WGM resonators can also be useful for compact optical gyroscopes, using counter-propagating (clockwise and counterclockwise) intra-cavity fields to measure rotation via Sagnac-induced frequency shifts. Recent research developments have shown that both Brillouin scattering [293] and Rayleigh backscattering [294] can be used to achieve remarkably high levels of stability.

Figure 32

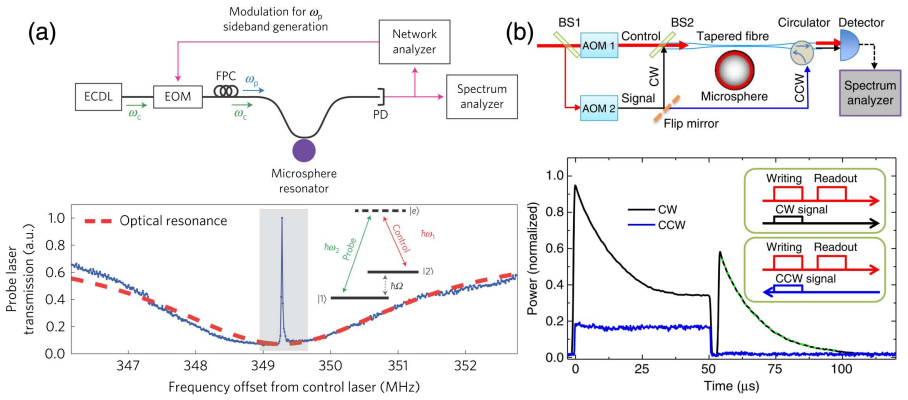

(a) Experimentally observed BSIT scattering induced transparency in a silica microsphere. Top: experimental setup. Bottom: spectrum with an analog of EIT's three-level lambda system in the inset. Reprinted by permission from Macmillan Publishers Ltd.: Kim *et al.*, Nat. Phys. **11**, 275–280 (2015) [290]. Copyright 2015. (b) Nonreciprocal light storage based on BSIT. Top: experimental setup. Bottom: measured intra-cavity signal power during the writing and readout processes. Inset: the pulses sequences with control signal in red and CW/CCW probe signal in black/blue. Reproduced from [289] under the terms of the Creative Commons Attribution 4.0 License. http://creativecommons.org/licenses/by/4.0/.

6.3c. Brillouin Scattering Induced Transparency

A recent application of SBS with high-Q WGMRs lies in the field of nonreciprocal Brillouin scattering induced transparency (BSIT), as demonstrated in 2015 by Kim *et al.* [290] and Dong *et al.* [289]. In WGMRs, optomechanically induced transparency, analogous to electromagnetically induced transparency (EIT), was reported in 2010 in a silica microtoroid oscillator by Weis *et al.* [295]. In such systems, the standing vibration mode features a longer lifetime than the optical mode and meets the requirement of a long-lived nonradiation coherence. In comparison, traveling acoustic modes in forward SBS also feature a long lifetime. Nonetheless, the conversion laws of energy and momentum in WGMRs for forward SBS require the use of two optical modes instead of one optical mode for BSIT.

Figure 32(a) shows the reported BSIT in a 150 μm diameter silica microsphere [290]. The experimental setup mainly consisted of a tunable control laser, a tunable probe laser by phase modulating the control laser, and the fiber taper coupled microsphere resonator. BSIT can be described by the three-level scheme shown in the inset. Two optical modes that satisfy the requirement of forward SBS were first located. A strong control laser was then used to excite the low-frequency optical mode representing the $|2\rangle \rightarrow |e\rangle$ transition. The weak probe laser detuned around the high-frequency optical mode probed the $|1\rangle \rightarrow |e\rangle$ transition. Due to the forward SBS process, the anti-Stokes signal interfered destructively with the probe laser and resulted in a sharp transparency window in the transmission spectrum of the probe optical mode, as shown in Fig. 32 (bottom). Both BSIT and Brillouin scattering induced opacity (slow and fast light) were demonstrated [290]. Meanwhile, the BSIT and subsequent nonreciprocal light storage were also reported in a silica microsphere resonator [289], as shown in Fig. 32, where two acousto-optic modulators were used to produce the control and signal sources with frequency separation matching the acoustic mode frequency ω_A. The mechanism of light storage lies in the transfer of signal pulse to the acoustic waves in BSIT. Similar to an optomechanical WGMR [296], the storage time is thereby determined by the lifetime of the acoustic wave. Nonreciprocity resulting from phase matching requirement was also verified.

7. CONCLUSION

In this paper, we have presented a broad overview of the latest advances in the area of nonlinear phenomena in WGM resonators with high and ultrahigh Q-factors.

We have first briefly introduced the concept of WGMRs, with an emphasis on their eigenmode and eigenspectrum properties, as well as their performances in terms of Q-factor. The second section focused on second-order nonlinearities like second-harmonic generation, optical parametric oscillations, and sum-frequency generation. Then, in the third section, we reviewed Kerr effects such as third-harmonic generation and Kerr optical frequency combs. Stimulated Raman and Brillouin scattering were then discussed in the two subsequent sections, respectively.

The topic of nonlinear phenomena in WGMRs high-Q still experiences a very fast growth, as indicated by the increasing number of published articles every year, and by the wide scope of the corresponding research. The general consensus is that the challenges to be met are of both fundamental and technological nature.

On the fundamental side, the quest for a better understanding of light–matter interactions is by essence an always on-going process. Since WGMRs offer an ideal platform to understand how long-lifetime and confined photons interact with matter, research along that line is expected to unveil unexpected phenomena. In the semiclassical realm, light–matter interactions are ruled by nonlinear partial differential equations with properties that are mathematically not completely understood.

The very high level of control achieved in recent years for these nonlinear processes allows us to design experiments where these interactions could be monitored at the few- or even single-photon level, paving the way for compact quantum photonic systems at room temperature.

From the technological side, the main challenge is twofold: leapfrog performance improvement comparatively to existing technologies, and scalability for mass production. Indeed, WGMRs have already demonstrated outstanding achievements in several areas ranging from telecommunications to sensing, but a very important last step is to achieve compatibility with industrial norms and constraints in terms of energy consumption, robustness, and interoperability with surrounding systems.

Research on the topic of nonlinear WGMRs is genuinely cross-disciplinary, and benefits from the contribution of scientists coming from a wide variety of different backgrounds. It can be expected that this shared interest will ensure many more fruitful scientific outcomes for WGMR research in the years to come.

FUNDING

H2020 European Research Council (ERC) (278616, 632108); Centre National d'Etudes Spatiales (CNES) (SHYRO); Agence Nationale de la Recherche (ANR); Labex ACTION (ANR-11-LABX-01-01); National Natural Science Foundation of China (NSFC) (61605051).

ACKNOWLEDGMENT

The authors would like to thank the Labex ACTION for financial and logistical support. G. L. would like to acknowledge the support from the NSFC. Y. K. C. would also like to acknowledge funding from the ERC through the projects NextPhase and Versyt and from the CNES through the project SHYRO.

REFERENCES

1. Lord Rayleigh, *The Theory of Sound* (Macmillan, 1896), Vol. **2**.
2. Lord Rayleigh, "The problem of the whispering gallery," Philos. Mag. **520**(120), 1001–1004 (1910).
3. Lord Rayleigh, "Further applications of Bessel's functions of high order to the whispering gallery and allied problems," Philos. Mag. **27**(157), 100–109 (1914).
4. C. Raman and G. Sutherland, "Whispering-gallery phenomena at St. Paul's Cathedral," Nature **108**, 42 (1921).
5. G. Mie, "Beiträge zur Optik trüber Medien, speziell kolloidaler Metallösungen," Ann. Phys. **330**, 377–445 (1908).
6. P. Debye, "Der lichtdruck auf kugeln von beliebigem material," Ann. Phys. **335**, 57–136 (1909).
7. A. N. Oraevsky, "Whispering-gallery waves," Quantum Electron. **32**, 377–400 (2002).
8. A. B. Matsko and V. S. Ilchenko, "Optical resonators with whispering gallery modes I: Basics," IEEE J. Sel. Top. Quantum Electron. **12**, 3–14 (2006).
9. V. Braginsky, M. Gorodetsky, and V. Ilchenko, "Quality-factor and nonlinear properties of optical whispering-gallery modes," Phys. Lett. A **137**, 393–397 (1989).
10. K. J. Vahala, "Optical microcavities," Nature **424**, 839–846 (2003).
11. A. Matsko, A. Savchenkov, D. Strekalov, V. Ilchenko, and L. Maleki, "Review of applications of whispering-gallery mode resonators in photonics and nonlinear optics," IPN Prog. Rep. **42**, 1–51 (2005).

12. V. S. Ilchenko and A. B. Matsko, "Optical resonators with whispering-gallery modes-part II: applications," IEEE J. Sel. Top. Quantum Electron. **12**, 15–32 (2006).
13. A. Chiasera, Y. Dumeige, P. Feron, M. Ferrari, Y. Jestin, G. Nunzi Conti, S. Pelli, S. Soria, and G. C. Righini, "Spherical whispering-gallery-mode microresonators," Laser Photon. Rev. **4**, 457–482 (2010).
14. M. R. Foreman, J. D. Swaim, and F. Vollmer, "Whispering gallery mode sensors," Adv. Opt. Photon. **7**, 168–240 (2015).
15. D. V. Strekalov, C. Marquardt, A. B. Matsko, H. G. Schwefel, and G. Leuchs, "Nonlinear and quantum optics with whispering gallery resonators," J. Opt. **18**, 123002 (2016).
16. T. Reynolds, N. Riesen, A. Meldrum, X. Fan, J. M. Hall, T. M. Monro, and A. François, "Fluorescent and lasing whispering gallery mode microresonators for sensing applications," Laser Photon. Rev. **11**, 1600265 (2017).
17. Y. Dumeige, S. Trebaol, L. Ghişa, T. K. N. Nguyen, H. Tavernier, and P. Féron, "Determination of coupling regime of high-Q resonators and optical gain of highly selective amplifiers," J. Opt. Soc. Am. B **25**, 2073–2080 (2008).
18. C. Lam, P. T. Leung, and K. Young, "Explicit asymptotic formulas for the positions, widths, and strengths of resonances in Mie scattering," J. Opt. Soc. Am. B **9**, 1585–1592 (1992).
19. S. Schiller, "Asymptotic expansion of morphological resonance frequencies in Mie scattering," Appl. Opt. **32**, 2181–2185 (1993).
20. B. Johnson, "Theory of morphology-dependent resonances: shape resonances and width formulas," J. Opt. Soc. Am. A **10**, 343–352 (1993).
21. L. Collot, V. Lefevre-Seguin, M. Brune, J. Raimond, and S. Haroche, "Very high-Q whispering-gallery mode resonances observed on fused silica microspheres," Europhys. Lett. **23**, 327–334 (1993).
22. M. L. Gorodetsky, A. A. Savchenkov, and V. S. Ilchenko, "Ultimate Q of optical microsphere resonators," Opt. Lett. **21**, 453–455 (1996).
23. V. Huet, A. Rasoloniaina, P. Guillemé, P. Rochard, P. Féron, M. Mortier, A. Levenson, K. Bencheikh, A. Yacomotti, and Y. Dumeige, "Millisecond photon lifetime in a slow-light microcavity," Phys. Rev. Lett. **116**, 133902 (2016).
24. M. Sumetsky, Y. Dulashko, and R. Windeler, "Optical microbubble resonator," Opt. Lett. **35**, 898–900 (2010).
25. S. Berneschi, D. Farnesi, F. Cosi, G. N. Conti, S. Pelli, G. Righini, and S. Soria, "High Q silica microbubble resonators fabricated by arc discharge," Opt. Lett. **36**, 3521–3523 (2011).
26. A. Watkins, J. Ward, Y. Wu, and S. N. Chormaic, "Single-input spherical microbubble resonator," Opt. Lett. **36**, 2113–2115 (2011).
27. N. Riesen, W. Q. Zhang, and T. M. Monro, "Dispersion in silica microbubble resonators," Opt. Lett. **41**, 1257–1260 (2016).
28. T. Ioppolo and M. V. Ötügen, "Pressure tuning of whispering gallery mode resonators," J. Opt. Soc. Am. B **24**, 2721–2726 (2007).
29. R. Henze, T. Seifert, J. Ward, and O. Benson, "Tuning whispering gallery modes using internal aerostatic pressure," Opt. Lett. **36**, 4536–4538 (2011).
30. Q. Lu, J. Liao, S. Liu, X. Wu, L. Liu, and L. Xu, "Precise measurement of micro bubble resonator thickness by internal aerostatic pressure sensing," Opt. Express **24**, 20855–20861 (2016).
31. D. Huang, W. Huang, J. Zeng, M. Deng, L. Shi, and T. Zhu, "Electrical thermo-optic tuning of whispering gallery mode microtube resonator," IEEE Photon. Technol. Lett. **29**, 169–172 (2017).
32. D. W. Vogt and R. Leonhardt, "Terahertz whispering gallery mode bubble resonator," Optica **4**, 809–812 (2017).

33. D. K. Armani, T. J. Kippenberg, S. M. Spillane, and K. J. Vahala, "Ultra-high-Q toroid microcavity on a chip," Nature **421**, 925–928 (2003).
34. T. J. Kippenberg, S. M. Spillane, and K. J. Vahala, "Kerr-nonlinearity optical parametric oscillation in an ultrahigh-Q toroid microcavity," Phys. Rev. Lett. **93**, 083904 (2004).
35. T. J. Kippenberg, S. M. Spillane, D. K. Armani, and K. J. Vahala, "Ultralow-threshold microcavity Raman laser on a microelectronic chip," Opt. Lett. **29**, 1224–1226 (2004).
36. P. Del'Haye, A. Schliesser, O. Arcizet, T. Wilken, R. Holzwarth, and T. J. Kippenberg, "Optical frequency comb generation from a monolithic microresonator," Nature **450**, 1214–1217 (2007).
37. M. Aspelmeyer, T. J. Kippenberg, and F. Marquardt, "Cavity optomechanics," Rev. Mod. Phys. **86**, 1391–1452 (2014).
38. T. Kippenberg, S. Spillane, D. Armani, and K. Vahala, "Fabrication and coupling to planar high-Q silica disk microcavities," Appl. Phys. Lett. **83**, 797–799 (2003).
39. H. Lee, T. Chen, J. Li, K. Y. Yang, S. Jeon, O. Painter, and K. J. Vahala, "Chemically etched ultrahigh-Q wedge-resonator on a silicon chip," Nat. Photonics **6**, 369–373 (2012).
40. J. Li, H. Lee, T. Chen, and K. J. Vahala, "Low-pump-power, low-phase-noise, and microwave to millimeter-wave repetition rate operation in microcombs," Phys. Rev. Lett. **109**, 233901 (2012).
41. A. R. Johnson, Y. Okawachi, J. S. Levy, J. Cardenas, K. Saha, M. Lipson, and A. L. Gaeta, "Chip-based frequency combs with sub-100 GHz repetition rates," Opt. Lett. **37**, 875–877 (2012).
42. J. S. Levy, A. Gondarenko, M. A. Foster, A. C. Turner-Foster, A. L. Gaeta, and M. Lipson, "CMOS-compatible multiple-wavelength oscillator for on-chip optical interconnects," Nat. Photonics **4**, 37–40 (2010).
43. F. Ferdous, H. Miao, D. E. Leaird, K. Srinivasan, J. Wang, L. Chen, L. T. Varghese, and A. M. Weiner, "Spectral line-by-line pulse shaping of on-chip microresonator frequency combs," Nat. Photonics **5**, 770–776 (2011).
44. T. Herr, K. Hartinger, J. Riemensberger, C. Y. Wang, E. Gavartin, R. Holzwarth, M. L. Gorodetsky, and T. J. Kippenberg, "Universal formation dynamics and noise of Kerr-frequency combs in microresonators," Nat. Photonics **6**, 480–487 (2012).
45. D. J. Moss, R. Morandotti, A. L. Gaeta, and M. Lipson, "New CMOS-compatible platforms based on silicon nitride and Hydex for nonlinear optics," Nat. Photonics **7**, 597–607 (2013).
46. A. Coillet, R. Henriet, K. P. Huy, M. Jacquot, L. Furfaro, I. Balakireva, L. Larger, and Y. K. Chembo, "Microwave photonics systems based on whispering-gallery-mode resonators," J. Vis. Exp. **78**, e50423 (2013).
47. S. B. Papp, P. Del'Haye, and S. A. Diddams, "Mechanical control of a microrod-resonator optical frequency comb," Phys. Rev. X **3**, 031003 (2013).
48. A. A. Savchenkov, A. B. Matsko, V. S. Ilchenko, and L. Maleki, "Optical resonators with ten million finesse," Opt. Express **15**, 6768–6773 (2007).
49. A. A. Savchenkov, A. B. Matsko, D. Strekalov, M. Mohageg, V. S. Ilchenko, and L. Maleki, "Low threshold optical oscillations in a whispering gallery mode CaF_2 resonator," Phys. Rev. Lett. **93**, 243905 (2004).
50. I. S. Grudinin, N. Yu, and L. Maleki, "Generation of optical frequency combs with a CaF_2 resonator," Opt. Lett. **34**, 878–880 (2009).
51. H. Tavernier, P. Salzenstein, K. Volyanskiy, Y. K. Chembo, and L. Larger, "Magnesium fluoride whispering gallery mode disk-resonators for microwave photonics applications," IEEE Photon. Technol. Lett. **22**, 1629–1631 (2010).

52. G. Lin, S. Diallo, R. Henriet, M. Jacquot, and Y. K. Chembo, "Barium fluoride whispering-gallery-mode disk-resonator with one billion quality-factor," Opt. Lett. **39**, 6009–6012 (2014).
53. R. Henriet, A. Coillet, K. Saleh, L. Larger, and Y. K. Chembo, "Barium fluoride and lithium fluoride whispering-gallery-mode resonators for photonics applications," Opt. Eng. **53**, 071821 (2014).
54. S. Diallo, G. Lin, R. Martinenghi, L. Furfaro, M. Jacquot, and Y. K. Chembo, "Brillouin lasing in ultra-high-Q lithium fluoride disk resonators," IEEE Photon. Technol. Lett. **28**, 955–958 (2016).
55. R. Henriet, G. Lin, A. Coillet, M. Jacquot, L. Furfaro, L. Larger, and Y. K. Chembo, "Kerr optical frequency comb generation in strontium fluoride whispering-gallery mode resonators with billion quality factor," Opt. Lett. **40**, 1567–1570 (2015).
56. V. S. Ilchenko, A. A. Savchenkov, A. B. Matsko, and L. Maleki, "Nonlinear optics and crystalline whispering gallery mode cavities," Phys. Rev. Lett. **92**, 043903 (2004).
57. Y. Pan, G. Lin, S. Diallo, X. Zhang, and Y. K. Chembo, "Design of X-cut and Z-cut lithium niobate whispering-gallery-mode disk-resonators with high quality factors," IEEE Photon. J. **9**, 2700608 (2017).
58. K. Volyanskiy, P. Salzenstein, H. Tavernier, M. Pogurmirskiy, Y. K. Chembo, and L. Larger, "Compact optoelectronic microwave oscillators using ultra-high Q whispering gallery mode disk-resonators and phase modulation," Opt. Express **18**, 22358–22363 (2010).
59. S. B. Papp and S. A. Diddams, "Spectral and temporal characterization of a fused-quartz-microresonator optical frequency comb," Phys. Rev. A **84**, 053833 (2011).
60. L. Maleki, "Sources: the optoelectronic oscillator," Nat. Photonics **5**, 728–730 (2011).
61. G. Kozyreff, J. L. Dominguez-Juarez, and J. Martorell, "Nonlinear optics in spheres: from second harmonic scattering to quasi-phase matched generation in whispering gallery modes," Laser Photon. Rev. **5**, 737–749 (2011).
62. I. Breunig, "Three-wave mixing in whispering gallery resonators," Laser Photon. Rev. **10**, 569–587 (2016).
63. F. Leo, T. Hansson, I. Ricciardi, M. De Rosa, S. Coen, S. Wabnitz, and M. Erkintalo, "Walk-off-induced modulation instability, temporal pattern formation, and frequency comb generation in cavity-enhanced second-harmonic generation," Phys. Rev. Lett. **116**, 033901 (2016).
64. X. Guo, C.-L. Zou, H. Jung, and H. X. Tang, "On-chip strong coupling and efficient frequency conversion between telecom and visible optical modes," Phys. Rev. Lett. **117**, 123902 (2016).
65. J. Moore, M. Tomes, T. Carmon, and M. Jarrahi, "Continuous-wave ultraviolet emission through fourth-harmonic generation in a whispering-gallery resonator," Opt. Express **19**, 24139–24146 (2011).
66. J. Dominguez-Juarez, G. Kozyreff, and J. Martorell, "Whispering gallery microresonators for second harmonic light generation from a low number of small molecules," Nat. Commun. **2**, 254 (2011).
67. D. V. Strekalov, A. S. Kowligy, V. G. Velev, G. S. Kanter, P. Kumar, and Y.-P. Huang, "Phase matching for the optical frequency conversion processes in whispering gallery mode resonators," J. Mod. Opt. **63**, 50–63 (2015).
68. R. W. Boyd, *Nonlinear Optics*, 3rd ed. (Academic, 2008).
69. J. U. Fürst, D. V. Strekalov, D. Elser, M. Lassen, U. L. Andersen, C. Marquardt, and G. Leuchs, "Naturally phase-matched second-harmonic generation in a whispering-gallery-mode resonator," Phys. Rev. Lett. **104**, 153901 (2010).

70. J. U. Fürst, K. Buse, I. Breunig, P. Becker, J. Liebertz, and L. Bohatý, "Second-harmonic generation of light at 245 nm in a lithium tetraborate whispering gallery resonator," Opt. Lett. **40**, 1932–1935 (2015).
71. G. Lin, J. U. Fürst, D. V. Strekalov, and N. Yu, "Wide-range cyclic phase matching and second harmonic generation in whispering gallery resonators," Appl. Phys. Lett. **103**, 181107 (2013).
72. J. Lin, Y. Xu, J. Ni, M. Wang, Z. Fang, L. Qiao, W. Fang, and Y. Cheng, "Phase-matched second-harmonic generation in an on-chip $LiNbO_3$ microresonator," Phys. Rev. Appl. **6**, 014002 (2016).
73. P. S. Kuo, J. Bravo-Abad, and G. S. Solomon, "Second-harmonic generation using -quasi-phasematching in a GaAs whispering-gallery-mode microcavity," Nat. Commun. **5**, 3109 (2014).
74. S. Mariani, A. Andronico, A. Lemaître, I. Favero, S. Ducci, and G. Leo, "Second-harmonic generation in AlGaAs microdisks in the telecom range," Opt. Lett. **39**, 3062–3065 (2014).
75. D. P. Lake, M. Mitchell, H. Jayakumar, L. F. dos Santos, D. Curic, and P. E. Barclay, "Efficient telecom to visible wavelength conversion in doubly resonant gallium phosphide microdisks," Appl. Phys. Lett. **108**, 031109 (2016).
76. C. Wang, M. J. Burek, Z. Lin, H. A. Atikian, V. Venkataraman, I.-C. Huang, P. Stark, and M. Lončar, "Integrated high quality factor lithium niobate microdisk resonators," Opt. Express **22**, 30924–30933 (2014).
77. N. Vukovic, N. Healy, J. R. Sparks, J. V. Badding, P. Horak, and A. C. Peacock, "Tunable continuous wave emission via phase-matched second harmonic generation in a ZnSe microcylindrical resonator," Sci. Rep. **5**, 11798 (2015).
78. I. Roland, M. Gromovyi, Y. Zeng, M. El Kurdi, S. Sauvage, C. Brimont, T. Guillet, B. Gayral, F. Semond, J. Y. Duboz, and M. de Micheli, "Phase-matched second harmonic generation with on-chip GaN-on-Si microdisks," Sci. Rep. **6**, 34191 (2016).
79. V. S. Ilchenko, A. B. Matsko, A. A. Savchenkov, and L. Maleki, "Low-threshold parametric nonlinear optics with quasi-phase-matched whispering-gallery modes," J. Opt. Soc. Am. B **20**, 1304–1308 (2003).
80. D. Haertle, "Domain patterns for quasi-phase matching in whispering-gallery modes," J. Opt. **12**, 035202 (2010).
81. K. Sasagawa and M. Tsuchiya, "Highly efficient third harmonic generation in a periodically poled MgO:$LiNbO_3$ disk resonator," Appl. Phys. Express **2**, 122401 (2009).
82. G. Lin, J. U. Fürst, D. V. Strekalov, I. S. Grudinin, and N. Yu, "High-Q UV whispering gallery mode resonators made of angle-cut BBO crystals," Opt. Express **20**, 21372–21378 (2012).
83. C. Xiong, W. Pernice, K. K. Ryu, C. Schuck, K. Y. Fong, T. Palacios, and H. X. Tang, "Integrated GaN photonic circuits on silicon (100) for second harmonic generation," Opt. Express **19**, 10462–10470 (2011).
84. J. S. Levy, M. A. Foster, A. L. Gaeta, and M. Lipson, "Harmonic generation in silicon nitride ring resonators," Opt. Express **19**, 11415–11421 (2011).
85. W. H. P. Pernice, C. Xiong, C. Schuck, and H. X. Tang, "Second harmonic generation in phase matched aluminum nitride waveguides and micro-ring resonators," Appl. Phys. Lett. **100**, 223501 (2012).
86. X. Guo, C.-L. Zou, and H. X. Tang, "Second-harmonic generation in aluminum nitride microrings with 2500%/W conversion efficiency," Optica **3**, 1126–1131 (2016).
87. J. Wang, B. Zhu, Z. Hao, F. Bo, X. Wang, F. Gao, Y. Li, G. Zhang, and J. Xu, "Thermo-optic effects in on-chip lithium niobate microdisk resonators," Opt. Express **24**, 21869–21879 (2016).

88. X. Sun, H. Liang, R. Luo, W. C. Jiang, X.-C. Zhang, and Q. Lin, "Nonlinear optical oscillation dynamics in high-Q lithium niobate microresonators," Opt. Express **25**, 13504–13516 (2017).
89. Y. Dumeige and P. Féron, "Whispering-gallery-mode analysis of phase-matched doubly resonant second-harmonic generation," Phys. Rev. A **74**, 063804 (2006).
90. P. S. Kuo, W. Fang, and G. S. Solomon, "$\bar{4}$-quasi-phase-matched interactions in GaAs microdisk cavities," Opt. Lett. **34**, 3580–3582 (2009).
91. P. Guillemé, M. Vallet, J. Stodolna, A. Ponchet, C. Cornet, A. Létoublon, P. Féron, O. Durand, Y. Léger, and Y. Dumeige, "Antiphase domain tailoring for combination of modal and $\bar{4}$-quasi-phase matching in gallium phosphide microdisks," Opt. Express **24**, 14608–14617 (2016).
92. B. Sturman and I. Breunig, "Generic description of second-order nonlinear phenomena in whispering-gallery resonators," J. Opt. Soc. Am. B **28**, 2465–2471 (2011).
93. P. S. Kuo and G. S. Solomon, "On- and off-resonance second-harmonic generation in GaAs microdisks," Opt. Express **19**, 16898–16918 (2011).
94. G. Lin and N. Yu, "Continuous tuning of double resonance-enhanced second harmonic generation in a dispersive dielectric resonator," Opt. Express **22**, 557–562 (2014).
95. J. U. Fürst, D. V. Strekalov, D. Elser, A. Aiello, U. L. Andersen, C. Marquardt, and G. Leuchs, "Low-threshold optical parametric oscillations in a whispering gallery mode resonator," Phys. Rev. Lett. **105**, 263904 (2010).
96. C. S. Werner, T. Beckmann, K. Buse, and I. Breunig, "Blue-pumped whispering gallery optical parametric oscillator," Opt. Lett. **37**, 4224–4226 (2012).
97. A. A. Savchenkov, A. B. Matsko, M. Mohageg, D. V. Strekalov, and L. Maleki, "Parametric oscillations in a whispering gallery resonator," Opt. Lett. **32**, 157–159 (2007).
98. T. Beckmann, H. Linnenbank, H. Steigerwald, B. Sturman, D. Haertle, K. Buse, and I. Breunig, "Highly tunable low-threshold optical parametric oscillation in radially poled whispering gallery resonators," Phys. Rev. Lett. **106**, 143903 (2011).
99. S.-K. Meisenheimer, J. U. Fürst, C. Werner, T. Beckmann, K. Buse, and I. Breunig, "Broadband infrared spectroscopy using optical parametric oscillation in a radially-poled whispering gallery resonator," Opt. Express **23**, 24042–24047 (2015).
100. G. Schunk, U. Vogl, D. V. Strekalov, M. Förtsch, F. Sedlmeir, H. G. L. Schwefel, M. Göbelt, S. Christiansen, G. Leuchs, and C. Marquardt, "Interfacing transitions of different alkali atoms and telecom bands using one narrowband photon pair source," Optica **2**, 773–778 (2015).
101. C. S. Werner, K. Buse, and I. Breunig, "Continuous-wave whispering-gallery optical parametric oscillator for high-resolution spectroscopy," Opt. Lett. **40**, 772–775 (2015).
102. S.-K. Meisenheimer, J. U. Fürst, A. Schiller, F. Holderied, K. Buse, and I. Breunig, "Pseudo-type-II tuning behavior and mode identification in whispering gallery optical parametric oscillators," Opt. Express **24**, 15137–15142 (2016).
103. Q. Mo, S. Li, Y. Liu, X. Jiang, G. Zhao, Z. Xie, X. Lv, and S. Zhu, "Widely tunable optical parametric oscillator in periodically poled congruently grown lithium tantalite whispering gallery mode resonators," Chin. Opt. Lett. **14**, 91902–91905 (2016).
104. M. Förtsch, J. Fürst, C. Wittmann, D. Strekalov, A. Aiello, M. V. Chekhova, C. Silberhorn, G. Leuchs, and C. Marquardt, "A versatile source of single photons for quantum information processing," Nat. Commun. **4**, 1818 (2013).

105. D. V. Strekalov, A. S. Kowligy, Y.-P. Huang, and P. Kumar, "Optical sum-frequency generation in a whispering-gallery-mode resonator," New J. Phys. **16**, 053025 (2014).
106. T. Carmon and K. J. Vahala, "Visible continuous emission from a silica microphotonic device by third harmonic generation," Nat. Phys. **3**, 430–435 (2007).
107. R. Ismaeel, T. Lee, M. Ding, N. G. Broderick, and G. Brambilla, "Nonlinear microfiber loop resonators for resonantly enhanced third harmonic generation," Opt. Lett. **37**, 5121–5123 (2012).
108. D. Farnesi, A. Barucci, G. Righini, S. Berneschi, S. Soria, and G. N. Conti, "Optical frequency conversion in silica-whispering-gallery-mode microspherical resonators," Phys. Rev. Lett. **112**, 093901 (2014).
109. M. Asano, S. Komori, R. Ikuta, N. Imoto, S. Özdemir, and T. Yamamoto, "Visible light emission from a silica microbottle resonator by second- and third-harmonic generation," Opt. Lett. **41**, 5793–5796 (2016).
110. A. Chen-Jinnai, T. Kato, S. Fujii, T. Nagano, T. Kobatake, and T. Tanabe, "Broad bandwidth third-harmonic generation via four-wave mixing and stimulated Raman scattering in a microcavity," Opt. Express **24**, 26322–26331 (2016).
111. W. Liang, A. A. Savchenkov, Z. Xie, J. F. McMillan, J. Burkhart, V. S. Ilchenko, C. W. Wong, A. B. Matsko, and L. Maleki, "Miniature multioctave light source based on a monolithic microcavity," Optica **2**, 40–47 (2015).
112. L. Wang, L. Chang, N. Volet, M. H. Pfeiffer, M. Zervas, H. Guo, T. J. Kippenberg, and J. E. Bowers, "Frequency comb generation in the green using silicon nitride microresonators," Laser Photon. Rev. **10**, 631–638 (2016).
113. S. Fujii, T. Kato, R. Suzuki, and T. Tanabe, "Third-harmonic blue light generation from Kerr clustered combs and dispersive waves," Opt. Lett. **42**, 2010–2013 (2017).
114. Y. Yang, X. Jiang, S. Kasumie, G. Zhao, L. Xu, J. M. Ward, L. Yang, and S. N. Chormaic, "Four-wave mixing parametric oscillation and frequency comb generation at visible wavelengths in a silica microbubble resonator," Opt. Lett. **41**, 5266–5269 (2016).
115. A. A. Savchenkov, V. S. Ilchenko, F. D. Teodoro, P. M. Belden, W. T. Lotshaw, A. B. Matsko, and L. Maleki, "Generation of Kerr combs centered at 4.5 μm in crystalline microresonators pumped with quantum-cascade lasers," Opt. Lett. **40**, 3468–3471 (2015).
116. A. G. Griffith, R. K. Lau, J. Cardenas, Y. Okawachi, A. Mohanty, R. Fain, Y. H. D. Lee, M. Yu, C. T. Phare, C. B. Poitras, A. L. Gaeta, and M. Lipson, "Silicon-chip mid-infrared frequency comb generation," Nat. Commun. **6**, 6299 (2015).
117. Y. Okawachi, K. Saha, J. S. Levy, Y. H. Wen, M. Lipson, and A. L. Gaeta, "Octave-spanning frequency comb generation in a silicon nitride chip," Opt. Lett. **36**, 3398–3400 (2011).
118. P. Del'Haye, T. Herr, E. Gavartin, M. L. Gorodetsky, R. Holzwarth, and T. J. Kippenberg, "Octave spanning tunable frequency comb from a microresonator," Phys. Rev. Lett. **107**, 063901 (2011).
119. I. H. Agha, Y. Okawachi, and A. L. Gaeta, "Theoretical and experimental investigation of broadband cascaded four-wave mixing in high-Q microspheres," Opt. Express **17**, 16209–16215 (2009).
120. M. Li, X. Wu, L. Liu, and L. Xu, "Kerr parametric oscillations and frequency comb generation from dispersion compensated silica micro-bubble resonators," Opt. Express **21**, 16908–16913 (2013).
121. A. Coillet, I. Balakireva, R. Henriet, K. Saleh, L. Larger, J. Dudley, C. Menyuk, and Y. Chembo, "Azimuthal Turing patterns, bright and dark cavity solitons in Kerr combs generated with whispering-gallery-mode resonators," IEEE Photon. J. **5**, 6100409 (2013).

122. C. Y. Wang, T. Herr, P. Del'Haye, A. Schliesser, J. Hofer, R. Holzwarth, T. W. Hansch, N. Picque, and T. J. Kippenberg, "Mid-infrared optical frequency combs at 2.5 μm based on crystalline microresonators," Nat. Commun. **4**, 1345 (2013).
123. L. Razzari, D. Duchesne, M. Ferrera, R. Morandotti, S. Chu, B. E. Little, and D. J. Moss, "CMOS-compatible integrated optical hyper-parametric oscillator," Nat. Photonics **4**, 41–45 (2010).
124. A. G. Griffith, M. Yu, Y. Okawachi, J. Cardenas, A. Mohanty, A. L. Gaeta, and M. Lipson, "Coherent mid-infrared frequency combs in silicon-microresonators in the presence of Raman effects," Opt. Express **24**, 13044–13050 (2016).
125. B. J. M. Hausmann, I. Bulu, V. Venkataraman, P. Deotare, and M. Loncar, "Diamond nonlinear photonics," Nat. Photonics **8**, 369–374 (2014).
126. M. Pu, L. Ottaviano, E. Semenova, and K. Yvind, "Efficient frequency comb generation in AlGaAs-on-insulator," Optica **3**, 823–826 (2016).
127. H. Jung, C. Xiong, K. Y. Fong, X. Zhang, and H. X. Tang, "Optical frequency comb generation from aluminum nitride microring resonator," Opt. Lett. **38**, 2810–2813 (2013).
128. H. Jung, R. Stoll, X. Guo, D. Fischer, and H. X. Tang, "Green, red, and IR frequency comb line generation from single IR pump in AlN microring resonator," Optica **1**, 396–399 (2014).
129. K. Saha, Y. Okawachi, J. S. Levy, R. K. W. Lau, K. Luke, M. A. Foster, M. Lipson, and A. L. Gaeta, "Broadband parametric frequency comb generation with a 1-μm pump source," Opt. Express **20**, 26935–26941 (2012).
130. Y. Xuan, Y. Liu, L. T. Varghese, A. J. Metcalf, X. Xue, P.-H. Wang, K. Han, J. A. Jaramillo-Villegas, A. A. Noman, C. Wang, S. Kim, M. Teng, Y. J. Lee, B. Niu, L. Fan, J. Wang, D. E. Leaird, A. M. Weiner, and M. Qi, "High-Q silicon nitride microresonators exhibiting low-power frequency comb initiation," Optica **3**, 1171–1180 (2016).
131. Y. K. Chembo, "Kerr optical frequency combs: theory, applications and perspectives," Nanophotonics **5**, 214–230 (2016).
132. A. B. Matsko, A. A. Savchenkov, D. Strekalov, V. S. Ilchenko, and L. Maleki, "Optical hyperparametric oscillations in a whispering-gallery-mode resonator: threshold and phase diffusion," Phys. Rev. A **71**, 033804 (2005).
133. Y. K. Chembo, D. V. Strekalov, and N. Yu, "Spectrum and dynamics of optical frequency combs generated with monolithic whispering gallery mode resonators," Phys. Rev. Lett. **104**, 103902 (2010).
134. Y. K. Chembo and N. Yu, "Modal expansion approach to optical-frequency-comb generation with monolithic whispering-gallery-mode resonators," Phys. Rev. A **82**, 033801 (2010).
135. Y. K. Chembo and N. Yu, "On the generation of octave-spanning optical frequency combs using monolithic whispering-gallery-mode microresonators," Opt. Lett. **35**, 2696–2698 (2010).
136. Y. K. Chembo, "Quantum dynamics of Kerr optical frequency combs below and above threshold: spontaneous four-wave mixing, entanglement, and squeezed states of light," Phys. Rev. A **93**, 033820 (2016).
137. L. Caspani, C. Reimer, M. Kues, P. Roztocki, M. Clerici, B. Wetzel, Y. Jestin, M. Ferrera, M. Peccianti, A. Pasquazi, L. Razzari, B. E. Little, S. T. Chu, D. J. Moss, and R. Morandotti, "Multifrequency sources of quantum correlated photon pairs on-chip: a path toward integrated quantum frequency combs," Nanophotonics **5**, 351–362 (2016).
138. A. A. Savchenkov, A. B. Matsko, M. Mohageg, D. V. Strekalov, and L. Maleki, "Parametric oscillations in a whispering gallery resonator," Opt. Lett. **32**, 157–159 (2006).

139. C. Godey, I. V. Balakireva, A. Coillet, and Y. K. Chembo, "Stability analysis of the spatiotemporal Lugiato-Lefever model for Kerr optical frequency combs in the anomalous and normal dispersion regimes," Phys. Rev. A **89**, 063814 (2014).
140. A. B. Matsko, A. A. Savchenkov, W. Liang, V. S. Ilchenko, D. Seidel, and L. Maleki, "Mode-locked Kerr frequency combs," Opt. Lett. **36**, 2845–2847 (2011).
141. Y. K. Chembo and C. R. Menyuk, "Spatiotemporal Lugiato-Lefever formalism for Kerr-comb generation in whispering-gallery-mode resonators," Phys. Rev. A **87**, 053852 (2013).
142. S. Coen, H. G. Randle, T. Sylvestre, and M. Erkintalo, "Modeling of octave-spanning Kerr frequency combs using a generalized mean-field Lugiato-Lefever model," Opt. Lett. **38**, 37–39 (2013).
143. L. A. Lugiato and R. Lefever, "Spatial dissipative structures in passive optical systems," Phys. Rev. Lett. **58**, 2209–2211 (1987).
144. M. Haelterman, S. Trillo, and S. Wabnitz, "Dissipative modulation instability in a nonlinear dispersive ring cavity," Opt. Commun. **91**, 401–407 (1992).
145. T. Miyaji, I. Ohnishi, and Y. Tsutsumi, "Bifurcation analysis to the Lugiato-Lefever equation in one space dimension," Phys. D **239**, 2066–2083 (2010).
146. G. Kozyreff, "Localized Turing patterns in nonlinear optical cavities," Phys. D **241**, 939–946 (2012).
147. P. Parra-Rivas, D. Gomila, M. A. Matías, S. Coen, and L. Gelens, "Dynamics of localized and patterned structures in the Lugiato-Lefever equation determine the stability and shape of optical frequency combs," Phys. Rev. A **89**, 043813 (2014).
148. A. A. Savchenkov, A. B. Matsko, V. S. Ilchenko, I. Solomatine, D. Seidel, and L. Maleki, "Tunable optical frequency comb with a crystalline whispering gallery mode resonator," Phys. Rev. Lett. **101**, 093902 (2008).
149. G. Lin, K. Saleh, R. Henriet, S. Diallo, R. Martinenghi, A. Coillet, and Y. K. Chembo, "Wide-range tunability, thermal locking, and mode-crossing effects in Kerr optical frequency combs," Opt. Eng. **53**, 122602 (2014).
150. Z. Qi, G. D'Aguanno, and C. R. Menyuk, "Nonlinear frequency combs generated by cnoidal waves in microring resonators," J. Opt. Soc. Am. B **34**, 785–794 (2017).
151. T. Hansson, D. Modotto, and S. Wabnitz, "Dynamics of the modulational instability in microresonator frequency combs," Phys. Rev. A **88**, 023819 (2013).
152. A. Coillet and Y. K. Chembo, "Routes to spatiotemporal chaos in Kerr optical frequency combs," Chaos **24**, 013113 (2014).
153. S. Coen and M. Erkintalo, "Universal scaling laws of Kerr frequency combs," Opt. Lett. **38**, 1790–1792 (2013).
154. T. Herr, V. Brasch, J. D. Jost, C. Y. Wang, N. M. Kondratiev, M. L. Gorodetsky, and T. J. Kippenberg, "Temporal solitons in optical microresonators," Nat. Photonics **8**, 145–152 (2014).
155. X. Yi, Q.-F. Yang, K. Y. Yang, M.-G. Suh, and K. Vahala, "Soliton frequency comb at microwave rates in a high-Q silica microresonator," Optica **2**, 1078–1085 (2015).
156. V. Brasch, M. Geiselmann, T. Herr, G. Lihachev, M. H. P. Pfeiffer, M. L. Gorodetsky, and T. J. Kippenberg, "Photonic chip-based optical frequency comb using soliton Cherenkov radiation," Science **351**, 357–360 (2016).
157. Y. H. Wen, M. R. E. Lamont, S. H. Strogatz, and A. L. Gaeta, "Self-organization in Kerr-cavity-soliton formation in parametric frequency combs," Phys. Rev. A **94**, 063843 (2016).
158. M. R. E. Lamont, Y. Okawachi, and A. L. Gaeta, "Route to stabilized ultrabroadband microresonator-based frequency combs," Opt. Lett. **38**, 3478–3481 (2013).

159. M. Karpov, H. Guo, A. Kordts, V. Brasch, M. H. P. Pfeiffer, M. Zervas, M. Geiselmann, and T. J. Kippenberg, "Raman self-frequency shift of dissipative Kerr solitons in an optical microresonator," Phys. Rev. Lett. **116**, 103902 (2016).
160. Q. Li, T. C. Briles, D. A. Westly, T. E. Drake, J. R. Stone, B. R. Ilic, S. A. Diddams, S. B. Papp, and K. Srinivasan, "Stably accessing octave-spanning microresonator frequency combs in the soliton regime," Optica **4**, 193–203 (2017).
161. X. Yi, Q.-F. Yang, K. Y. Yang, and K. Vahala, "Active capture and stabilization of temporal solitons in microresonators," Opt. Lett. **41**, 2037–2040 (2016).
162. X. Hu, Y. Liu, X. Xu, Y. Feng, W. Zhang, W. Wang, J. Song, Y. Wang, and W. Zhao, "Spatiotemporal evolution of a cosine-modulated stationary field and Kerr frequency comb generation in a microresonator," Appl. Opt. **54**, 8751–8757 (2015).
163. H. Guo, M. Karpov, E. Lucas, A. Kordts, M. H. P. Pfeiffer, V. Brasch, G. Lihachev, V. E. Lobanov, M. L. Gorodetsky, and T. J. Kippenberg, "Universal dynamics and deterministic switching of dissipative Kerr solitons in optical microresonators," Nat. Phys. **13**, 94–102 (2017).
164. P. Del'Haye, K. Beha, S. B. Papp, and S. A. Diddams, "Self-injection locking and phase-locked states in microresonator-based optical frequency combs," Phys. Rev. Lett. **112**, 043905 (2014).
165. P. Del'Haye, A. Coillet, W. Loh, K. Beha, S. B. Papp, and S. A. Diddams, "Phase steps and resonator detuning measurements in microresonator frequency combs," Nat. Commun. **6**, 5668 (2015).
166. J. M. Silver, C. Guo, L. Del Bino, and P. Del'Haye, "Kerr superoscillator model for microresonator frequency combs," Phys. Rev. A **95**, 033835 (2017).
167. P. Parra-Rivas, D. Gomila, F. Leo, S. Coen, and L. Gelens, "Third-order chromatic dispersion stabilizes Kerr frequency combs," Opt. Lett. **39**, 2971–2974 (2014).
168. S. Wang, H. Guo, X. Bai, and X. Zeng, "Broadband Kerr frequency combs and intracavity soliton dynamics influenced by high-order cavity dispersion," Opt. Lett. **39**, 2880–2883 (2014).
169. T. Herr, V. Brasch, J. D. Jost, I. Mirgorodskiy, G. Lihachev, M. L. Gorodetsky, and T. J. Kippenberg, "Mode spectrum and temporal soliton formation in optical microresonators," Phys. Rev. Lett. **113**, 123901 (2014).
170. H. Taheri, A. A. Eftekhar, K. Wiesenfeld, and A. Adibi, "Soliton formation in whispering-gallery-mode resonators via input phase modulation," IEEE Photon. J. **7**, 2200309 (2015).
171. H. Taheri, P. Del'Haye, A. A. Eftekhar, K. Wiesenfeld, and A. Adibi, "Self-synchronization phenomena in the Lugiato-Lefever equation," Phys. Rev. A **96**, 013828 (2017).
172. M. Liao, H. Zhou, Y. Geng, Y. Ling, B. Wu, and K. Qiu, "Enhanced single cavity soliton generation in Kerr microresonators via inverse-Kelly sideband," IEEE Photon. J. **9**, 4501709 (2017).
173. W. Wang, W. Zhang, S. T. Chu, B. E. Little, Q. Yang, L. Wang, X. Hu, L. Wang, G. Wang, Y. Wang, and W. Zhao, "Repetition rate multiplication pulsed laser source based on a microring resonator," ACS Photon. **4**, 1677–1683 (2017).
174. J. H. T. Mbe, C. Millián, and Y. K. Chembo, "Existence and switching behavior of bright and dark Kerr solitons in whispering-gallery mode resonators with zero group-velocity dispersion," Eur. Phys. J. D **71**, 196 (2017).
175. J. K. Jang, Y. Okawachi, M. Yu, K. Luke, X. Ji, M. Lipson, and A. L. Gaeta, "Dynamics of mode-coupling-induced microresonator frequency combs in normal dispersion," Opt. Express **24**, 28794–28803 (2016).

176. P. Parra-Rivas, D. Gomila, E. Knobloch, S. Coen, and L. Gelens, "Origin and stability of dark pulse Kerr combs in normal dispersion resonators," Opt. Lett. **41**, 2402–2405 (2016).
177. W. Liang, D. Eliyahu, A. B. Matsko, V. S. Ilchenko, D. Seidel, and L. Maleki, "Spectrally pure RF photonic source based on a resonant optical hyper-parametric oscillator," Proc. SPIE **8960**, 896010 (2014).
178. W. Liang, A. A. Savchenkov, V. S. Ilchenko, D. Eliyahu, D. Seidel, A. B. Matsko, and L. Maleki, "Generation of a coherent near-infrared Kerr frequency comb in a monolithic microresonator with normal GVD," Opt. Lett. **39**, 2920–2923 (2014).
179. Y. Liu, Y. Xuan, X. Xue, P.-H. Wang, S. Chen, A. J. Metcalf, J. Wang, D. E. Leaird, M. Qi, and A. M. Weiner, "Investigation of mode coupling in normal-dispersion silicon nitride microresonators for Kerr frequency comb generation," Optica **1**, 137–144 (2014).
180. X. Xue, Y. Xuan, Y. Liu, P.-H. Wang, S. Chen, J. Wang, D. E. Leaird, M. Qi, and A. M. Weiner, "Mode-locked dark pulse Kerr combs in normal-dispersion micro-resonators," Nat. Photonics **9**, 594–600 (2015).
181. S.-W. Huang, H. Zhou, J. Yang, J. F. McMillan, A. Matsko, M. Yu, D.-L. Kwong, L. Maleki, and C. W. Wong, "Mode-locked ultrashort pulse generation from on-chip normal dispersion microresonators," Phys. Rev. Lett. **114**, 053901 (2015).
182. X. Xue, Y. Xuan, P.-H. Wang, Y. Liu, D. E. Leaird, M. Qi, and A. M. Weiner, "Normal-dispersion microcombs enabled by controllable mode interactions," Laser Photon. Rev. **9**, L23–L28 (2015).
183. M. Li, M. Zhang, J. Wang, W. Chang, F. Zhou, and L. Deng, "Flexible tuning optical frequency combs via parametric seeding in microresonators with normal dispersion," IEEE Photon. J. **7**, 1400907 (2015).
184. V. E. Lobanov, G. Lihachev, and M. L. Gorodetsky, "Generation of platicons and frequency combs in optical microresonators with normal GVD by modulated pump," Europhys. Lett. **112**, 54008 (2015).
185. A. B. Matsko, A. A. Savchenkov, and L. Maleki, "On excitation of breather solitons in an optical microresonator," Opt. Lett. **37**, 4856–4858 (2012).
186. C. Bao and C. Yang, "Carrier-envelope phase dynamics of cavity solitons: scaling law and soliton stability," Phys. Rev. A **92**, 053831 (2015).
187. G. R. Kol, J. Kamdem, and T. C. Kofané, "Routes to various breather solitons in whispering-gallery-mode resonators through the variational method," J. Mod. Opt. **63**, 2259–2264 (2016).
188. C. Bao, J. A. Jaramillo-Villegas, Y. Xuan, D. E. Leaird, M. Qi, and A. M. Weiner, "Observation of Fermi-Pasta-Ulam recurrence induced by breather solitons in an optical microresonator," Phys. Rev. Lett. **117**, 163901 (2016).
189. Z. Liu, M. Ouali, S. Coulibaly, M. G. Clerc, M. Taki, and M. Tlidi, "Characterization of spatiotemporal chaos in a Kerr optical frequency comb and in all fiber cavities," Opt. Lett. **42**, 1063–1066 (2017).
190. A. Coillet, J. Dudley, G. Genty, L. Larger, and Y. K. Chembo, "Optical rogue waves in whispering-gallery-mode resonators," Phys. Rev. A **89**, 013835 (2014).
191. L. Zhang, C. Bao, V. Singh, J. Mu, C. Yang, A. M. Agarwal, L. C. Kimerling, and J. Michel, "Generation of two-cycle pulses and octave-spanning frequency combs in a dispersion-flattened micro-resonator," Opt. Lett. **38**, 5122–5125 (2013).
192. I. S. Grudinin, L. Baumgartel, and N. Yu, "Impact of cavity spectrum on span in microresonator frequency combs," Opt. Express **21**, 26929–26935 (2013).

193. Y. Okawachi, M. R. E. Lamont, K. Luke, D. O. Carvalho, M. Yu, M. Lipson, and A. L. Gaeta, "Bandwidth shaping of microresonator-based frequency combs via dispersion engineering," Opt. Lett. **39**, 3535–3538 (2014).
194. I. S. Grudinin and N. Yu, "Dispersion engineering of crystalline resonators via microstructuring," Optica **2**, 221–224 (2015).
195. G. Lin and Y. K. Chembo, "On the dispersion management of fluorite whispering-gallery mode resonators for Kerr optical frequency comb generation in the telecom and mid-infrared range," Opt. Express **23**, 1594–1604 (2015).
196. Y. Nakagawa, Y. Mizumoto, T. Kato, T. Kobatake, H. Itobe, Y. Kakinuma, and T. Tanabe, "Dispersion tailoring of a crystalline whispering gallery mode microcavity for a wide-spanning optical Kerr frequency comb," J. Opt. Soc. Am. B **33**, 1913–1920 (2016).
197. M. Soltani, A. Matsko, and L. Maleki, "Enabling arbitrary wavelength frequency combs on chip," Laser Photon. Rev. **10**, 158–162 (2016).
198. S.-W. Huang, J. Yang, J. Lim, H. Zhou, M. Yu, D.-L. Kwong, and C. W. Wong, "A low-phase-noise 18 GHz Kerr frequency microcomb phase-locked over 65 THz," Sci. Rep. **5**, 13355 (2015).
199. G. Lin, Y. Candela, O. Tillement, Z. Cai, V. Leffèvre-Seguin, and J. Hare, "Thermal bistability-based method for real-time optimization of ultralow-threshold whispering gallery mode microlasers," Opt. Lett. **37**, 5193–5195 (2012).
200. S. Diallo, G. Lin, and Y. K. Chembo, "Giant thermo-optical relaxation oscillations in millimeter-size whispering gallery mode disk resonators," Opt. Lett. **40**, 3834–3837 (2015).
201. A. Coillet, P. Del'Haye, W. Loh, K. Beha, S. B. Papp, and S. A. Diddams, "Measuring optical phases of Kerr frequency combs," in *Frontiers in Optics* (Optical Society of America, 2014), paper FM4B.4.
202. W. Liang, D. Eliyahu, V. S. Ilchenko, A. A. Savchenkov, A. B. Matsko, D. Seidel, and L. Maleki, "High spectral purity Kerr frequency comb radio frequency photonic oscillator," Nat. Commun. **6**, 7957 (2015).
203. K. E. Webb, J. K. Jang, J. Anthony, S. Coen, M. Erkintalo, and S. G. Murdoch, "Measurement of microresonator frequency comb coherence by spectral interferometry," Opt. Lett. **41**, 277–280 (2016).
204. P.-H. Wang, F. Ferdous, H. Miao, J. Wang, D. E. Leaird, K. Srinivasan, L. Chen, V. Aksyuk, and A. M. Weiner, "Observation of correlation between route to formation, coherence, noise, and communication performance of Kerr combs," Opt. Express **20**, 29284–29295 (2012).
205. A. Coillet and Y. Chembo, "On the robustness of phase locking in Kerr optical frequency combs," Opt. Lett. **39**, 1529–1532 (2014).
206. V. Torres-Company, D. Castelló-Lurbe, and E. Silvestre, "Comparative analysis of spectral coherence in microresonator frequency combs," Opt. Express **22**, 4678–4691 (2014).
207. J. Pfeifle, A. Coillet, R. Henriet, K. Saleh, P. Schindler, C. Weimann, W. Freude, I. V. Balakireva, L. Larger, C. Koos, and Y. K. Chembo, "Optimally coherent Kerr combs generated with crystalline whispering gallery mode resonators for ultrahigh capacity fiber communications," Phys. Rev. Lett. **114**, 093902 (2015).
208. M. Peccianti, A. Pasquazi, Y. Park, B. Little, S. T. Chu, D. Moss, and R. Morandotti, "Demonstration of a stable ultrafast laser based on a nonlinear microcavity," Nat. Commun. **3**, 765 (2012).
209. S. B. Papp, P. Del'Haye, and S. A. Diddams, "Parametric seeding of a microresonator optical frequency comb," Opt. Express **21**, 17615–17624 (2013).
210. G. Lin, R. Martinenghi, S. Diallo, K. Saleh, A. Coillet, and Y. K. Chembo, "Spectro-temporal dynamics of Kerr combs with parametric seeding," Appl. Opt. **54**, 2407–2412 (2015).

211. T. J. Kippenberg, R. Holzwarth, and S. A. Diddams, "Microresonator-based optical frequency combs," Science **332**, 555–559 (2011).
212. S. Diallo and Y. K. Chembo, "Optimization of primary Kerr optical frequency combs for tunable microwave generation," Opt. Lett. **42**, 3522–3525 (2017).
213. K. Saleh and Y. K. Chembo, "On the phase noise performance of microwave and millimeter-wave signals generated with versatile Kerr optical frequency combs," Opt. Express **24**, 25043–25056 (2016).
214. K. Saleh and Y. Chembo, "Phase noise performance comparison between microwaves generated with Kerr optical frequency combs and optoelectronic oscillators," Electron. Lett. **53**, 264–266 (2017).
215. K. Saleh and Y. K. Chembo, "Optimization of close-in phase noise for microwaves generated with Kerr combs using Brillouin-assisted pump depletion," IEEE Photon. J. **8**, 5501807 (2016).
216. P. Del'Haye, O. Arcizet, A. Schliesser, R. Holzwarth, and T. J. Kippenberg, "Full stabilization of a microresonator-based optical frequency comb," Phys. Rev. Lett. **101**, 053903 (2008).
217. S. B. Papp, K. Beha, P. Del'Haye, F. Quinlan, H. Lee, K. J. Vahala, and S. A. Diddams, "Microresonator frequency comb optical clock," Optica **1**, 10–14 (2014).
218. P. Del'Haye, S. B. Papp, and S. A. Diddams, "Hybrid electro-optically modulated microcombs," Phys. Rev. Lett. **109**, 263901 (2012).
219. J. D. Jost, T. Herr, C. Lecaplain, V. Brasch, M. H. P. Pfeiffer, and T. J. Kippenberg, "Counting the cycles of light using a self-referenced optical microresonator," Optica **2**, 706–711 (2015).
220. P. Del'Haye, A. Coillet, T. Fortier, K. Beha, D. C. Cole, K. Y. Yang, H. Lee, K. J. Vahala, S. B. Papp, and S. A. Diddams, "Phase-coherent microwave-to-optical link with a self-referenced microcomb," Nat. Photonics **10**, 516–520 (2016).
221. A. Coillet, R. Henriet, P. Salzenstein, K. P. Huy, L. Larger, and Y. K. Chembo, "Time-domain dynamics and stability analysis of optoelectronic oscillators based on whispering-gallery mode resonators," IEEE J. Sel. Top. Quantum Electron. **19**, 1–12 (2013).
222. K. Saleh, R. Henriet, S. Diallo, G. Lin, R. Martinenghi, I. V. Balakireva, P. Salzenstein, A. Coillet, and Y. K. Chembo, "Phase noise performance comparison between optoelectronic oscillators based on optical delay lines and whispering gallery mode resonators," Opt. Express **22**, 32158–32173 (2014).
223. K. Saleh, G. Lin, and Y. K. Chembo, "Effect of laser coupling and active stabilization on the phase noise performance of optoelectronic microwave oscillators based on whispering-gallery-mode resonators," IEEE Photon. J. **7**, 5500111 (2015).
224. R. M. Nguimdo, K. Saleh, A. Coillet, G. Lin, R. Martinenghi, and Y. K. Chembo, "Phase noise performance of optoelectronic oscillators based on whispering-gallery mode resonators," IEEE J. Quantum Electron. **51**, 6500308 (2015).
225. R. M. Nguimdo, V. Lecocq, Y. K. Chembo, and T. Erneux, "Effect of time delay on the stability of optoelectronic oscillators based on whispering-gallery mode resonators," IEEE J. Quantum Electron. **52**, 6500107 (2016).
226. Y. K. Chembo, L. Baumgartel, and N. Yu, "Neutral mounting of ultrahigh Q whispering gallery mode disc-resonators for metrological applications," IEEE Photon. J. **9**, 6800308 (2017).
227. J. S. Levy, K. Saha, Y. Okawachi, M. A. Foster, A. L. Gaeta, and M. Lipson, "High-performance silicon-nitride-based multiple-wavelength source," IEEE Photon. Technol. Lett. **24**, 1375–1377 (2012).
228. J. Pfeifle, V. Brasch, M. Lauermann, Y. Yu, D. Wegner, T. Herr, K. Hartinger, P. Schindler, J. Li, D. Hillerkuss, R. Schmogrow, C. Weimann, R. Holzwarth,

W. Freude, J. Leuthold, T. J. Kippenberg, and C. Koos, "Coherent terabit communications with microresonator Kerr frequency combs," Nat. Photonics **8**, 375–380 (2014).
229. Y.-C. Chuang, T.-A. Liu, W.-J. Ting, H.-F. Chen, Y.-C. Cheng, P.-E. Hsu, and J.-L. Peng, "Compact and portable 100-GHz microresonator-based optical frequency comb generation system for dense wavelength division multiplexing fiber optic communication," Opt. Eng. **55**, 100503 (2016).
230. P. Marin-Palomo, J. N. Kemal, M. Karpov, A. Kordts, J. Pfeifle, M. H. P. Pfeiffer, P. Trocha, S. Wolf, V. Brasch, M. H. Anderson, R. Rosenberger, K. Vijayan, W. Freude, T. J. Kippenberg, and C. Koos, "Microresonator-based solitons for massively parallel coherent optical communications," Nature **546**, 274–279 (2017).
231. S. Hua, J. Wen, X. Jiang, Q. Hua, L. Jiang, and M. Xiao, "Demonstration of a chip-based optical isolator with parametric amplification," Nat. Commun. **7**, 13657 (2016).
232. J. B. Snow, S.-X. Qian, and R. K. Chang, "Stimulated Raman scattering from individual water and ethanol droplets at morphology-dependent resonances," Opt. Lett. **10**, 37–39 (1985).
233. S. M. Spillane, T. J. Kippenberg, and K. J. Vahala, "Ultralow-threshold Raman laser using a spherical dielectric microcavity," Nature **415**, 621–623 (2002).
234. T. J. Kippenberg, S. M. Spillane, B. Min, and K. J. Vahala, "Theoretical and experimental study of stimulated and cascaded Raman scattering in ultrahigh-Q optical microcavities," IEEE J. Sel. Top. Quantum Electron. **10**, 1219–1228 (2004).
235. L. Sirleto, A. Vergara, and M. A. Ferrara, "Advances in stimulated Raman scattering in nanostructures," Adv. Opt. Photon. **9**, 169–217 (2017).
236. X. Liu, C. Sun, B. Xiong, L. Wang, J. Wang, Y. Han, Z. Hao, H. Li, Y. Luo, J. Yan, T. Wei, Y. Zhang, and J. Wang, "Integrated continuous-wave aluminum nitride Raman laser," Optica **4**, 893–896 (2017).
237. Y. K. Chembo, I. S. Grudinin, and N. Yu, "Spatiotemporal dynamics of Kerr-Raman optical frequency combs," Phys. Rev. A **92**, 043818 (2015).
238. G. Lin, S. Diallo, J. M. Dudley, and Y. K. Chembo, "Universal nonlinear scattering in ultra-high Q whispering gallery-mode resonators," Opt. Express **24**, 14880–14894 (2016).
239. B. Min, T. J. Kippenberg, and K. J. Vahala, "Compact, fiber-compatible, cascaded Raman laser," Opt. Lett. **28**, 1507–1509 (2003).
240. A. Mazzei, H. Krauter, O. Benson, and S. Götzinger, "Influence of a controllable scatterer on the lasing properties of an ultralow threshold Raman microlaser," Appl. Phys. Lett. **89**, 101105 (2006).
241. T. Lu, L. Yang, T. Carmon, and B. Min, "A narrow-linewidth on-chip toroid Raman laser," IEEE J. Quantum Electron. **47**, 320–326 (2011).
242. M. V. Chistiakova and A. M. Armani, "Cascaded Raman microlaser in air and buffer," Opt. Lett. **37**, 4068–4070 (2012).
243. X.-F. Jiang, Y.-F. Xiao, Q.-F. Yang, L. Shao, W. R. Clements, and Q. Gong, "Free-space coupled, ultralow-threshold Raman lasing from a silica microcavity," Appl. Phys. Lett. **103**, 101102 (2013).
244. F. Vanier, M. Rochette, N. Godbout, and Y.-A. Peter, "Raman lasing in As_2S_3 high-Q whispering gallery mode resonators," Opt. Lett. **38**, 4966–4969 (2013).
245. N. Deka, A. J. Maker, and A. M. Armani, "Titanium-enhanced Raman microcavity laser," Opt. Lett. **39**, 1354–1357 (2014).
246. D. Farnesi, F. Cosi, C. Trono, G. C. Righini, G. N. Conti, and S. Soria, "Stimulated anti-Stokes Raman scattering resonantly enhanced in silica microspheres," Opt. Lett. **39**, 5993–5996 (2014).

247. B.-B. Li, W. R. Clements, X.-C. Yu, K. Shi, Q. Gong, and Y.-F. Xiao, "Single nanoparticle detection using split-mode microcavity Raman lasers," Proc. Natl. Acad. Sci. U. S. A. **111**, 14657–14662 (2014).
248. Ş. K. Özdemir, J. Zhu, X. Yang, B. Peng, H. Yilmaz, L. He, F. Monifi, S. H. Huang, G. L. Long, and L. Yang, "Highly sensitive detection of nanoparticles with a self-referenced and self-heterodyned whispering-gallery Raman microlaser," Proc. Natl. Acad. Sci. U. S. A. **111**, E3836–E3844 (2014).
249. B. Peng, S. K. Özdemir, S. Rotter, H. Yilmaz, M. Liertzer, F. Monifi, C. M. Bender, F. Nori, and L. Yang, "Loss-induced suppression and revival of lasing," Science **346**, 328–332 (2014).
250. F. Vanier, Y.-A. Peter, and M. Rochette, "Cascaded Raman lasing in packaged high quality As_2S-3 microspheres," Opt. Express **22**, 28731–28739 (2014).
251. W. R. Clements, B.-B. Li, B.-Q. Shen, and Y.-F. Xiao, "Raman-lasing dynamics in split-mode microresonators," Phys. Rev. A **91**, 013804 (2015).
252. D. Farnesi, A. Barucci, G. C. Righini, G. N. Conti, and S. Soria, "Generation of hyper-parametric oscillations in silica microbubbles," Opt. Lett. **40**, 4508–4511 (2015).
253. Y. Ooka, Y. Yang, J. Ward, and S. N. Chormaic, "Raman lasing in a hollow, bottle-like microresonator," Appl. Phys. Express **8**, 092001 (2015).
254. X. Yang, S. K. Özdemir, B. Peng, H. Yilmaz, F.-C. Lei, G.-L. Long, and L. Yang, "Raman gain induced mode evolution and on-demand coupling control in whispering-gallery-mode microcavities," Opt. Express **23**, 29573–29583 (2015).
255. T. Kato, A. Hori, R. Suzuki, S. Fujii, T. Kobatake, and T. Tanabe, "Transverse mode interaction via stimulated Raman scattering comb in a silica microcavity," Opt. Express **25**, 857–866 (2017).
256. B.-B. Li, Y.-F. Xiao, M.-Y. Yan, W. R. Clements, and Q. Gong, "Low-threshold Raman laser from an on-chip, high-Q, polymer-coated microcavity," Opt. Lett. **38**, 1802–1804 (2013).
257. I. S. Grudinin and L. Maleki, "Ultralow-threshold Raman lasing with CaF_2 resonators," Opt. Lett. **32**, 166–168 (2007).
258. W. Liang, V. S. Ilchenko, A. A. Savchenkov, A. B. Matsko, D. Seidel, and L. Maleki, "Passively mode-locked Raman laser," Phys. Rev. Lett. **105**, 143903 (2010).
259. G. Lin and Y. K. Chembo, "Phase-locking transition in Raman combs generated with whispering gallery mode resonators," Opt. Lett. **41**, 3718–3721 (2016).
260. J. Moore, M. Tomes, T. Carmon, and M. Jarrahi, "Continuous-wave cascaded-harmonic generation and multi-photon Raman lasing in lithium niobate whispering-gallery resonators," Appl. Phys. Lett. **99**, 221111 (2011).
261. M. T. Simons and I. Novikova, "Observation of second-order hyper-Raman generation in $LiNbO_3$ whispering-gallery mode disk resonators," Opt. Lett. **36**, 3027–3029 (2011).
262. M. Leidinger, B. Sturman, K. Buse, and I. Breunig, "Strong forward-backward asymmetry of stimulated Raman scattering in lithium-niobate-based whispering gallery resonators," Opt. Lett. **41**, 2823–2826 (2016).
263. R. Drever, J. L. Hall, F. Kowalski, J. Hough, G. Ford, A. Munley, and H. Ward, "Laser phase and frequency stabilization using an optical resonator," Appl. Phys. B **31**, 97–105 (1983).
264. Q.-F. Yang, X. Yi, K. Y. Yang, and K. Vahala, "Stokes solitons in optical microcavities," Nat. Phys. **13**, 53–57 (2016).
265. A. Kobyakov, M. Sauer, and D. Chowdhury, "Stimulated Brillouin scattering in optical fibers," Adv. Opt. Photon. **2**, 1–59 (2010).

266. B. J. Eggleton, C. G. Poulton, and R. Pant, "Inducing and harnessing stimulated Brillouin scattering in photonic integrated circuits," Adv. Opt. Photon. **5**, 536–587 (2013).
267. P. T. Rakich, C. Reinke, R. Camacho, P. Davids, and Z. Wang, "Giant enhancement of stimulated Brillouin scattering in the subwavelength limit," Phys. Rev. X **2**, 011008 (2012).
268. I. S. Grudinin, A. B. Matsko, and L. Maleki, "Brillouin lasing with a CaF_2 whispering gallery mode resonator," Phys. Rev. Lett. **102**, 043902 (2009).
269. M. Tomes and T. Carmon, "Photonic micro-electromechanical systems vibrating at X-band (11-GHz) rates," Phys. Rev. Lett. **102**, 113601 (2009).
270. G. Bahl, J. Zehnpfennig, M. Tomes, and T. Carmon, "Stimulated optomechanical excitation of surface acoustic waves in a microdevice," Nat. Commun. **2**, 403 (2011).
271. C. Guo, K. Che, P. Zhang, J. Wu, Y. Huang, H. Xu, and Z. Cai, "Low-threshold stimulated Brillouin scattering in high-Q whispering gallery mode tellurite microspheres," Opt. Express **23**, 32261–32266 (2015).
272. J. Li, H. Lee, and K. J. Vahala, "Microwave synthesizer using an on-chip Brillouin oscillator," Nat. Commun. **4**, 2097 (2013).
273. W. Loh, A. A. S. Green, F. N. Baynes, D. C. Cole, F. J. Quinlan, H. Lee, K. J. Vahala, S. B. Papp, and S. A. Diddams, "Dual-microcavity narrow-linewidth Brillouin laser," Optica **2**, 225–232 (2015).
274. W. Loh, M. T. Hummon, H. F. Leopardi, T. M. Fortier, F. Quinlan, J. Kitching, S. B. Papp, and S. A. Diddams, "Microresonator Brillouin laser stabilization using a microfabricated rubidium cell," Opt. Express **24**, 14513–14524 (2016).
275. W. Loh, J. Becker, D. C. Cole, A. Coillet, F. N. Baynes, S. B. Papp, and S. A. Diddams, "A microrod-resonator Brillouin laser with 240 Hz absolute linewidth," New J. Phys. **18**, 045001 (2016).
276. M. Asano, Y. Takeuchi, S. K. Ozdemir, R. Ikuta, L. Yang, N. Imoto, and T. Yamamoto, "Stimulated Brillouin scattering and Brillouin-coupled four-wave-mixing in a silica microbottle resonator," Opt. Express **24**, 12082–12092 (2016).
277. G. Bahl, K. H. Kim, W. Lee, J. Liu, X. Fan, and T. Carmon, "Brillouin cavity optomechanics with microfluidic devices," Nat. Commun. **4**, 1994 (2013).
278. G. Lin, S. Diallo, K. Saleh, R. Martinenghi, J.-C. Beugnot, T. Sylvestre, and Y. K. Chembo, "Cascaded Brillouin lasing in monolithic barium fluoride whispering gallery mode resonators," Appl. Phys. Lett. **105**, 231103 (2014).
279. J. Zehnpfennig, G. Bahl, M. Tomes, and T. Carmon, "Surface optomechanics: calculating optically excited acoustical whispering gallery modes in microspheres," Opt. Express **19**, 14240–14248 (2011).
280. M. Dong and H. G. Winful, "Unified approach to cascaded stimulated Brillouin scattering and frequency-comb generation," Phys. Rev. A **93**, 043851 (2016).
281. J. A. Haigh, A. Nunnenkamp, A. J. Ramsay, and A. J. Ferguson, "Triple-resonant Brillouin light scattering in magneto-optical cavities," Phys. Rev. Lett. **117**, 133602 (2016).
282. A. Osada, R. Hisatomi, A. Noguchi, Y. Tabuchi, R. Yamazaki, K. Usami, M. Sadgrove, R. Yalla, M. Nomura, and Y. Nakamura, "Cavity optomagnonics with spin-orbit coupled photons," Phys. Rev. Lett. **116**, 223601 (2016).
283. X. Zhang, N. Zhu, C.-L. Zou, and H. X. Tang, "Optomagnonic whispering gallery microresonators," Phys. Rev. Lett. **117**, 123605 (2016).
284. R. Zhang, J. Sun, G. Chen, M. Cheng, and J. Jiang, "Demonstration of highly efficient forward stimulated Brillouin scattering in partly suspended silicon nanowire racetrack resonators," Appl. Phys. Lett. **111**, 031102 (2017).
285. G. Lin and Y. K. Chembo, "Opto-acoustic phenomena in whispering gallery mode resonators," Int. J. Optomechatron. **10**, 32–39 (2016).

286. G. Lin, B. Qian, F. Oručević, Y. Candela, J.-B. Jager, Z. Cai, V. Lefèvre-Seguin, and J. Hare, "Excitation mapping of whispering gallery modes in silica microcavities," Opt. Lett. **35**, 583–585 (2010).
287. B. Yao, C. Yu, Y. Wu, S.-W. Huang, H. Wu, Y. Gong, Y. Chen, Y. Li, C. W. Wong, X. Fan, and Y. Rao, "Graphene-enhanced Brillouin optomechanical microresonator for ultrasensitive gas detection," Nano Lett. **17**, 4996–5002 (2017).
288. G. Bahl, M. Tomes, F. Marquardt, and T. Carmon, "Observation of spontaneous Brillouin cooling," Nat. Phys. **8**, 203–207 (2012).
289. C.-H. Dong, Z. Shen, C.-L. Zou, Y.-L. Zhang, W. Fu, and G.-C. Guo, "Brillouin-scattering-induced transparency and non-reciprocal light storage," Nat. Commun. **6**, 6193 (2015).
290. J. Kim, M. C. Kuzyk, K. Han, H. Wang, and G. Bahl, "Non-reciprocal Brillouin scattering induced transparency," Nat. Phys. **11**, 275–280 (2015).
291. Y.-S. Park and H. Wang, "Resolved-sideband and cryogenic cooling of an optomechanical resonator," Nat. Phys. **5**, 489–493 (2009).
292. J. Li, H. Lee, and K. J. Vahala, "Low-noise Brillouin laser on a chip at 1064 nm," Opt. Lett. **39**, 287–290 (2014).
293. J. Li, M.-G. Suh, and K. Vahala, "Microresonator Brillouin gyroscope," Optica **4**, 346–348 (2017).
294. W. Liang, V. S. Ilchenko, A. A. Savchenkov, E. Dale, D. Eliyahu, A. B. Matsko, and L. Maleki, "Resonant microphotonic gyroscope," Optica **4**, 114–117 (2017).
295. S. Weis, R. Rivière, S. Deléglise, E. Gavartin, O. Arcizet, A. Schliesser, and T. J. Kippenberg, "Optomechanically induced transparency," Science **330**, 1520–1523 (2010).
296. V. Fiore, Y. Yang, M. C. Kuzyk, R. Barbour, L. Tian, and H. Wang, "Storing optical information as a mechanical excitation in a silica optomechanical resonator," Phys. Rev. Lett. **107**, 133601 (2011).

Guoping Lin received his joint PhD degrees in optics and physics from Xiamen University, China and *École Normale Supérieure* of Paris, France, in 2010. He subsequently worked as a NASA postdoctoral fellow at the Jet Propulsion Laboratory in Pasadena, California, USA and then as a postdoc at FEMTO-ST Institute in Besançon, France. He is now an associate professor at MOE Key Laboratory of Fundamental Quantities Measurement, School of Physics, Huazhong University of Science and Technology in Wuhan, China. Dr. Lin's research interests focus on device physics, nonlinear optics, and laser physics using ultrahigh-Q optical resonators.

Aurélien Coillet graduated from the *École Normale Supérieure* of Lyon, France, and received his PhD in nonlinear optics from the Burgundy University, France. He continued his research as a postdoctoral fellow at the FEMTO-ST Institute, France, and then at NIST Boulder, Colorado, USA, where he focused on the nonlinear dynamics of Kerr comb generation. He now holds a position of associate professor at the University Bourgogne-Franche-Comté and at the *Laboratoire Interdisciplinaire Carnot de Bourgogne*, France. His research activities include the study of nonlinear optical phenomena in micro- and nano-devices, and the development of new fiber lasers.

Yanne K. Chembo received in 2006 a PhD degree in photonics from the University of the Balearic Islands (Palma de Mallorca, Spain), and independently, a PhD degree in nonlinear dynamics from the University of Yaoundé I (Cameroon). In 2007 and 2008, he was a postdoctoral fellow with the FEMTO-ST Institute in Besançon, France. In 2009, he was a NASA Postdoctoral Program (NPP) Fellow at the Quantum Science and Technology Group of the Jet Propulsion Laboratory, Caltech (Pasadena, California, USA). From 2010 to 2016, he was a senior research scientist with CNRS (*Centre National de la Recherche Scientifique*) in France, with affiliation to the FEMTO-ST Institute where he founded and led the Microwave Photonics Group for Aerospace and Communication Engineering. In 2017, he joined the International GeorgiaTech-CNRS Research Laboratory in Atlanta, Georgia, USA. He has co-authored more than 150 articles in refereed international journals and international conference proceedings. His research interests involve microwave photonics, optoelectronics, as well as the nonlinear, stochastic, and quantum dynamics of complex photonic systems. He is a senior member of IEEE and OSA, and an associate editor for the OSA journal *Optics Express*.